

DTIC FILE COPY

4

AD-A222 660

GL-TR-90-0057

**Formation and Deactivation of Vibrationally
Excited Atmospheric Molecules**

J. Steinfeld
C. Fell
M. Phillips
J. Klaassen
C. Van Zoeren

Massachusetts Institute of Technology
Department of Chemistry
Cambridge, MA 02139

20 March 1990



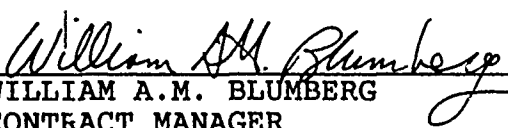
Final Report
1 July 1986-31 March 1990

APPROVED FOR PUBLIC RELEASE; DISTRIBUTION UNLIMITED

GEOPHYSICS LABORATORY
AIR FORCE SYSTEMS COMMAND
UNITED STATES AIR FORCE
HANSCOM AIR FORCE BASE, MASSACHUSETTS 01731-5000

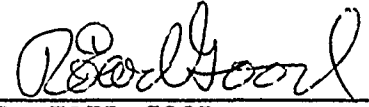
90 06 12 132

"This technical report has been reviewed and
is approved for publication"


WILLIAM A.M. BLUMBERG
CONTRACT MANAGER


GEORGE A. VANASSE
BRANCH CHIEF

FOR THE COMMANDER


R. EARL GOOD
DIVISION DIRECTOR

This report has been reviewed by the ESD Public Affairs Office (PA) and is releasable to the National Technical Information Service (NTIS).

Qualified requestors may obtain additional copies from the Defense Technical Information Center. All others should apply to the National Technical Information Service.

If your address has changed, or if you wish to be removed from the mailing list, or if the addressee is no longer employed by your organization, please notify GL/DAA, Hanscom AFB, MA 01731. This will assist us in maintaining a current mailing list.

Do not return copies of this report unless contractual obligations or notices on a specific document requires that it be returned.

UNCLASSIFIED

SECURITY CLASSIFICATION OF THIS PAGE

| REPORT DOCUMENTATION PAGE | | | | Form Approved OMB No 0704-0188 | |
|--|-------|--|--|--|------------------------------|
| 1a REPORT SECURITY CLASSIFICATION Unclassified | | | 1b RESTRICTIVE MARKINGS | | |
| 2a SECURITY CLASSIFICATION AUTHORITY N/A | | | 3 DISTRIBUTION/AVAILABILITY OF REPORT Approved for public release; distribution unlimited. | | |
| 2b DECLASSIFICATION/DOWNGRADING SCHEDULE N/A | | | | | |
| 4 PERFORMING ORGANIZATION REPORT NUMBER(S) | | | 5 MONITORING ORGANIZATION REPORT NUMBER(S) GL-TR-90-0057 | | |
| 6a. NAME OF PERFORMING ORGANIZATION Massachusetts Institute of Technology | | 6b OFFICE SYMBOL (If applicable) | 7a. NAME OF MONITORING ORGANIZATION Geophysics Laboratory | | |
| 6c ADDRESS (City, State, and ZIP Code) Department of Chemistry Cambridge, Massachusetts 02139 | | | 7b. ADDRESS (City, State, and ZIP Code) Hanscom Air Force Base Bedford, Massachusetts 01731-5000 | | |
| 8a. NAME OF FUNDING / SPONSORING ORGANIZATION | | 8b OFFICE SYMBOL (If applicable) | 9 PROCUREMENT INSTRUMENT IDENTIFICATION NUMBER F19628-86-C-0139 | | |
| 8c ADDRESS (City, State, and ZIP Code) | | | 10 SOURCE OF FUNDING NUMBERS | | |
| | | | PROGRAM ELEMENT NO 61102F | PROJECT NO. 2310 | TASK NO G4 |
| 11 TITLE (Include Security Classification) Formation and Deactivation of Vibrationally Excited Atmospheric Molecules (U) | | | | | |
| 12 PERSONAL AUTHOR(S) J. Steinfeld, C. Fell, C.M. Phillips, J. Klaassen, C. Van Zoeren | | | | | |
| 13a. TYPE OF REPORT Final Technical | | 13b. TIME COVERED FROM 01 Jul 86 to 31 Mar 90 | | 14. DATE OF REPORT (Year, Month, Day) 20 March 1990 | |
| 15. PAGE COUNT 112 | | | | | |
| 16. SUPPLEMENTARY NOTATION | | | | | |
| 17. COSATI CODES | | | 18. SUBJECT TERMS (Continue on reverse if necessary and identify by block number) | | |
| FIELD | GROUP | SUB-GROUP | nitric oxide, multiphoton ionization, nitrogen atom, stimulated-emission pumping, quenching rates, flow kinetics. <i>525</i> | | |
| | | | | | |
| 19 ABSTRACT (Continue on reverse if necessary and identify by block number) Research on the following topics is summarized: (1) quenching of N(² D) atoms by atomic oxygen; (2) reactions of N(² P) atoms; (3) detection of N(⁴ S) atoms by resonantly enhanced multiphoton ionization; (4) a kinetic model for partially saturated, resonantly enhanced multiphoton ionization of diatomic molecules; and (5) stimulated-emission pumping of nitric oxide. —Several directions of future research on these topics are indicated. | | | | | |
| 20 DISTRIBUTION/AVAILABILITY OF ABSTRACT <input checked="" type="checkbox"/> UNCLASSIFIED/UNLIMITED <input type="checkbox"/> SAME AS RPT <input type="checkbox"/> DTIC USERS | | | 21. ABSTRACT SECURITY CLASSIFICATION UNCLASSIFIED | | |
| 22a NAME OF RESPONSIBLE INDIVIDUAL William Blumberg | | | 22b TELEPHONE (Include Area Code) | | 22c. OFFICE SYMBOL GL/OP1 |

CONTENTS

| | <u>Page</u> |
|---|-------------|
| 1. Summary of Research Objectives and Results | 1 |
| 2. Quenching of N(² D) by O(³ P) | |
| 1. Introduction | 5 |
| 2. Experimental | 7 |
| 2.1 Apparatus | 7 |
| 2.2 Experimental Procedure | 9 |
| 3. Analysis of Results | 14 |
| 4. Results and Discussion | 16 |
| 5. Conclusions | 21 |
| Acknowledgements | 23 |
| References | 23 |
| 3. Reactions of N(² P) | |
| 1. N(² P) Kinetics | 39 |
| 2. Results | |
| 2.1 N(² P) + O ₂ Experiments | 39 |
| 2.2 N(² P) + NO/O | 40 |
| 3. Discussion | 42 |
| 4. Conclusions | 42 |
| References | 43 |
| 4. Detection of N(⁴ S) by Resonantly Enhanced Multiphoton Ionization Spectroscopy | 55 |
| 5. A Kinetic Model for Resonantly Enhanced Multiphoton Ionization of NO | |
| 1. Introduction | 59 |
| 2. Methodology | 59 |
| 2.1 The Kinetic Model | 59 |
| 3. Results and Discussion | |
| A. Comparison with Experiment | 62 |
| B. Vibration Subband Relations | 63 |
| C. Correction of Previous Kinetic Results | 64 |
| 4. Conclusions | 64 |
| References | 65 |
| 6. Stimulated-Emission-Pumping of Nitric Oxide | |
| 1. Introduction | 77 |
| 2. Evaluation of Available Pump Sources | |
| 2.1 SEP of NO Using the ArF Excimer Pump | 80 |
| 2.2 SEP of NO Using a Two-Photon Pump | 85 |



| | |
|--------------------|-------------------------------------|
| Session For | |
| S GRA&I | <input checked="" type="checkbox"/> |
| C TAB | <input type="checkbox"/> |
| Unounced | <input type="checkbox"/> |
| ification | |
| Distribution | |
| Availability Codes | |
| Dist | Avail and/or Special |
| A-1 | |

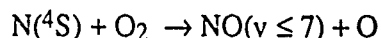
CONTENTS

| | <u>Page</u> |
|--|-------------|
| 3. Experimental | |
| 3.1 Two-Photon Pumping | 86 |
| 3.2 "Two Minus One" SEP | 87 |
| Discussion | 88 |
| References | 90 |
| 7. Recent Developments and Future Applications | |
| 1. REMPI Detection of $N_2(X^1\Sigma^+_g)$ | 101 |
| 2. Identification of Atomic and Molecular Species Generated in Nitrogen Afterglow With SF_6 | 102 |
| 3. FACELIF Modifications | 102 |
| References | 103 |

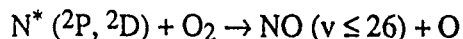
1. Summary of Research Objectives and Results

In this research program, we have been concerned with the reactions of nitrogen atoms under upper-atmosphere conditions. Reactions of $N(^4S)$ and $N^*(^2P, ^2D)$ with molecular oxygen are the major source of vibrationally excited NO in the upper atmosphere, which in turn is responsible for infrared emission in the 5 to 6 μm region. Measurement of the NO production rates and vibrational distributions are carried out in the FACELIF reactor at the Air Force Geophysics Laboratory (Hanscom AFB, Massachusetts) using resonance-enhanced multiphoton ionization (REMPI) detection. The REMPI detection efficiency for N atoms and NO molecules is therefore of considerable interest.

In previous work on this system, the rates and branching ratios in the reaction



were determined; however, an unexpected apparent alternation of rates into neighboring v states required further investigation. Similar measurements for the reaction



would be highly desirable, in order to check infrared chemiluminescence results from the COCHISE reactor. In order to optimize such an experiment, rates for deactivation of the metastable nitrogen atoms by constituents in the flow reactor must be known. During the course of this research, a report appeared from the SRI group [J. Phys. Chem. 92, 5977 (1988)] in which the rate coefficient for the $N(^2D) + O(^3P)$ quenching reaction was reported as $ca. 2 \times 10^{-11} \text{ cm}^3 \text{ sec}^{-1}$ at 300K, considerably larger than previous measurements. We undertook to remeasure this reaction rate in the FACELIF reactor. The $O(^3P)$ atoms were generated by titrating NO directly into the active nitrogen flow. Analysis of the results required that the rate coefficient for the reaction $N(^2D) + NO \rightarrow N_2 + O$ be known accurately, and this was also determined. A finite mixing time correction is also necessary. The best estimate of the rate coefficient from this work is $(6.9 \pm 7, -1.1) \times 10^{-13} \text{ cm}^3 \text{ sec}^{-1}$ at $T = 298 \text{ K}$, considerably smaller than the rate reported by the SRI group and in much better accord with values required by atmospheric models. These results,

described in Section 2 of this report, are in the process of publication in the Journal of Chemical Physics, and complete kinetic data are documented in AFGL technical report.

The mixing-time and other corrections indicated by the work on the $N(^2D) + O$ quenching rate suggested that a previous report by Phillips *et al.* [J. Phys. Chem. **91**, 5001 (1987)], in which the $N(^2P) + O_2$ reaction rate was determined to be $(1.8 \pm 0.2) \times 10^{-12} \text{ cm}^3 \text{ sec}^{-1}$, might also be in error. Preliminary results of a re-measurement of this rate in the FACELIF reactor, described in Section 3, give a value of $\sim 3.4 \times 10^{-12} \text{ cm}^3 \text{ sec}^{-1}$, in much better accord with earlier measurements by Kaufmann and co-workers [J. Chem. Phys. **73**, 4701 (1980)]. However, an independent measurement by Piper *et al.* [private communication] gives a value of $k[N(^2P) + O_2] \sim 2. \times 10^{-12} \text{ cm}^3 \text{ sec}^{-1}$, which agrees with the previous Phillips *et al.* measurement. This issue is unresolved at the present time.

During the course of this work, we observed that $N(^4S)$ atoms could be efficiently detected by Resonantly Enhanced Multiphoton Ionization (REMPI). The magnitude of the ion signal, after correction for laser power dependence, is directly proportional to the $N(^4S)$ concentration and, once calibrated, is a direct and highly sensitive method for $N(^4S)$ concentration measurements in fast-flow kinetics experiments. These results, described in Section 4, are in the process of publication as a Note in Spectrochimica Acta.

It was noted earlier that the vibrational state distribution in the $N(^4S) + O_2$ reaction, as probed by REMPI, showed an unexpected alternation between adjacent vibrational states. It was suggested by C. Feigerle [private communication] that this could be due to partial saturation of the initial ($A \leftarrow X$) absorption step in NO. Accordingly, a detailed kinetic and spectroscopic model for $(1 + 1)$ multiphoton ionization of Hund's case (a) diatomic molecules in this regime was investigated. The model predictions, verified for $NO(v=1)/NO(v=0)$ signal ratios and for REMPI detection of high vibrational levels of $N_2(X^1\Sigma)$ in nitrogen discharges, suggest that the previous measurements of NO vibrational state distributions from the $N(^4S) + O_2$ reaction carried out in the FACELIF reactor do indeed need to be corrected for partial saturation effects to obtain accurate values of $k(v)$. These results, described in Section 5, are being prepared for eventual publication.

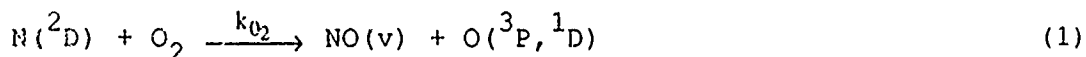
In order to completely reduce the data from FACELIF experiments on $(N + O_2)$ or $(N^* + O_2) \rightarrow NO(v)$, it is also necessary to know vibrational deactivation efficiencies for highly vibrationally excited levels of NO. We have investigated the feasibility of using Stimulated-Emission Pumping (SEP) to generate the high instantaneous densities of $NO(v'')$ required for such measurements. While SEP via the $B(2\Pi)$ state using a commercially available ArF excimer was found not to be feasible, a two-photon-pump scheme via the $A^2\Sigma$ state, followed by stimulated $A \rightarrow X$ emission, did succeed in moving population into $v'' = 4$ levels of the X state, as described in Section 6. However, due to limitations on the availability of laser sources, it was not possible to carry out detailed measurements on $NO(v'')$ state relaxation. In a concluding section, several possible directions for future investigations are indicated.

2. Quenching of $N(^2D)$ by $O(^3P)$

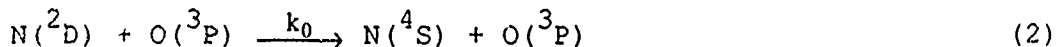
[for publication in the Journal of Chemical Physics, v. 92 (April 15 1990)]

1. Introduction

$N(^2D)$ is an important constituent of the mesosphere and thermosphere. Atmospheric modeling studies¹⁻³ indicate that the reaction



is the primary source of the NO concentrations first observed in rocket experiments⁴. While the value of the rate coefficient for reaction (1) is well established⁵⁻¹⁰, the coefficient for the quenching reaction



is still the subject of some dispute. The relative magnitude of these two rate coefficients is important in determining the partitioning between the two product channels. Modeling calculations require that reaction (1) be the dominant loss channel for $N(^2D)$. A recent experimental measurement¹¹ of the rate coefficient for reaction (2) reported a value of $3.4 \times 10^{-11} \times \exp(-145/T) \text{ cm}^3 \text{ sec}^{-1}$, which would correspond to $2.1 \times 10^{-11} \text{ cm}^3 \text{ sec}^{-1}$ at $T = 300 \text{ K}$; the quoted error limits are on the order of $\pm 50\%$. This value is considerably higher than previous determinations and more discordant with preferred modeling values^{2, 12-15}

which require $k_O < 10^{-12} \text{ cm}^3 \text{ sec}^{-1}$. If this rate were correct, then $\text{N}(^2\text{D})$ would contribute to the overall depletion of NO by enhancing the $\text{N}(^4\text{S})$ concentration which reacts rapidly with NO through the reaction



This would necessitate a re-evaluation of the role of $\text{N}(^2\text{D})$ in the upper atmosphere and the identification of another source term for NO.

We have re-measured the rate coefficients for both reactions (1) and (2) in order to establish the true partitioning between these two $\text{N}(^2\text{D})$ loss channels. This was done using the FACELIF reactor¹⁶ with multi-photon ionization (MPI) detection of reactant and product species. The experimental method makes use of reaction (3) to generate the $\text{O}(^3\text{P})$ atom quenchers¹¹. As this reaction takes place directly in the main flow, recovery of k_O requires that the rate coefficient for the reaction



be known accurately. Reported values^{17,18} for this rate coefficient range from 5.9×10^{-11} to $1.8 \times 10^{-10} \text{ cm}^3 \text{ s}^{-1}$; thus, it was necessary to carry out a measurement of k_{NO} as well, in order to determine the correct value of k_O .

2. Experimental

2.1. Apparatus

The experimental set-up was essentially the same as that used in previous rate measurements performed using the FACELIF reactor¹⁶ and will therefore be described only briefly here. A schematic is shown in Fig.1. The $N(^2D)$ atoms were produced in a 70W microwave discharge of a 1-2% mixture of N_2 in helium. The N_2 and He were purified using gettering furnaces containing Cu at 600° C and Ti at 800° C, respectively, to remove O_2 impurities prior to entering the discharge tube. The NO (Matheson 98% purity) was flowed through a purifying manifold consisting of an ascarite trap and a liquid nitrogen/methanol slurry, and was then diluted with He to ~10% concentration prior to use. All other quenchers were used without further purification.

Metastable nitrogen atoms are deactivated at essentially every wall collision^{6,19}. The $N(^2D)$ concentrations created by microwave discharges are approximately two orders of magnitude lower than the ground state nitrogen atom concentration. The combination of these two factors made it essential, under certain circumstances, to be able to introduce the metastable atoms into the reaction zone as quickly as possible, while the $N(^2D)$ was still in sufficient concentration to provide an adequate signal level. This necessitated a fast pumping speed which was provided by a Roots blower (Leybold-Heraeus WS1000) backed by a large displacement forepump (Heraeus-

Englehard DK180). The maximum linear flow velocity attainable using this configuration was of the order of 6000 cm s^{-1} , which corresponds to a minimum flow time of approximately 2 ms. Longer flow times could be achieved by reducing the pumping speed as required. Quenching gases were injected through a loop injector whose position could be adjusted, over a limited range, along the length of the flow tube, again altering the flow time. Some comparative studies were performed using a perforated ball injector to probe any possible disparities in mixing properties. These indicated that the mixing characteristics were comparable with marginally poorer mixing for the ball injector.

The $\text{N}(^2\text{D})$ concentration was monitored using resonance enhanced multiphoton ionization^{18,19}. The frequency doubled output of a Nd:YAG pumped dye laser (Quanta-Ray DCR2A, PDL-1, WEX-1) was used to photo-ionize $\text{N}(^2\text{D})$, resonantly enhanced by the two-photon transitions at 268.95 and 268.98 nm²⁰. The current produced across a pair of Ni wire grids, biased at 90V, was amplified using an Ithaco model 1211 current preamplifier and averaged on an EG & G model 162 Boxcar Averager. Signal levels were generally measured by setting the laser on resonance at each data point and subtracting the off-resonance baseline from the averaged signal. Some results were also taken by scanning the laser across the resonance lines with no significant difference in the results.

The method used to generate the $\text{O}(^3\text{P})$ quenchers involves the titration of NO directly into the flowtube¹¹. The NO/He mixture is introduced into the flow, through the loop injector, where it reacts rapidly with $\text{N}(^4\text{S})$ ²¹, which is present in high concentrations in

microwave discharge flows of N_2/He . Under ideal conditions, the $N(^4S)$ will be in sufficient excess that all the NO will be rapidly converted to $O(^3P)$ before making any significant contribution to the $N(^2D)$ quenching. The diffusion coefficient for O atoms in He is $700 \text{ cm}^2 \text{ sec}^{-1}$ ²², and the surface recombination coefficient is on the order of 10^{-4} ²³. For the flowspeeds and pressures used in our 2 in. diameter flowtube, we estimate less than 1% loss of $O(^3P)$ over the reaction length.

2.2 Experimental Procedure

Preliminary experiments were carried out investigating the variation in the total $N(^2D)$ quenching rate over a wide range of reaction times. These were used to calculate an effective rate coefficient at each reaction time. This is defined as

$$k_{\text{eff}} = - \alpha(v/d) (d \ln[N(^2D)] / d[Q]) \quad (5)$$

where v is the average flow speed, d is the injector to detector distance, α is the non-laminar flow correction having a numerical value of 1.62 ⁹, and $[Q]$ is the initial quencher concentration. The use of Eq. (5) is equivalent to assuming that all the initially added NO is converted instantaneously to $O(^3P)$ by the $N(^4S)$ without contributing to the $N(^2D)$ decay. The results, shown in Fig.2, display a rapid decrease in the effective rate coefficient with increasing reaction time. Even at ~50ms there is some indication that the rate coefficient is still approaching an asymptotic

value of less than $1 \times 10^{-12} \text{ cm}^3 \text{ s}^{-1}$. The flow conditions over this range of reaction times necessarily varied by a substantial amount. The total pressure varied from 0.2 to 4 Torr in going from short to longer reaction times. There was a corresponding change in the $\text{N}(^4\text{S})$ concentration, although this was not explicitly measured for all points along the curve. The percentage of initially added NO remaining unreacted at the detection point was also measured for the same range of reaction times. The NO $\gamma(0,0)$ MPI signals^{24,25} were used for this purpose. The magnitude of this signal is directly proportional to the NO concentration. A blank titration was performed under the same set of experimental conditions, except with the discharge turned off. The ratio of the two slopes yields a value of the fraction of initially added NO that remains unreacted. The results are shown in Fig.3.

Comparison of Figs. 2 and 3 shows clearly that the faster effective rate constants are correlated with significant residual NO concentrations. The short reaction time measurements represent a region in which reaction with NO dominates the $\text{N}(^2\text{D})$ decay. These measurements indicate an extreme lower limit on k_{NO} . The longer reaction time measurements, to the extent that there is still some NO contribution to the effective decay rate, represent an extreme upper limit on the $\text{O}(^3\text{P})$ quenching rate coefficient. The limiting values obtained for k_{NO} and k_{O} obtained in this way, indicate a ratio for these two rate coefficients in excess of 25 to 1. Consequently, for short reaction times, where $[\text{NO}] \sim [\text{O}]$, the $\text{O}(^3\text{P})$ contribution is smaller by a factor $k_{\text{O}}/k_{\text{NO}}$, and may be legitimately neglected when determining k_{NO} . Conversely, the

large value of k_{NO} compared to k_{O} means that even very small amounts of NO may cause a significant degree of quenching.

It has been reported that REMPI detection of $\text{N}(^2\text{D})$ at 269 nm can generate $\text{N}(^2\text{D})$ through the two photon dissociation of NO ^{26,27}. In order to ensure that this effect was not compromising our results we looked for the characteristic $\text{N}(^2\text{D})$ signal at high NO flow with the discharge turned off (i.e. with [NO] significantly higher than normal operating conditions). No signal was observed until [NO] was over 100 times that used during titrations. The laser power, measured after exiting the flow tube, was $<0.5 \text{ mJ pulse}^{-1}$ compared to the 2-5 mJ pulse^{-1} reported by Jusinski *et al.* ²⁶. This gives a production rate ratio of between 1:16 and 1:100 for the two systems. Also, NO concentrations in the detection region were always $\leq 0.5 \text{ mTorr}$. The combination of these two factors accounts for the lack of any measurable levels of $\text{N}(^2\text{D})$ production from NO dissociation.

Measurements of k_{NO} and k_{O} both require knowledge of $[\text{N}(^4\text{S})]$ to determine how fast the NO is depleted and therefore the extent to which it contributes to the $\text{N}(^2\text{D})$ decay. For long reaction times the standard NO titration method ²⁸ may be used to determine $[\text{N}(^4\text{S})]$ accurately. This technique has serious limitations at the shorter reaction times to which the NO rate coefficient measurements were constrained. To obtain a distinct titration end point, reaction (3) must have sufficient time to go to completion. The method therefore, is best suited to conditions where $[\text{N}(^4\text{S})]$ is high and the reaction time is long. This is precisely the opposite of the requirements for accurate k_{NO}

measurements. Other practical difficulties were encountered in the form of greatly reduced signal levels and interfering fluorescence. The fast flows and consequent low pressures (0.2-0.4 Torr) lead to significantly reduced signal levels and a subsequent reduction in signal to noise. In addition, stray light from the discharge created a background large in comparison to the target signal. Anomalous effects were observed for small NO additions in the form of an initial rise in signal level. It is possible that this has its origins in fluorescence resulting from some coincident reaction. It has been previously reported²⁹ that some short-lived source of $N_2(B)$, other than $N(^4S)$ atom recombination, exists in discharge flows which may interfere with titration measurements.

Attempts were made to fit the titration plots for short reaction times. This introduced a further limitation beyond the practical problems already mentioned. Fitting would require the use of the rate coefficient for reaction (3), which has associated error bounds that will propagate into the $[N(^4S)]$ value. As a result of these limitations, an alternative method of determining $[N(^4S)]$ was devised. Measurements of NO depletion were made using

$\gamma(0,0)$ MPI band intensities, as described earlier. The high sensitivity of MPI to NO enables very small concentrations to be detected and it is therefore possible to work with $[N(^4S)] \gg [NO]$. The NO decay can then be described by the pseudo first-order rate equation

$$[NO] = [NO]_0 \exp(-k_N[N(^4S)]t) \quad (6)$$

where $[\text{NO}]_0$ is the initial concentration of NO added. The $\text{N}(^4\text{S})$ concentration is simply given by

$$[\text{N}(^4\text{S})] = -\ln\{[\text{NO}]/[\text{NO}]_0\}/(k_{\text{N}}t) \quad (7)$$

Since the ratio $[\text{NO}]/[\text{NO}]_0$ may be determined very precisely, the accuracy of this technique is limited by the uncertainty in k_{N} .

For slow flows ($> 20\text{ms}$), it is reasonable to assume that the mixing time is short in comparison to the total flowtime. For very fast flows ($< 5\text{ms}$), this assumption may lead to a significant underestimation of the rate coefficients. A standard technique used to probe mixing effects is to perform rate measurements over a range of injector positions under constant flow conditions. A plot of the decay coefficient as a function of the flowtime will give a straight line whose x-axis intercept gives a value for the effective mixing time and whose slope yields a value for the rate coefficient. In the case of NO, the accompanying reaction with $\text{N}(^4\text{S})$ depletes NO and thus compromises the technique. In order to circumvent this problem, we performed the rate measurements substituting O_2 as a quencher. If it is assumed that the mixing characteristics for O_2 and NO are comparable, then the effective mixing time obtained using O_2 may be applied to NO, provided that identical flow conditions are employed.

3. Analysis of Results

Measurements of both k_{NO} and k_{O} involve injecting NO molecules directly into the main discharge flow, where they react rapidly with $\text{N}(^4\text{S})$ atoms to generate $\text{O}(^3\text{P})$. Whatever the flow conditions, the NO will be present for some finite time in the tube. The $\text{N}(^2\text{D})$ atoms may be quenched by $\text{O}(^3\text{P})$ and NO, both of which will be present in varying concentrations along the length of the flowtube. From reactions (2) and (3), the rate equation describing the decay of $\text{N}(^2\text{D})$ is

$$-d[\text{N}(^2\text{D})]/dt = k_{\text{NO}}[\text{N}(^2\text{D})][\text{NO}] + k_{\text{O}}[\text{N}(^2\text{D})][\text{O}] + k_{\text{W}}[\text{N}(^2\text{D})] \quad (8)$$

where k_{W} is the first order rate coefficient for wall deactivation.

Integration of this equation over the reaction time gives

$$-\ln\{[\text{N}(^2\text{D})]/[\text{N}(^2\text{D})]_0\} = k_{\text{NO}} \int_0^t [\text{NO}]dt + k_{\text{O}} \int_0^t [\text{O}]dt + k_{\text{W}}t \quad (9)$$

where $[\text{N}(^2\text{D})]_0$ is the initial concentration of $\text{N}(^2\text{D})$. The concentration of $\text{O}(^3\text{P})$ at any given time is simply equal to $[\text{NO}]_0 - [\text{NO}]_t$, the amount of NO reacted, if there is no other significant loss of $\text{O}(^3\text{P})$.

The rate of change of NO with time is given by

$$-d[\text{NO}]/dt = k_{\text{N}}[\text{NO}][\text{N}(^4\text{S})] + k_{\text{NO}}[\text{NO}][\text{N}^*] \quad (10)$$

where $[N^*]$ is the metastable nitrogen atom concentration. Since $[N(^4S)] \gg [N^*]$, the second term in equation (10) may be neglected, and the NO concentration is given by Eq. (6). Substituting this into Eq. (9) gives

$$-\ln\{[N(^2D)]/[N(^2D)]_0\} = k_O[NO]_0 t + (k_{NO} - k_O)/k_N [N(^4S)] \times \{1 - \exp(-k_N [N(^4S)] t)\} [NO]_0 \quad (11)$$

For the situation where $[N(^4S)]$ cannot be considered to be in large excess, a slightly more complex expression results. The NO concentration, in this instance, is expressed as

$$-d[NO]/dt = k_N \{ [NO]_0 - [NO]_t \} \{ [N(^4S)]_0 - [NO]_t \} \quad (12)$$

where $[N(^4S)]_0$ is the initial ground state nitrogen atom concentration. This is a second order rate equation which when integrated gives⁶

$$\frac{1}{([NO]_0 - [N(^4S)]_0)} \ln \left\{ \frac{[N(^4S)]_0 ([NO]_0 - [NO]_t)}{[NO]_0 ([N(^4S)]_0 - [NO]_t)} \right\} = k_N t \quad (13)$$

Re-arranging this expression for $[NO]$ gives

$$[\text{NO}]_t = \frac{[\text{N}(^4\text{S})] - [\text{NO}]_0 \frac{[\text{N}(^4\text{S})]}{[\text{NO}]_0} e^{-([\text{NO}]_0 - [\text{N}(^4\text{S})]) k_{\text{N}} t}}{1 - \frac{[\text{N}(^4\text{S})]}{[\text{NO}]_0} e^{-([\text{NO}]_0 - [\text{N}(^4\text{S})]) k_{\text{N}} t}} \quad (14)$$

The $\text{N}(^2\text{D})$ concentration at any point along the flowtube is given by

$$-\ln \left\{ \frac{[\text{N}(^2\text{D})]}{[\text{N}(^2\text{D})]_0} \right\} = k_{\text{NO}} [\text{NO}]_0 t + (k_0 - k_{\text{NO}}) \int_0^t [\text{NO}] dt + \text{const.} \quad (15)$$

$\int_0^{t_{\text{max}}} [\text{NO}] dt$ must be evaluated by numerical integration over the range $t = 0$ to t_{max} where t_{max} is the reaction time corrected for mixing effects.

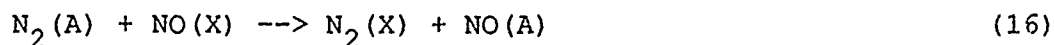
4. Results and Discussion

An estimate of the effective mixing time for the NO kinetic runs was obtained from the O_2 rate measurements. The results are shown in Fig. 4. The total pressure in the flowtube was ~ 0.4 Torr with a

linear flow velocity of $\sim 6000 \text{ cm s}^{-1}$. A weighted linear regression fit to the data yields a value of $(0.48 \pm 0.19) \text{ ms}$ for the effective mixing time. The slope of the line in Fig.4 gives a value of the $\text{N}(^2\text{D}) + \text{O}_2$ rate coefficient of $(5.89 \pm 0.40) \times 10^{-12} \text{ cm}^3 \text{ s}^{-1}$, in good agreement with previous determinations⁵⁻¹⁰.

The NO experiments were carried out using identical flow conditions to those for the O_2 runs. The $\text{N}(^4\text{S})$ concentrations were varied between 0.25 and 0.45 mTorr. For these conditions $\int_0^t [\text{O}] dt \sim \int_0^t [\text{NO}] dt$, but as $k_{\text{NO}} \gg k_{\text{O}}$, the $\text{O}(^3\text{P})$ atom quenching may be neglected. From Eq. (9), a plot of the $\text{N}(^2\text{D})$ signal decay versus $\int_0^t [\text{NO}] dt$ will give a straight line whose slope gives a value for k_{NO} directly. Such a plot is shown in Fig.5 for $t = 3.90 \text{ ms}$ and $[\text{N}(^4\text{S})] = 0.315 \text{ mTorr}$.

There are a number of sources of error that must be considered in calculating k_{NO} . Uncertainties in signal levels are shown as error bars in Fig. 5. The dynamic range of the $\text{N}(^2\text{D})$ decay which could be followed was limited by the appearance of the NO $\gamma(0,4)$ band at higher NO concentrations, which obscured the $\text{N}(^2\text{D})$ signal to some extent. This baseline variation is reflected in the larger error bars for high $[\text{NO}]$ additions. The vibrationally excited NO population is presumably the result of the reaction³⁰



followed by γ -band emission, although this has not been confirmed experimentally.

The value used for k_N in the calculations is taken from the literature²¹ and has an associated uncertainty of $\pm 26\%$. This value is used in calculating $[N(^4S)]$ and again in the integration of $\int_0^t [NO] dt$. This error manifests itself as a shift in the x-axis position of the data points. The extreme values for k_N , $[N(^4S)]$, and t_{max} were used to calculate upper and lower bounds for k_{NO} . These bounds are shown in Fig. 6 for the data shown in Fig. 5. The upper and lower bounds, together with rate coefficient obtained using the mean values of k_N , $[N(^4S)]$ and t_{max} , are given in Table 1 for all kinetic runs. The error limits on each value are the statistical errors ($\pm 1 \sigma$) obtained from a weighted linear regression fit to the data points in each limit. These are small in comparison to the error bounds indicating that the dominant source of error arises from the uncertainty in the values of k_N and the mixing time. The final values are obtained by taking the weighted mean of all kinetic runs. This procedure yields a result of $(6.70, +1.36, -1.21) \times 10^{-11} \text{ cm}^3 \text{ s}^{-1}$ for k_{NO} .

The ideal conditions in which to measure k_0 are at long reaction times with $[NO] \ll [N(^4S)]$. If these conditions can be fulfilled then Eq. (11) may be used to evaluate k_0 . Given the great disparity between k_{NO} and k_0 , these conditions are extremely difficult to realize in practice. At the slowest flows, the use of high flow tube pressures was not sufficient to offset the loss of signal due to increased wall deactivation, thus constraining the experimental range of t . The maximum $[N(^4S)]$ values obtained, even under these extreme conditions, were $1.6 \times 10^{14} \text{ cm}^{-3}$ ($\sim 5 \text{ mTorr}$). The low value of k_{NO} required NO additions of up to 3.5 mTorr to

give $[N(^2D)]/[N(^2D)]_0 < 0.05$ and thus the $[N(^4S)] \gg [NO]$ condition could not be met. Some attempts were made to enhance N-atom dissociation by adding SF_6 to the discharge flow³¹. This did result in a significant increase in $[N(^4S)]$ (by a factor of up to 2.5) and also in the $N(^2D)$ signal level. Unfortunately, the use of SF_6 also resulted in the appearance of a large molecular MPI spectrum in the same frequency range which also varied with quencher concentration and therefore compromised the results. It is possible that such interferences would not occur for other $N(^2D)$ detection methods. If this were true, then this method could be used to enhance both $N(^4S)$ and $N(^2D)$, assuming that the species generated by discharging SF_6 do not participate in the chemistry in any way.

Eq. (15) was used in calculating k_0 . The previously determined value of k_{NO} was used and the NO contribution to the decay subtracted at each point. Figs. 7 and 8 show the effect of applying this correction to the raw data for two separate kinetic runs. The relative contribution from NO increases with increased quencher addition and shorter reaction time. Even for the highest $[N(^4S)]$ values and longest flowtimes, NO accounted for ~30% of the $N(^2D)$ decay.

The $N(^4S)$ concentration can be measured by the more usual titration technique for these slow flow conditions. $[N(^4S)]$ was measured before and after each kinetic run with results agreeing to within 2% in all instances. We conservatively estimate an accuracy of $\pm 5\%$ for the NO titration technique. The mixing time

was not explicitly measured for these longer reaction times as this can reasonably be expected to be short compared to the flowtime. Given the long flowtime and large $N(^4S)$ concentration, $\int_0^t [O]dt \rightarrow [NO]_0 t$ and the correction for the NO contribution to the decay involves primarily a y-axis adjustment. The magnitude of this adjustment is sensitive to the exact values used for k_N and k_{NO} . In the interests of self-consistency within the analysis, when one extreme value of k_N was taken in the error calculation, the value of k_{NO} calculated using that same value was used. Thus the k_N and k_{NO} errors are correlated and, in this instance, tend to cancel one another. The measurement of k_O is therefore less sensitive to the uncertainty in k_O than is k_{NO} . The error bounds for k_O were calculated using the extreme values of $[N(^4S)]$, k_N , and k_{NO} . The results are shown in Figs. 9 and 10 for the data in Figs. 7 and 8, respectively. The results of twelve separate kinetic runs are given in Table 2. As before, the errors quoted for each value are the statistical values in each limit and are small compared to the uncertainties arising from the correlated systematic errors. The weighted averages of these data give a value for k_O of $(6.93 + 0.71, -1.08) \times 10^{-13} \text{ cm}^3 \text{ s}^{-1}$. The absence of any systematic variation in k_O with t confirms that there is no significant loss of $O(^3P)$ along the flow tube. The O_2 formed would react rapidly with $N(^2D)$, giving an apparent increase in k_O at longer reaction times.

5. Conclusions

The previously reported experimental and modeling values of k_0 are listed in Table 3. The value of k_0 reported here is in good agreement with the most recent experimental measurement made by Piper³², who utilized $O(^3P)$ atom generation and $N(^2D)$ detection techniques differing from those employed here. It is also in fair agreement with the earlier results of Davenport et al.³³ and Ianuzzi et al.⁹. The major conflict is with the result of Jusinski et al.¹¹, who recently rekindled the ongoing controversy regarding the disparity between experimental measurements and the preferred modeling values by suggesting that the true rate was of the order of $2.1 \times 10^{-11} \text{ cm}^3 \text{ s}^{-1}$. The experiment by Jusinski et al. and the studies reported here were performed using an essentially identical experimental set-up and methodology. The origin of the disparity in the results is not immediately apparent although it is interesting to note that our preliminary investigations (as illustrated in Fig. 2) also yield a value of $k_{\text{eff}} \sim 2 \times 10^{-11} \text{ cm}^3 \text{ sec}^{-1}$ at $t = 7.5 \text{ ms}$. Our results and calculations indicate that, for the conditions reported in ref. 11 ($[N(^4S)] = 10 \text{ mTorr}$, $t = 7.5 \text{ ms}$), an effective rate constant (which is what was actually reported) of $\sim 2 \times 10^{-12} \text{ cm}^3 \text{ s}^{-1}$ should be observed. The order of magnitude difference cannot be accounted for by any reasonable adjustment for poor mixing. It is possible that the faster rate observed is the result of the quenching of some precursor which is the dominant $N(^2D)$ source in their higher pressure system ($\sim 30 \text{ Torr}$). The non-linearity observed in some of their plots would tend to support this hypothesis.

The method of generating $O(^3P)$ atoms necessarily means that NO molecules will be present in the flow for some finite time. As k_{NO} turns out to be nearly two orders of magnitude larger than k_O , this will always be significant although, by carefully controlling the experimental conditions, the NO contribution can be kept to a minimum. It is essential that the flow conditions be precisely characterised for each kinetic run, and that the analysis carried out with extreme care, if meaningful results are to be recovered. This also applies to the NO results. In this instance, the requirement that the measurements be carried out at very short reaction times brings us to the limits of flow tube technology. The mixing time, using standard injectors and flows, becomes a significant fraction of the total flow time and must be carefully considered to avoid reporting artificially low values. The accuracy of the reported value of k_{NO} is primarily dictated by the confidence limits associated with k_N . Should a more precise value of k_N become available, the confidence limits on k_{NO} may be reduced accordingly.

Experimental measurements of k_O encounter a number of difficulties, the most immediate of which are, the generation of a pure source of $O(^3P)$ atoms, their transportation to the reaction zone and the subsequent efficient mixing of the reactants. The method of titrating NO directly into the flow tube ingeniously solves the transportation and mixing difficulties but introduces an additional complication as the $O(^3P)$ precursor itself is a highly reactive impurity. With precise characterisation of flow conditions and careful analysis of

results, an accurate value for k_O can be recovered.

Recent models for atmospheric NO concentrations have tended to favor larger values of k_O , and it would appear that experiment and theory have finally reached a consensus regarding the preferred value of this rate coefficient. Bates³⁴ has shown that the fast rate coefficient reported by Jusinski et al.¹¹ is incompatible with observed data on OI red line emission at 630 nm. Also, the most recent modeling calculation by Fesen³⁵ successfully accounts for observed NO distributions using a value of $k_O = 1 \times 10^{-12} \text{ cm}^3 \text{ s}^{-1}$, which coincides with the most recent experimental determinations.

Acknowledgements

This research was performed under contract F19628-86-C-0139 from the Air Force Geophysics Laboratory, and sponsored by the Air Force Office of Scientific Research under Task 2310G4. We thank Dr. Tom G. Slanger (SRI International) and Dr. Larry Piper (Physical Sciences Inc.) for very useful discussions.

References

1. R.B.Norton and C.A.Bart, J. Geophys. Res. **65**, 1469 (1970).
2. D.F.Strobel, D.N.Hunten and M.B.McElroy, J. Geophys. Res. **75**, 4307 (1970).
3. D.W.Rusch, J. Geophys. Res. **78**, 5676 (1973).
4. C.A.Barth, J. Geophys. Res. **69**, 3301 (1964).
5. L.G.Piper, M.E.Donahue and W.T.Rawlins, J. Phys. Chem. **91**,

- 3883 (1987).
6. C.-L.Lin and F.Kaufman, J. Chem. Phys. **55**, 3760 (1971).
 7. T.G.Slanger, B.J.Wood and G.Black, J. Geophys. Res. **76**, 8430 (1971).
 8. G.Black, T.G.Slanger, G.A. St. John and R.A.Young, J. Chem. Phys. **51**, 116 (1969).
 9. M.P.Ianuzzi and F.Kaufman, J. Chem. Phys. **73**, 4701 (1980).
 10. B.Fell, I.V.Riva and D.L.McFadden, J. Phys. Chem. **85**, 224 (1981).
 11. L.E.Jusinski, G.Black and T.G.Slanger, J. Phys. Chem. **92**, 5977 (1988).
 12. E.S.Oran, P.S.Julienne and P.F.Strobel, J. Geophys. Res. **80**, 3068 (1975).
 13. J.E. Frederick and D.W. Rusch, J. Geophys. Res. **82**, 3509 (1977).
 14. T.E. Cravens, J.C. Gerard, A.I. Stewart and D.W. Rusch, J. Geophys. Res. **84**, 2675 (1979).
 15. D.W.Rusch and J.C.Gerard, J. Geophys. Res. **85**, 1285 (1980).
 16. I.C.Winkler, R.A.Stachnik, J.I.Steinfeld and S.M.Miller, J. Chem. Phys. **85**, 890 (1986).
 17. D.Husain, S.K.Mitra and A.N.Young, J. Chem. Soc. Faraday Trans. II **70**, 1721 (1974).
 18. G.Black and L.E.Jusinski, Chem. Phys. Lett., **139**, 41 (1987).
 19. C.M.Phillips, J.I.Steinfeld and S.M.Miller, J. Phys. Chem. **91**, 5001, (1987).
 20. C.E.Moore, "Atomic Energy Levels", Vol. I, NSRDS-NBS35, U.S. Government Printing Office (Washington, D.C., 1971).

21. J.H.Lee, J.V.Michael, W.A.Payne and L.Steif, J. Chem. Phys. **69**, 3069 (1978).
22. J.E. Morgan and H.F. Schiff, Can J. Chem. **42**, 2300, (1964).
23. G. Black and T.G. Slanger, J. Chem. Phys., **74**, 6517, (1981).
24. H.Zacharias, M.M.T.Loy, P.A.Roland and Aa.S.Sudbo, J. Chem. Phys. **81**, 3148 (1984).
25. I.C.Winkler, R.Stachnik, J.I.Steinfeld and S.M.Miller, Spectrochim. Acta **A42**, 339 (1986).
26. L.E. Jusinski, G.E. Gadd, G. Black and T.G. Slanger, J. Chem. Phys. **90**, 4282 (1982).
27. G.E. Gadd, L.E. Jusinski and T.G. Slanger, J. Chem. Phys., **91**, 3378 (1989).
28. H.C.Yang and T.M.Niemczyk, Anal. Chem. **58**, 2492 (1986).
29. L.G.Piper, Report No. PSI-050-TR-509 (Physical Sciences Inc., Wakefield, Mass., 1985).
30. L.G.Piper, L.M.Cowles and W.T.Rawlins, J. Chem. Phys. **85**, 3369 (1986).
31. R.A.Young, R.L.Sharpless and R.Stringham, J. Chem. Phys. **40**, 117 (1964).
32. L.G.Piper J. Chem. Phys. **91**, 3516 (1989).
33. J.E.Davenport, T.G.Slanger and G.Black, J. Geophys. Res. **81**, 12 (1976).
34. D.R. Bates, Planet Space Sci., **37**, 1145 (1989).
35. C.G.Fesen, J.C.Gerard and D.W.Rusch, J. Geophys, Res. **94**, 5419 (1989).
36. P.G. Richards, D.G. Torr, M.R. Torr, J. Geophys. Res **86**, 1495 (1981).

Table I. Kinetic Data for Determination of $\text{N}(^2\text{D}) + \text{NO} \rightarrow \text{N}_2 + \text{O}$ Rate Coefficient

| t, ms | $k_{\text{NO}}, \text{ cm}^3 \text{ molecule}^{-1} \text{ sec}^{-1} \times 10^{-11}$ | | |
|---------------|--|-----------------|------------------|
| | lower bound | mid-range | upper bound |
| 1.82 | 6.11 ± 0.18 | 7.72 ± 0.22 | 8.79 ± 0.26 |
| | 6.65 ± 0.28 | 8.52 ± 0.36 | 9.73 ± 0.41 |
| 2.625 | 7.38 ± 0.31 | 8.77 ± 0.37 | 10.30 ± 0.43 |
| | 7.53 ± 0.30 | 8.88 ± 0.35 | 10.60 ± 0.42 |
| 3.175 | 5.81 ± 0.22 | 7.13 ± 0.27 | 8.89 ± 0.34 |
| | 6.64 ± 0.40 | 8.24 ± 0.50 | 10.40 ± 0.63 |
| 3.385 | 6.56 ± 0.30 | 7.84 ± 0.36 | 9.47 ± 0.43 |
| | 6.56 ± 0.26 | 7.76 ± 0.31 | 9.28 ± 0.37 |
| 3.865 | 4.39 ± 0.18 | 5.13 ± 0.22 | 6.06 ± 0.25 |
| | 4.61 ± 0.24 | 5.38 ± 0.28 | 6.38 ± 0.33 |
| 3.895 | 4.61 ± 0.13 | 5.67 ± 0.16 | 7.15 ± 0.20 |
| | 5.00 ± 0.18 | 6.13 ± 0.22 | 7.63 ± 0.27 |
| Weighted mean | 5.49 ± 0.07 | 6.70 ± 0.08 | 8.06 ± 0.10 |

Table II. Kinetic Data for Determination of $N(^2D) + O(^3P)$ Rate Coefficient

| t, ms | $k_O, \text{cm}^3 \text{ molecule}^{-1} \text{ sec}^{-1} \times 10^{-13}$ | | |
|---------------|---|------------------------|--------------------------|
| | lower bound ^a | mid-range ^b | upper bound ^c |
| 23 | 4.74 ± 0.37 | 7.60 ± 0.37 | 9.17 ± 0.37 |
| | 3.37 ± 0.50 | 6.38 ± 0.49 | 8.03 ± 0.49 |
| 31.7 | 5.33 ± 0.23 | 6.81 ± 0.23 | 7.57 ± 0.23 |
| | 5.08 ± 0.31 | 6.78 ± 0.31 | 7.64 ± 0.31 |
| 36.1 | 7.12 ± 0.26 | 8.51 ± 0.26 | 9.27 ± 0.26 |
| | 6.01 ± 0.24 | 7.44 ± 0.24 | 8.27 ± 0.24 |
| 41.4 | 6.62 ± 0.21 | 7.58 ± 0.21 | 8.14 ± 0.21 |
| | 6.01 ± 0.26 | 6.99 ± 0.26 | 7.53 ± 0.26 |
| 44.8 | 5.46 ± 0.28 | 6.21 ± 0.27 | 6.63 ± 0.27 |
| | 5.32 ± 0.28 | 6.09 ± 0.28 | 6.52 ± 0.28 |
| 55 | 6.19 ± 0.17 | 6.65 ± 0.17 | 6.90 ± 0.17 |
| | 5.54 ± 0.23 | 6.05 ± 0.23 | 6.33 ± 0.23 |
| Weighted mean | 5.85 ± 0.08 | 6.93 ± 0.08 | 7.64 ± 0.08 |

^aUsing $k_N = 2.5 \times 10^{-11} \text{ cm}^3 \text{ sec}^{-1}$,

^bUsing $k_N = 3.4 \times 10^{-11} \text{ cm}^3 \text{ sec}^{-1}$

^cUsing $k_N = 4.3 \times 10^{-11} \text{ cm}^3 \text{ sec}^{-1}$

$k_{NO} = 5.49 \times 10^{-11} \text{ cm}^3 \text{ sec}^{-1}$

$k_{NO} = 6.70 \times 10^{-11} \text{ cm}^3 \text{ sec}^{-1}$

$k_{NO} = 8.06 \times 10^{-11} \text{ cm}^3 \text{ sec}^{-1}$

Table III. Experimental and a Representative Sample of Modeling Determinations of k_0

| | k_0 , $\text{cm}^3\text{sec}^{-1}$ | Source | Reference |
|--------------|--------------------------------------|-----------------------------------|-----------|
| Experimental | $(1.8 \pm 0.6) \times 10^{-12}$ | Davenport <u>et al.</u> (1976) | 33 |
| | $< 1.8 \times 10^{-12}$ | Ianuzzi & Kaufman (1980) | 9 |
| | $(2.1 \pm 0.8) \times 10^{-11}$ | Jusinski <u>et al.</u> (1988) | 11 |
| | $(1.06 \pm 0.26) \times 10^{-12}$ | Piper (1988) | 32 |
| | $(6.9 \pm 1.0) \times 10^{-13}$ | this work | |
| Modeling | 1×10^{-12} | Strobel <u>et al.</u> (1970) | 2 |
| | $< 10^{-14}$ | Oran <u>et al.</u> (1975) | 12 |
| | $4 \cdot 10^{-13}$ | Frederick & Rusch (1977) | 13 |
| | $1 \cdot 10^{-12}$ | Cravens <u>et al.</u> (1979) | 14 |
| | $4 \cdot 10^{-13}$ | Rusch & Gerard (1980) | 15 |
| | $6 \cdot 10^{-13}$ | Richards <u>et al.</u> (1981) | 36 |
| | $\sim 1 \times 10^{-12}$ | Fesen <u>et al.</u> (1989) | 35 |

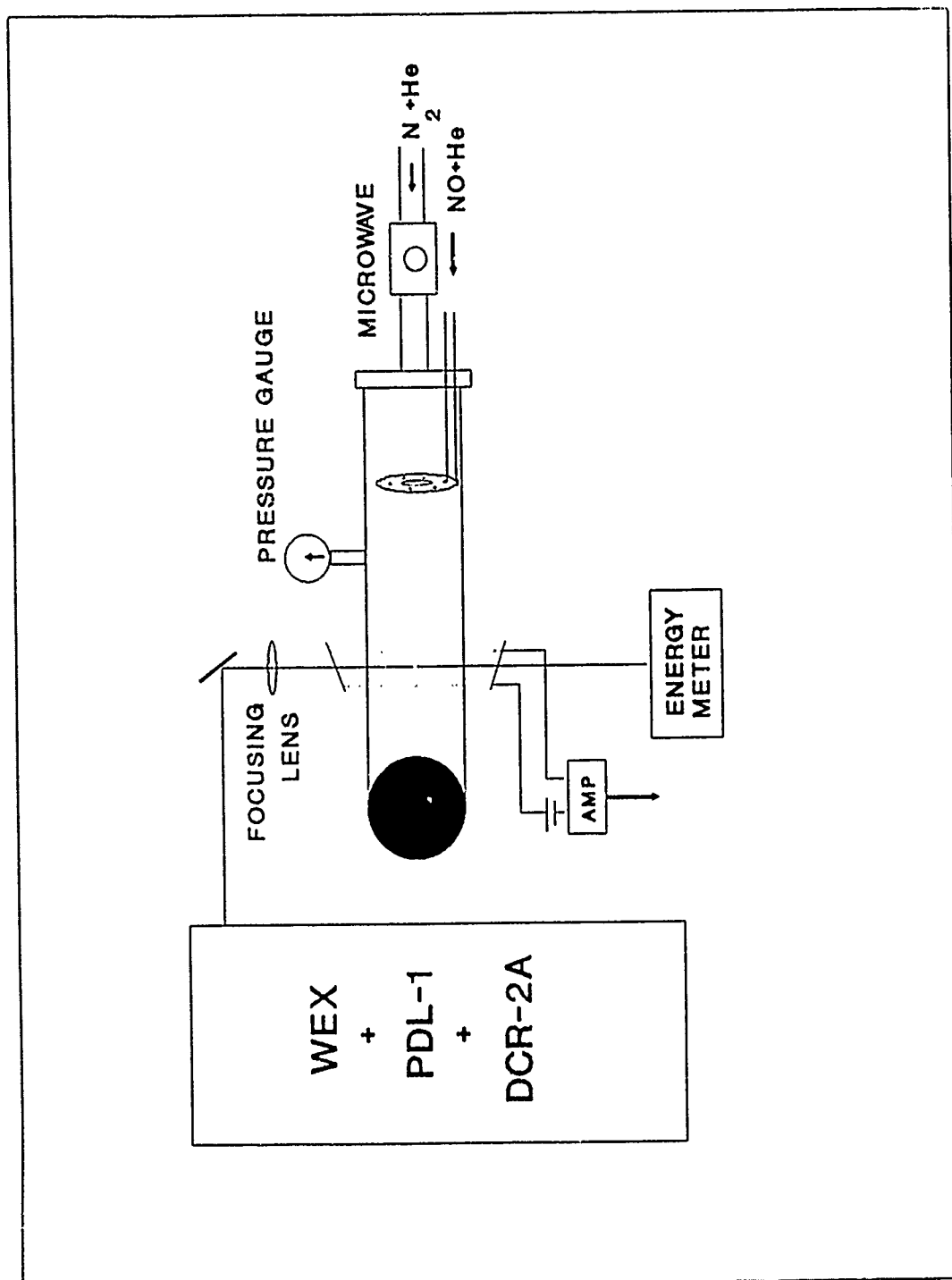


Figure 1. Schematic of FACELIF experimental apparatus. The solid circle represents a right angle connection to the pumping system.

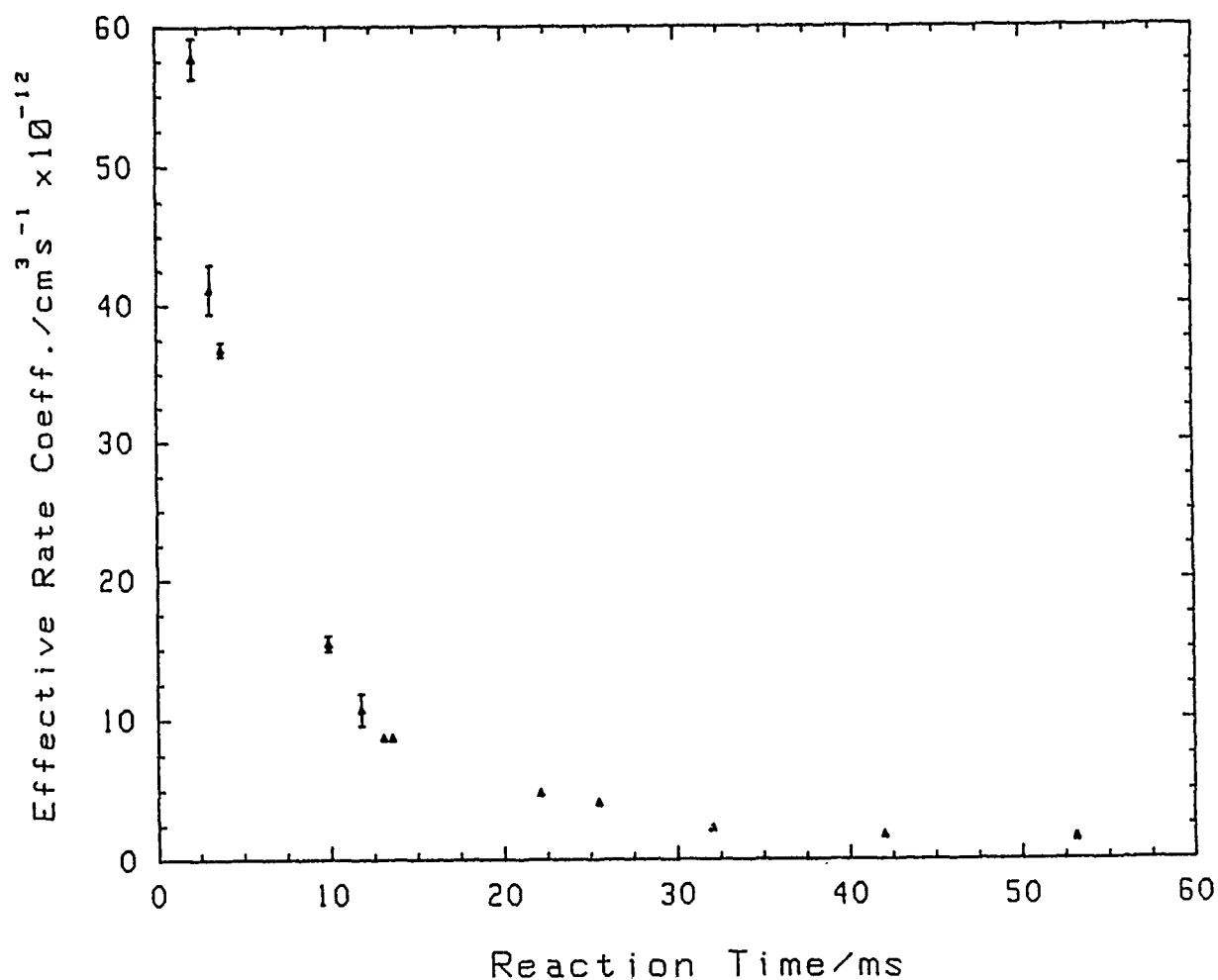


Figure 2. Variation in the effective rate coefficient, k_{eff} (Eq. (5)) with reaction time. The reaction time was varied by adjustments to the injector position and the flow speed. Consequently, the flow conditions (i.e. total pressure, $[N(^4S)]$ etc.) varied with the reaction time.

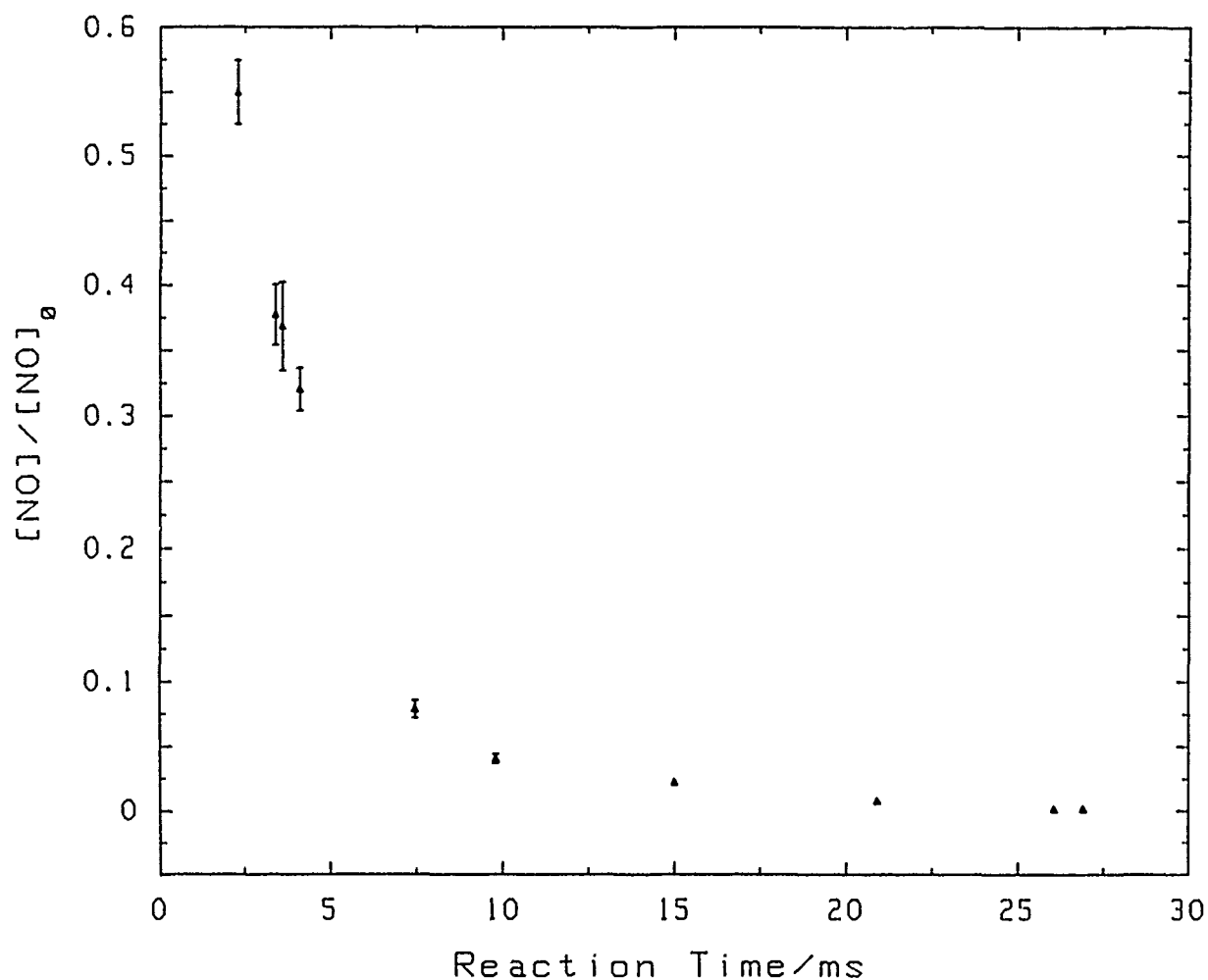


Figure 3. Variation in the fractional amount of initially added NO that remained unreacted at the MPI-detection point. As with the k_{eff} measurements, flow conditions varied with reaction time.

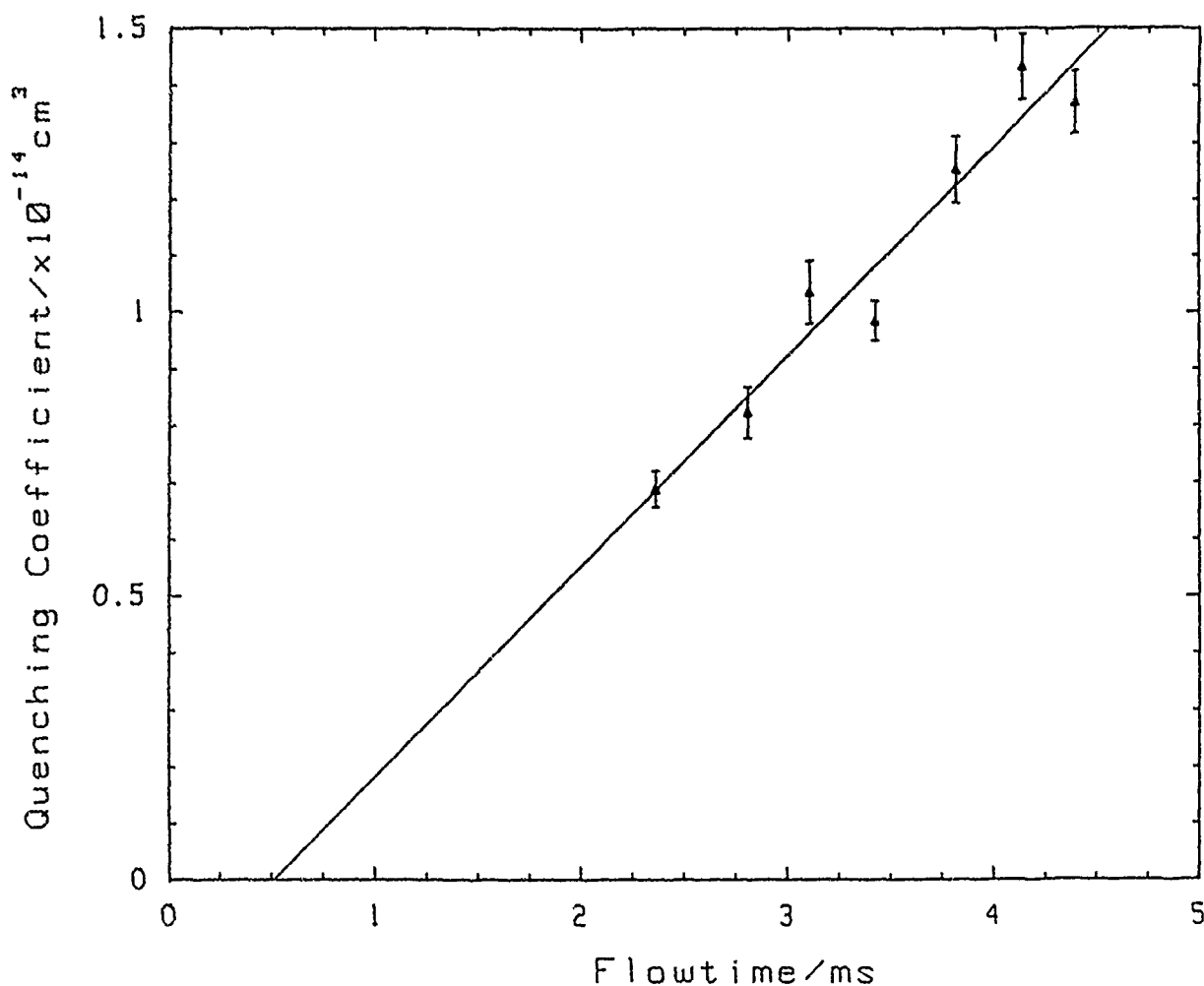


Figure 4. Variation in the decay coefficient ($-\text{dln}[N(^2\text{D})]/\text{d}[\text{O}_2]$) with reaction time for $N(^2\text{D})$ quenching by O_2 . Flowtube pressure was 0.46 Torr at a linear flow velocity of 6700 cm s^{-1} . The error bars represent the statistical limits to the decay coefficient obtained from a weighted linear regression fit to the individual data sets.

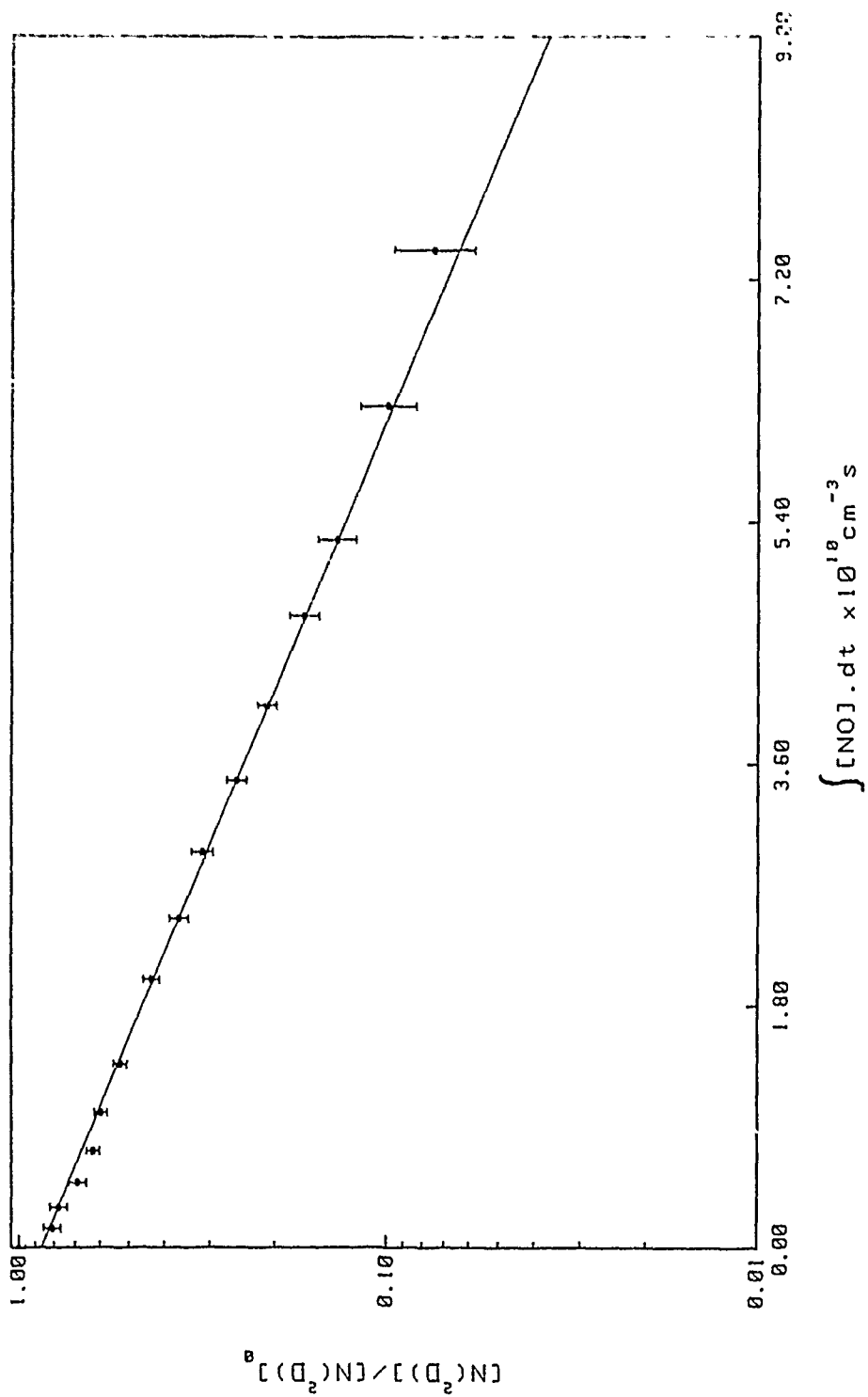


Figure 5. Decay of the $\text{N}(^2\text{D})$ MPI-signal as a function of $\int_0^t [\text{NO}].dt$, which was calculated by numerical integration of Eq. (14). $t = 3.90\text{ms}$ (corrected for 0.48ms mixing time), $k_N = 3.4 \times 10^{-11} \text{ cm}^3 \text{ s}^{-1}$, and $[\text{N}(^4\text{S})] = 0.43\text{mTorr}$.

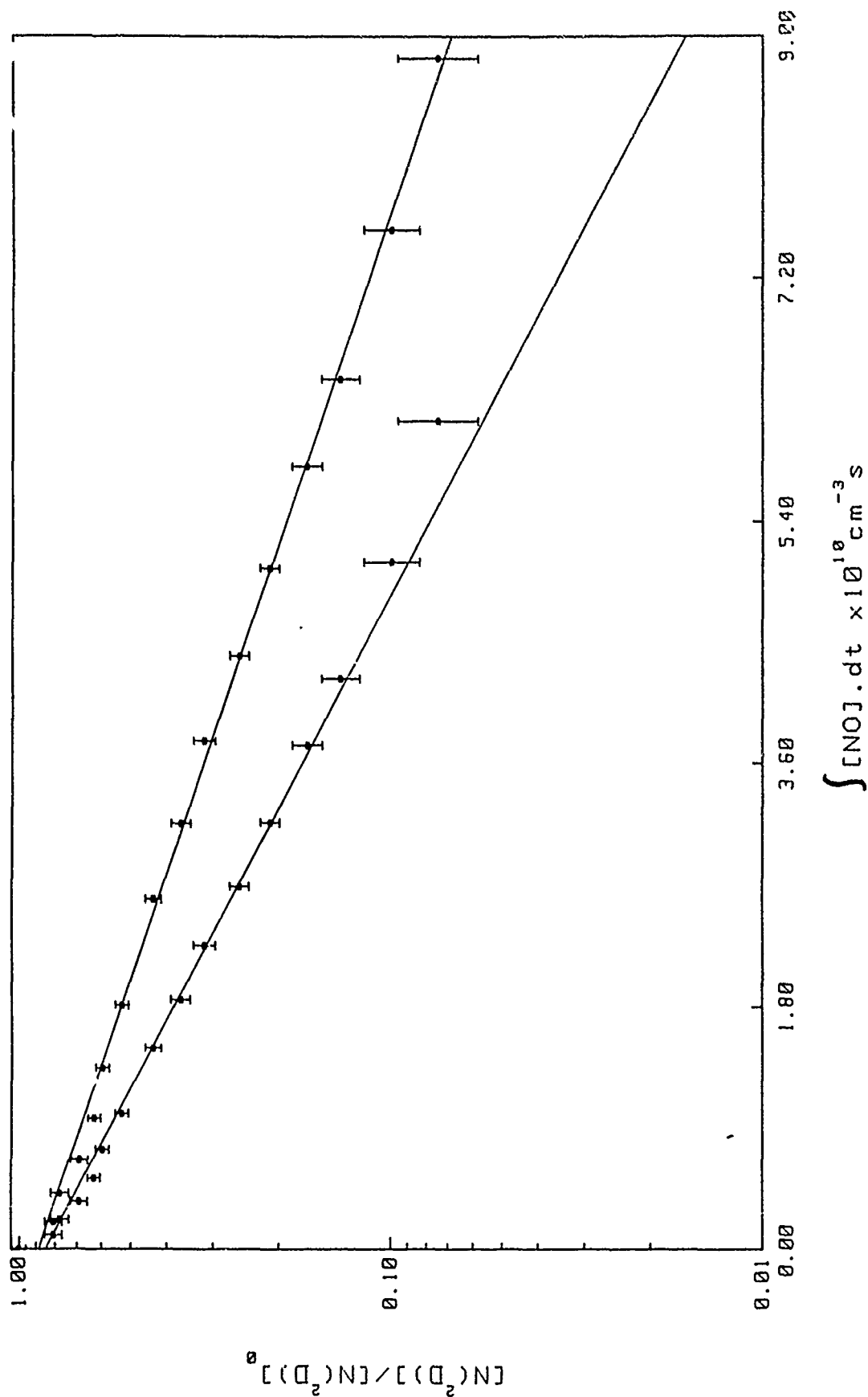


Figure 6. Error bounds on the decay of the $N(^2D)$ MPI-signal as a function of $\int_0^t [NO]dt$ for the data shown in Fig. 5. Lower trace: $t = 3.71\text{ms}$, $k_N = 4.3 \times 10^{-11} \text{ cm}^3 \text{ s}^{-1}$ and $[N(^4S)] = 0.52\text{mTorr}$. Upper trace: $t = 4.09\text{ms}$, $k_N = 2.5 \times 10^{-11} \text{ cm}^3 \text{ s}^{-1}$ and $[N(^4S)] = 0.34\text{mTorr}$.

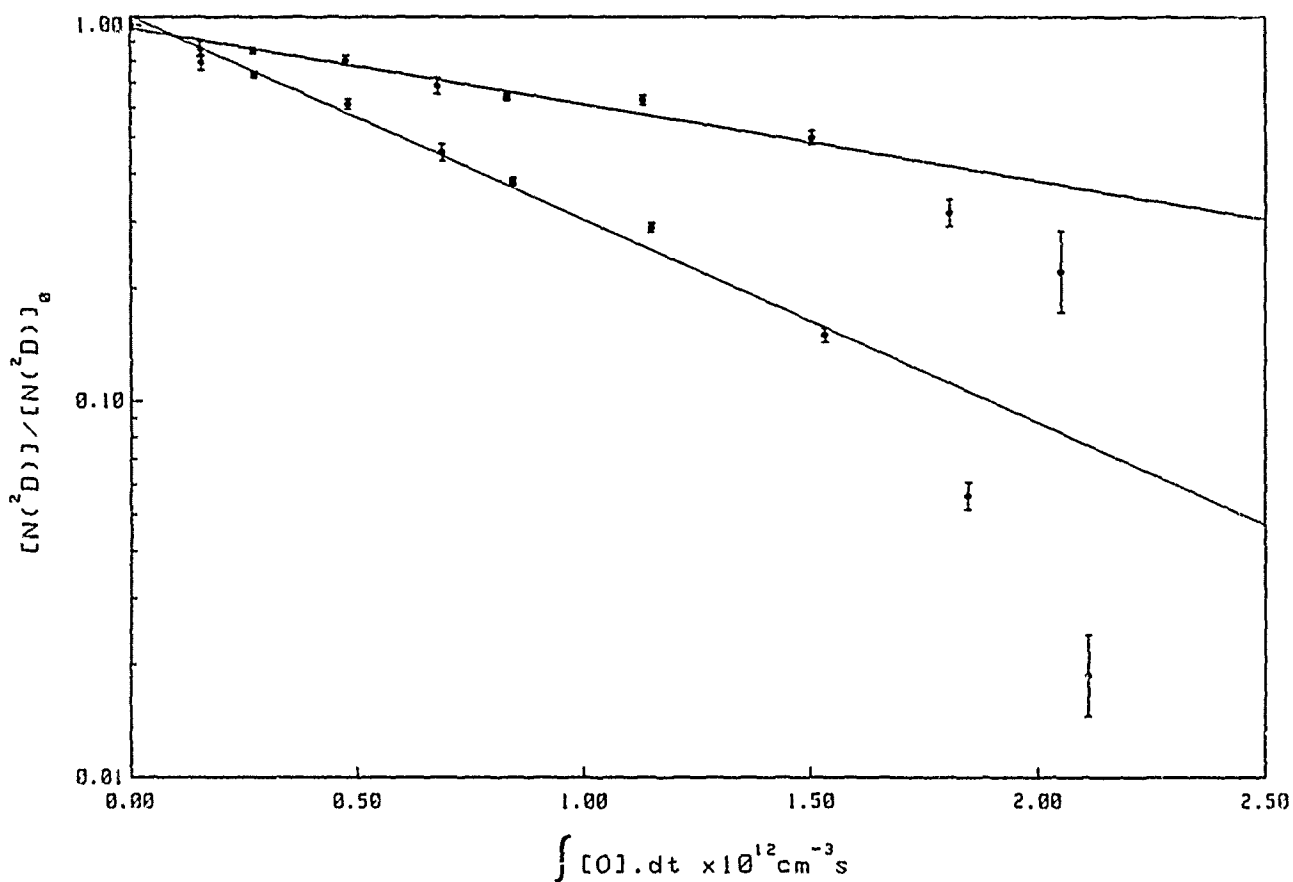


Figure 7. Decay of the $N(^2D)$ MPI-signal as a function of $\int_0^t [O]dt$. The bottom trace was calculated assuming instantaneous conversion of $[NO]$ to $[O]$ (i.e., $\int_0^t [O]dt = [NO]_0 t$) and therefore no correction for depletion of $N(^2D)$ by NO is necessary. A linear regression fit to these data gives a value of $k_O = 2.03 \times 10^{-12} \text{ cm}^3 \text{ s}^{-1}$. The upper trace was calculated using Eq. (15) with $k_N = 3.4 \times 10^{-11} \text{ cm}^3 \text{ s}^{-1}$, $k_{NO} = 6.7 \times 10^{-11} \text{ cm}^3 \text{ s}^{-1}$, $[N(^4S)] = 3.28 \text{ mTorr}$ and $t = 23.0 \text{ ms}$. This gives a value of $k_O = 7.60 \times 10^{-13} \text{ cm}^3 \text{ s}^{-1}$. The difference in the two plots shows the relative magnitude of the NO contribution to the $N(^2D)$ signal decay.

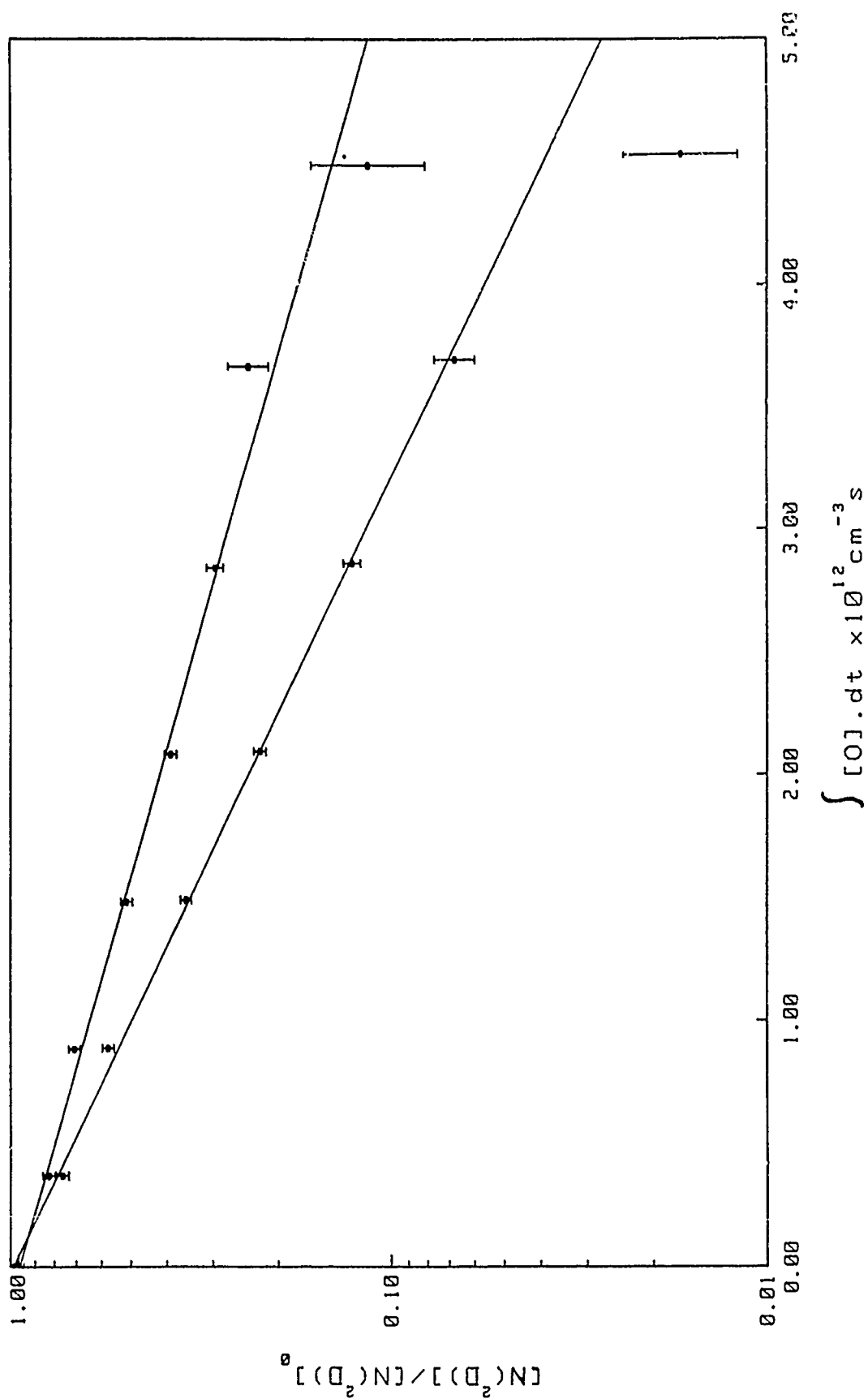


Figure 8. Same as Fig.7 for $t = 41.4 \text{ ms}$. The top trace was calculated using $k_N = 3.4 \times 10^{-11} \text{ cm}^3 \text{ s}^{-1}$, $k_{NO} = 6.7 \times 10^{-11} \text{ cm}^3 \text{ s}^{-1}$ and $[N(^4S)] = 4.28 \text{ mTorr}$.

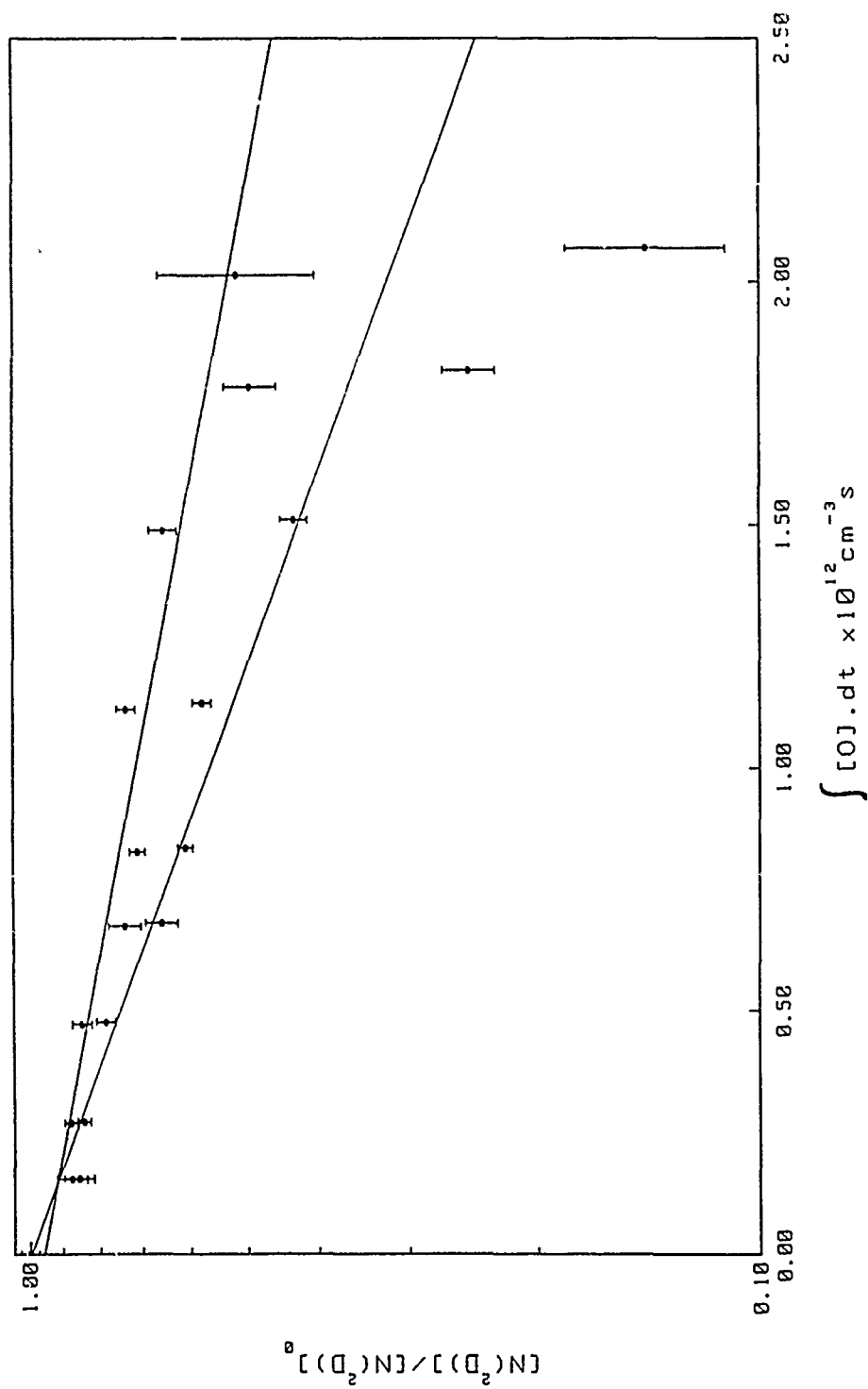


Figure 9. Upper and lower bounds to $N(^2D)$ decay as a function of $\int_0^t [O] dt$ for the data shown in Fig. 7. Lower trace: $k_N = 4.3 \times 10^{-11} \text{ cm}^3 \text{ s}^{-1}$, $k_{NO} = 8.06 \times 10^{-11} \text{ cm}^3 \text{ s}^{-1}$ and $[N(^4S)] = 3.44 \text{ mTorr}$. Upper trace: $k_N = 2.5 \times 10^{-11} \text{ cm}^3 \text{ s}^{-1}$, $k_{NO} = 5.49 \times 10^{-11} \text{ cm}^3 \text{ s}^{-1}$ and $[N(^4S)] = 3.12 \text{ mTorr}$.

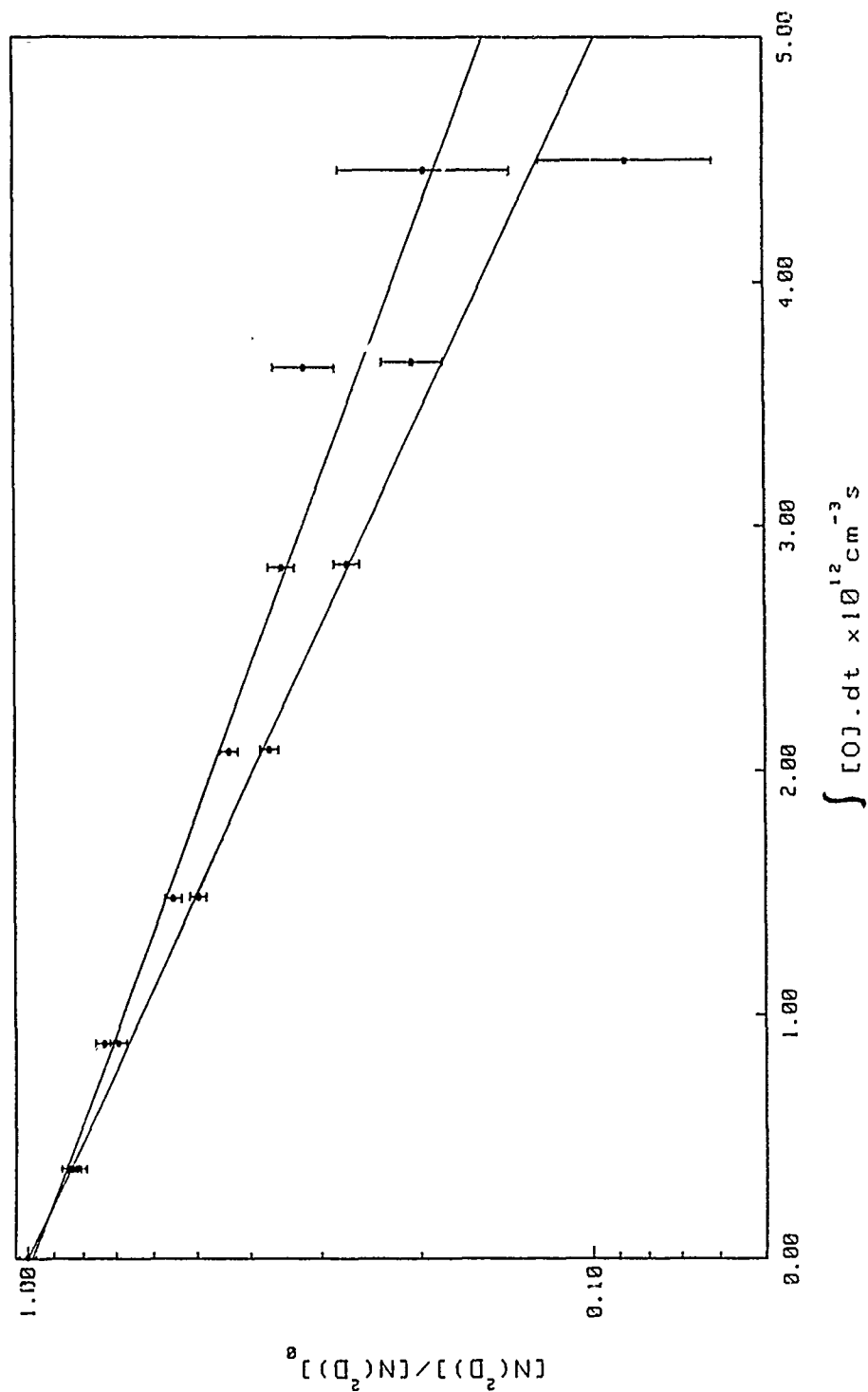


Figure 10. Upper and lower bounds for $N(^2D)$ decay as a function of $\int_0^t [O]dt$ for the data shown in Fig. 8. Lower trace: $k_N = 4.3 \times 10^{-11} \text{ cm}^3 \text{ s}^{-1}$, $k_{NO} = 8.06 \times 10^{-11} \text{ cm}^3 \text{ s}^{-1}$ and $[N(^4S)] = 4.49 \text{ mTorr}$. Upper trace: $k_N = 2.5 \times 10^{-11} \text{ cm}^3 \text{ s}^{-1}$, $k_{NO} = 5.49 \times 10^{-11} \text{ cm}^3 \text{ s}^{-1}$ and $[N(^4S)] = 4.01 \text{ mTorr}$.

3. Reactions of $N(^2P)$

3.1. $N(^2P)$ Kinetics

$N(^2P)$ kinetics may be investigated using an identical experimental set-up to that used for $N(^2D)$ studies. MPI detection of $N(^2P)$ utilizes the two photon transition¹

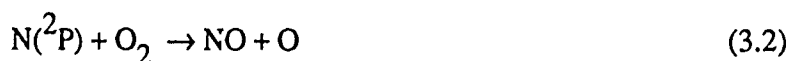


at 290 nm with a third photon then ionizing the atom. Measurements of rates for the reaction of $N(^2P)$ with O_2 and NO , and for quenching by $O(^3P)$ were taken. The experimental procedure and kinetic analysis are identical to those given in the previous section for the $N(^2D)$ measurements.

3.2. Results

3.2.1. $N(^2P) + O_2$ Experiments

A previous measurement² of the rate coefficient for the reaction



made using the FACELIF apparatus, reported a value of $1.8 \times 10^{-12} \text{ cm}^3 \text{ s}^{-1}$. This was somewhat lower than some previously reported values^{3,4}. We therefore undertook a remeasurement of this rate coefficient in which the effects of the finite mixing time were explicitly accounted for. This was done, as reported in the previous section, by performing rate measurements over a range of reaction lengths, under uniform flow conditions. These measurements were carried out under fast flow conditions and the quenching rate for each data set plotted as a function of the flow time. The results are plotted in Fig. 3.1. The slope of this graph yields a value for the rate coefficient of $3.4 \times 10^{-12} \text{ cm}^3 \text{ s}^{-1}$. The x-axis intercept gives a value for the effective mixing time for the particular flow conditions which in this instance is approximately 1.2 ms. Neglect of this effect leads to a considerable underestimation of the rate coefficient. The reported value is in good agreement with previous measurements^{3,4}.

3.2.2. $N(^2P) + NO/O$

As with $N(^2D)$, the variation in the effective rate coefficient (the rate coefficient calculated assuming that all the initially added NO is converted instantaneously to $O(^3P)$) with reaction time was measured over a wide range of flow times. The results are shown in Fig. 3.2. The error bars on each data point represent the statistical errors obtained from a linear regression fit to the individual data sets. The temporal behavior is identical to that observed for $N(^2D)$ (see Fig. 2 in Section 2). The reaction



is known to be rapid⁵. Therefore, as for $N(^2D)$, the short reaction time measurements may be considered to give a lower limit on the rate coefficient for reaction (3.3). It might also be expected that the longer reaction time measurements will give an upper limit to the $N(^2P)+O$ quenching rate coefficient.

In order to derive rate coefficients for $N(^2P)$ reaction with NO and quenching by $O(^3P)$, it is necessary to know the $N(^4S)$ atom concentration. For the NO measurements, $[N(^4S)]$ was determined using a variation of the technique described in the previous section. The equation describing the NO decay along the flowtube is

$$[NO] = [NO]_0 \exp(-k_N[N]t) \quad (3.4)$$

provided that $[NO] \ll [N]$. In this instance, the NO $\gamma(0,0)$ MPI signal was monitored as a function of the injector position. This is equivalent to varying t and therefore a plot of $\ln [\text{MPI-signal}]$ vs. t will have a slope of $k_N[N]$. k_N is known from the literature⁵ and thus $[N]$ is derived for all points along the flowtube. The results are plotted in Fig. 3.3.

The results do not display the linear behavior that might be expected over the whole range. Three distinct regions are apparent. The two shorter reaction time regions ($t < 3.2\text{ms}$) indicate that $[N]$ is different for these two ranges of injector position. $[N]$ measurements made using the technique described in the previous section and direct MPI measurements (next section) confirm that this is the case. The variation in $[N]$ would appear to be the result of a physical effect with the loop injector

disturbing the spatial distribution of the afterglow as it is withdrawn towards the point at which the flowtube diameter increases (see Fig. 1 in Section 2). While the effect appears to have a sharp onset it is probable that there is some variation in $[N]$ over the whole range. The main source of error, however, is expected to be from the error bars associated with the literature value of k_N^5 . The values obtained are, for $t < 2.7$ ms, $[N] = (0.211 \pm 0.055)$ mTorr and, for $3.2 < t < 2.7$ ms, $[N] = (0.411 \pm 0.107)$ mTorr.

As the injector is drawn further back towards the expansion point, the flow is disturbed such that the main and quencher flows do not become fully mixed for some distance beyond the addition point. The net result is that the effective contact time between the reactants remains approximately constant over the whole range. Care must be taken to avoid this region when taking kinetic measurements.

The results of three kinetic runs were computed using the analysis given in the previous section. The effective rate coefficient measurements (Fig. 3.2) suggest that, as for $N(^2D)$, the O-atom contribution to the decay may be neglected for fast flows. The flow conditions used were identical to those used for $N(^2D) + NO$ experiments and therefore the same effective mixing time of (0.48 ± 0.19) ms was used. The data are presented in Figs. 3.4-3.6. The rate coefficients obtained using this procedure are $(4.64 \pm 0.12) \times 10^{-11}$, $(4.52 \pm 0.26) \times 10^{-11}$, and $(4.32 \pm 0.12) \times 10^{-11} \text{ cm}^3 \text{ s}^{-1}$ for $t = 1.78, 1.98$, and 2.16 ms, respectively.

This value for the $N(^2P) + NO$ reaction rate coefficient was then used to calculate a value for the O atom quenching rate coefficient. As for $N(^2D)$, these measurements are best taken at long flowtimes with high $[N]$. The results of four measurements are shown in Figs. 3.7-3.10. These yield rate coefficient values of $(2.45 \pm 0.07) \times 10^{-12}$, $(3.05 \pm 0.13) \times 10^{-12}$, $(2.83 \pm 0.04) \times 10^{-12}$, and $(4.29 \pm 0.14) \times 10^{-12} \text{ cm}^3 \text{ s}^{-1}$, for $t = 38.1, 31.5, 27.7$, and 22.1 ms, respectively. A number of other measurements were also taken. These all exhibited a trend towards lower rate coefficient values as the reaction time increased.

3.3 Discussion

It has recently been reported⁶ that microwave discharges do not provide a clean source of $N(^2P)$. The results reported by Piper exhibit a rapid initial decay followed by a considerably slower decay for larger quencher additions. This was interpreted as the initial rapid quenching of some unidentified precursor to $N(^2P)$, followed by quenching of the remaining microwave generated $N(^2P)$. It was suggested that this second region represented the true $N(^2P)$ rates.

The longer reaction time measurements showed indications of non-exponential behavior in some instances (see Figs. 3.7 - 3.10). Also, the recovered rate coefficients decreased with increased reaction time even after correction for the NO contribution. The range of values indicated by these results is considerably lower than previously reported O-atom quenching rate coefficients, which range from 1×10^{-11} to $7 \times 10^{-11} \text{ cm}^3 \text{ s}^{-1}$ ^{7,8}. These results clearly indicate that, for these time scales, we are not observing a pure exponential decay of discharge generated $N(^2P)$.

3.4. Conclusions

It is not possible to infer anything regarding the $N(^2P) + O$ quenching rate coefficient from these results. The variation in the effective rate coefficient (Fig. 3.2) with time is clearly misleading. The $N(^2P) + NO$ results were therefore recalculated using the most recently reported value⁶ for the $N(^2P) + O$ quenching rate coefficient of $1.7 \times 10^{-11} \text{ cm}^3 \text{ s}^{-1}$. The data appear to give reasonable exponential decays and consistent rate coefficient values. Given the short reaction time and low $[N(^4S)]$, the O-atom correction is still comparatively minor. This is illustrated graphically in Fig. 3.11 where the magnitude of the correction is on the order of 5%. The recalculated values are $(4.38 \pm 0.12) \times 10^{-11}$, $(4.24 \pm 0.25) \times 10^{-11}$ and $(4.00 \pm 0.12) \times 10^{-11} \text{ cm}^3 \text{ s}^{-1}$ for $t = 1.78, 1.98$, and 2.16 ms, respectively, giving a mean value of $(4.21 \pm 0.17) \times 10^{-11} \text{ cm}^3 \text{ s}^{-1}$. The quoted limits here only include errors from the fitted slopes and take no account of uncertainties in $[N]$ or the mixing time. This value is approximately 25% higher than previously reported values^{3,9}. Given the limited dynamic range of these experiments, it is not possible to comment on the suggestion⁶ that this

measurement in fact reflects the reaction rate of NO or O₂ with an unidentified N(²P) precursor.

Using the new FACELIF configuration (see Section 7), incorporating a movable MPI detector, it should be possible to observe the N(²P) decay along the flowtube. Any deviation from the predicted exponential time decay (governed by wall diffusion) will indicate the presence of N(²P) precursors⁶ or a possible N atom recombination source².

References

1. C.E. Moore, *Atomic Energy Levels*; NSRDS-NBS35, Vol. I; U.S. Government Printing Office: Washington, DC, 1971.
2. C.M. Phillips, J.I. Steinfeld and S.M. Miller, *J. Phys. Chem.* **91**, 5001 (1987).
3. D. Husain, S.K. Mitra and A.N. Young, *J. Chem. Soc., Faraday Trans. 2*, **70**, 1721 (1987).
4. M.P. Iannuzzi and F. Kaufman, *J. Chem. Phys.*, **73**, 4701 (1980).
5. J.H. Lee, J.V. Michael, W.A. Payne and C.J. Steif, *J. Chem. Phys.* **69**, 3069 (1978).
6. W.T. Rawlins, L.G. Piper, M.E. Fraser, H.C. Murphy, T.R. Tucker and A. Gelb, Report No. AFGL-TR-89-0124 (Physical Sciences Inc., Wakefield, Mass., 1989). Vol. I - ADA213341; Vol. II - ADA213342; Vol. III - ADA213343; Vol. IV - 213344.
7. R.A. Young and O.J. Dunn, *J. Chem. Phys.* **63**, 1150 (1975).
8. M.F. Golde and B.A. Thrush, *Faraday Discuss. Chem. Soc.* **53**, 233 (1972).
9. D. Husain, L.J. Kirsch and J.R. Wiesenfeld, *Faraday Discuss. Chem. Soc.* **53**, 201 (1972).

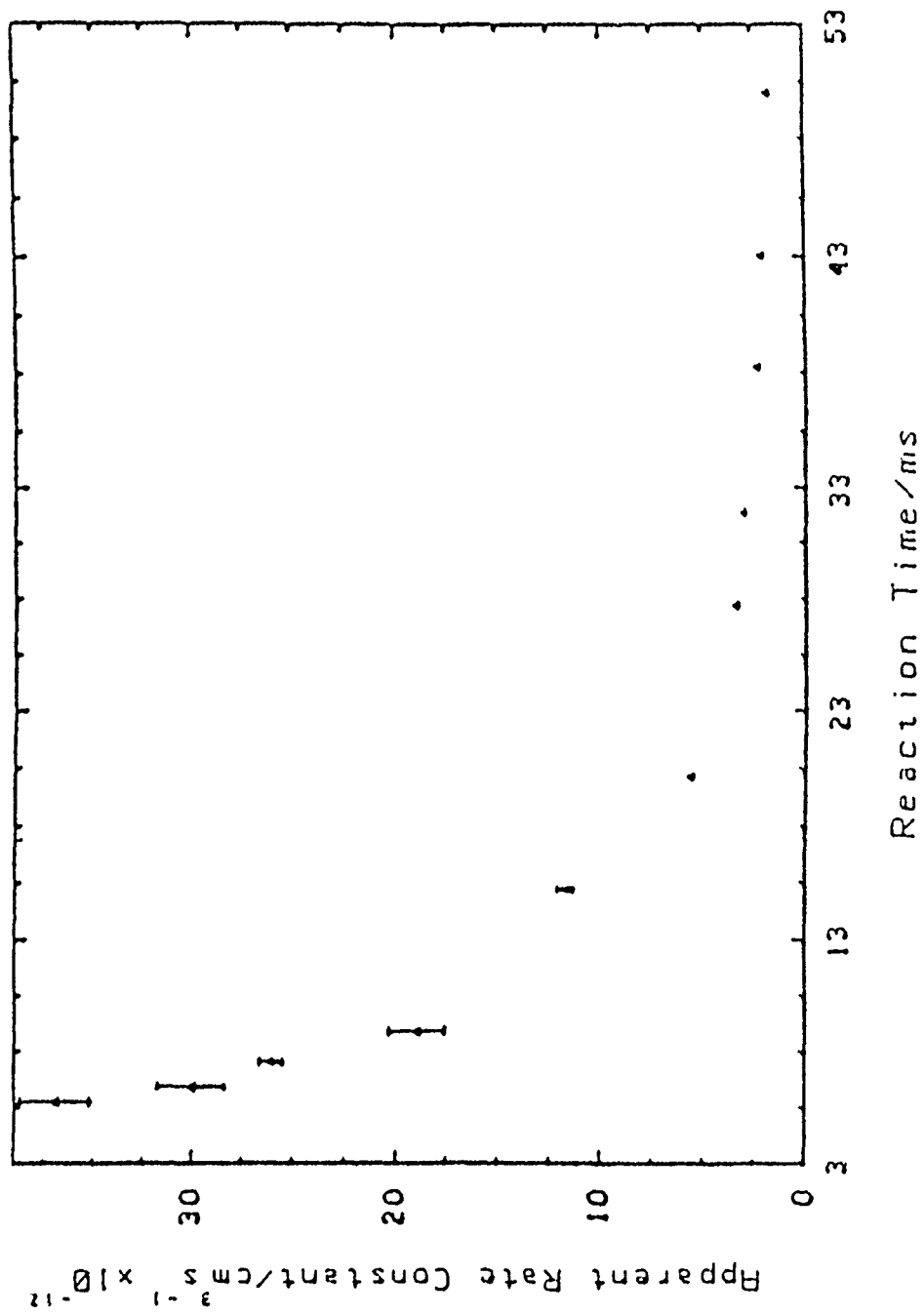


Figure 3.1. Variation in the effective rate coefficient, k_{eff} (Eq. 2.5) with reaction time for $\text{N}(^2\text{P})$.

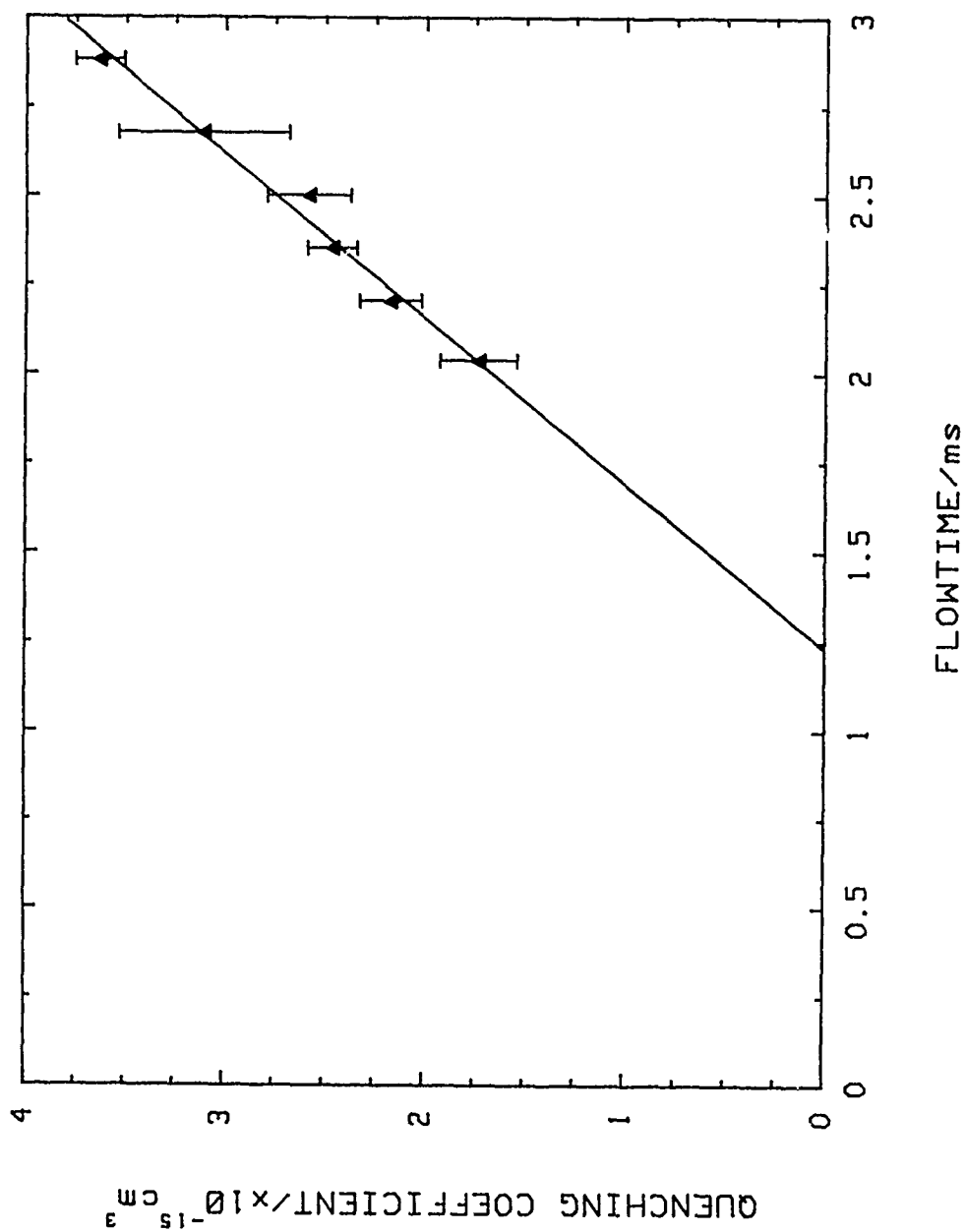


Figure 3.2. Variation in the quenching coefficient $(-d \ln[N(^2P)]/d[O_2])$ with flowtime. Flowtube pressure = 0.39 Torr, flow velocity = 7400 cm s⁻¹.

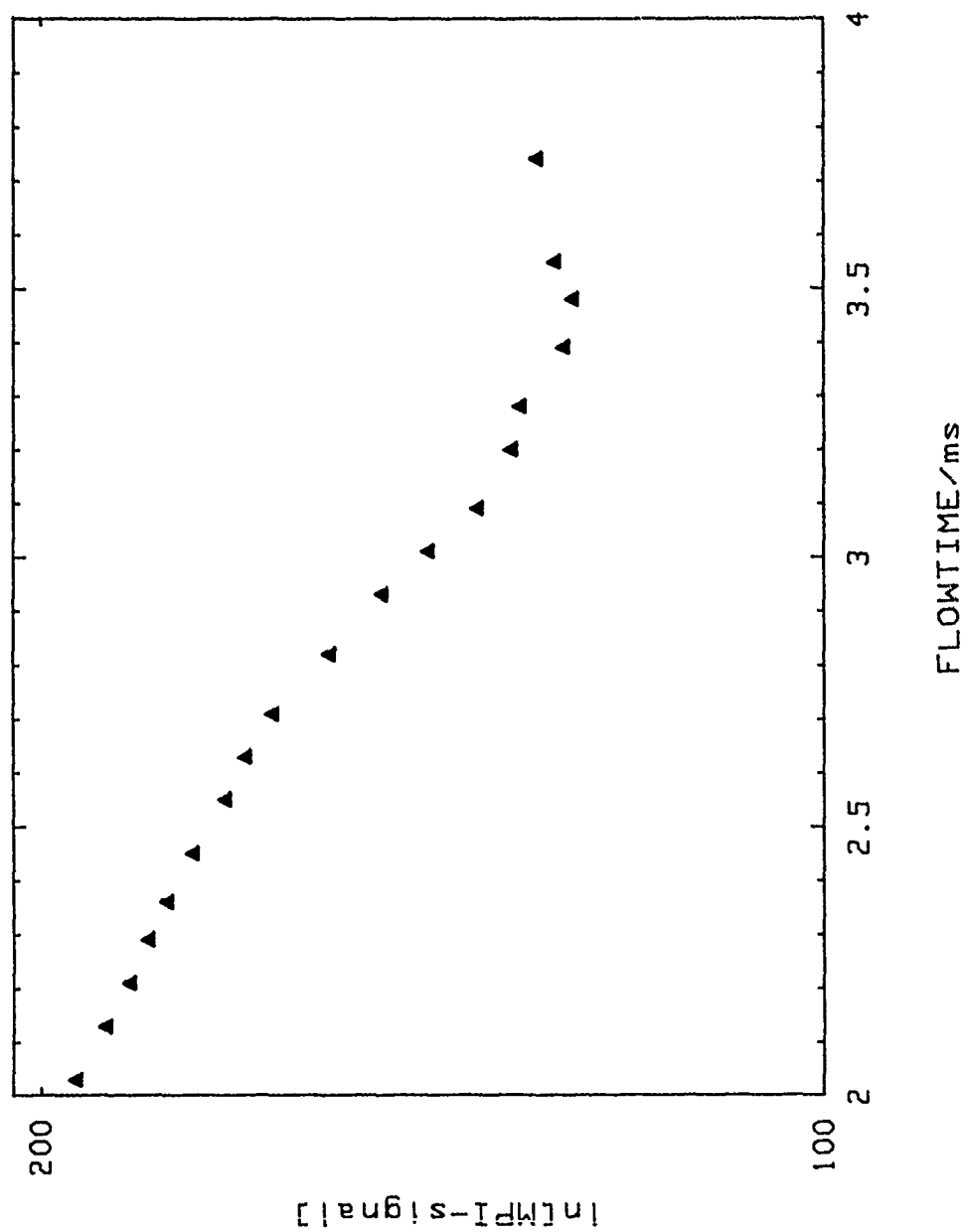


Figure 3.3. Variation in [NO] with injector position (= flowtime). Flowtube pressure = 0.38 Torr, flow velocity = 7400 cm s^{-1} and $[\text{NO}]_0 = 0.025 \text{ mT}$.

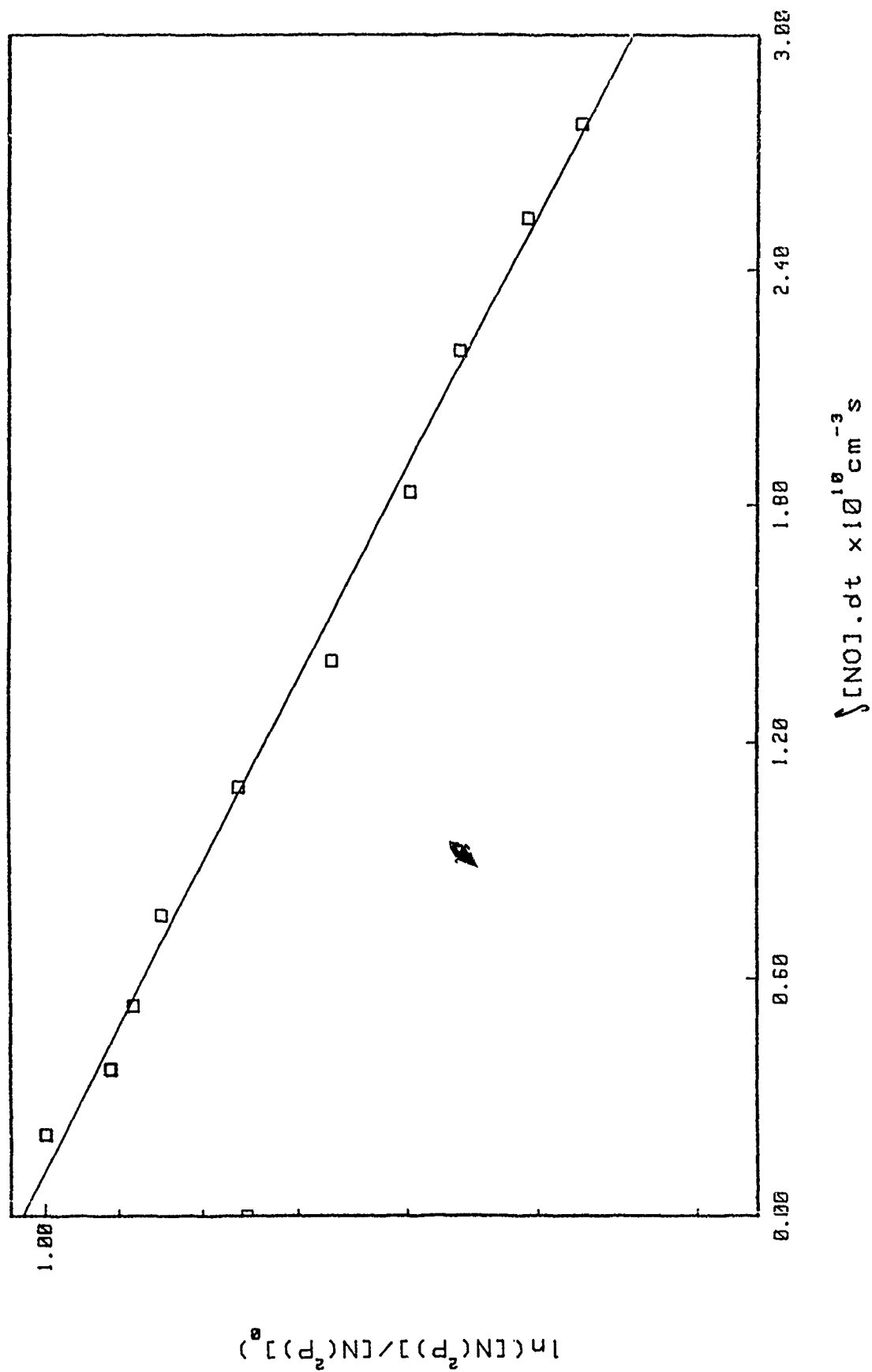


Figure 3.4. Decay of the $N(^2P)$ MPI-signal as a function of $\int [NO].dt$. $t = 1.78 \text{ ms}$, $[N] = 0.211 \text{ mT}$ and $k_{NO} = (4.64 \pm 0.12) \times 10^{-11} \text{ cm}^3 \text{ s}^{-1}$.

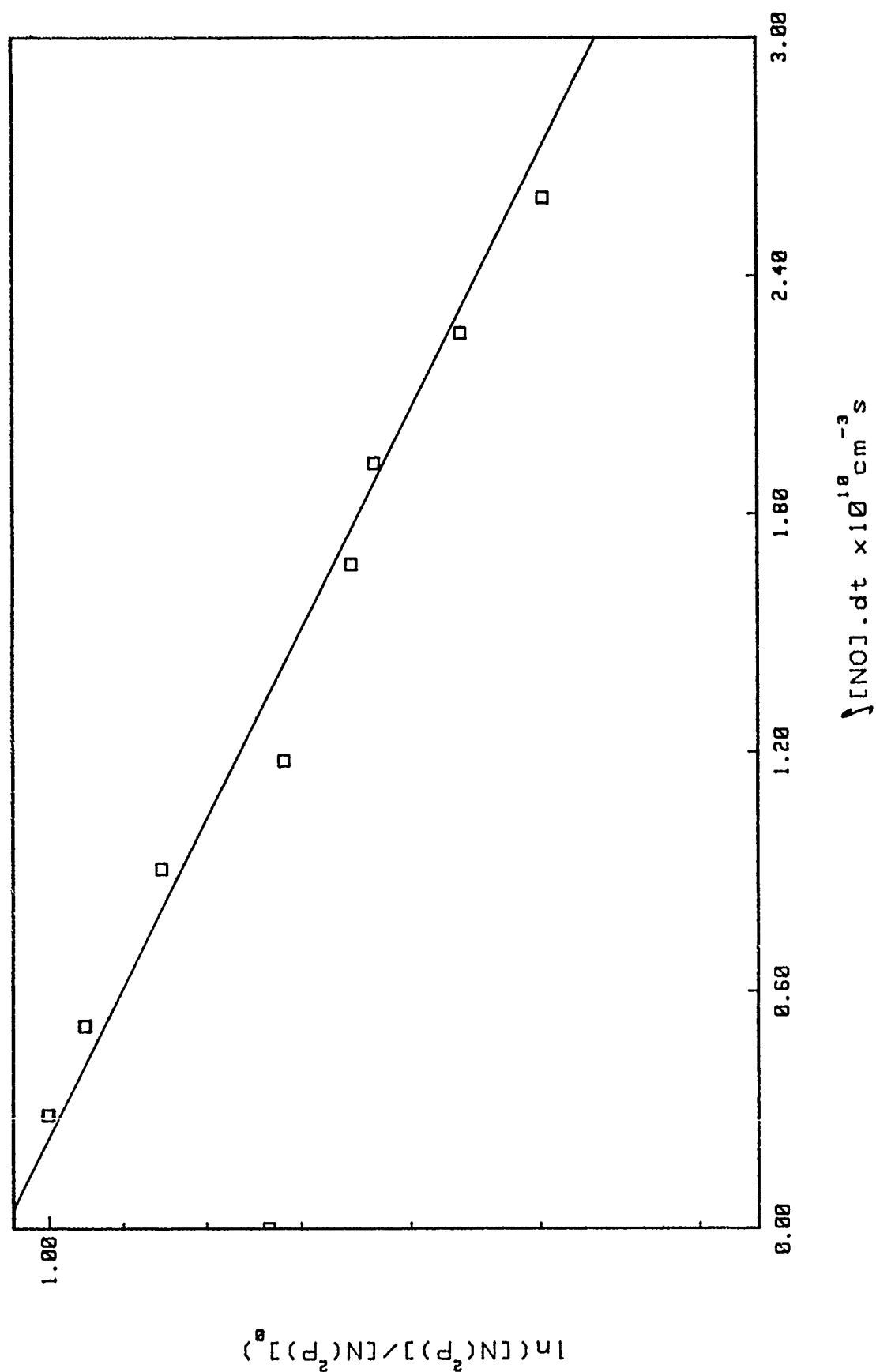


Figure 3.5. As Fig. 3.4 with $t = 1.98 \text{ ms}$, $[N] = 0.211 \text{ mT}$ and $k_{\text{NO}} = (4.52 \pm 0.26) \times 10^{-11} \text{ cm}^3 \text{ s}^{-1}$.

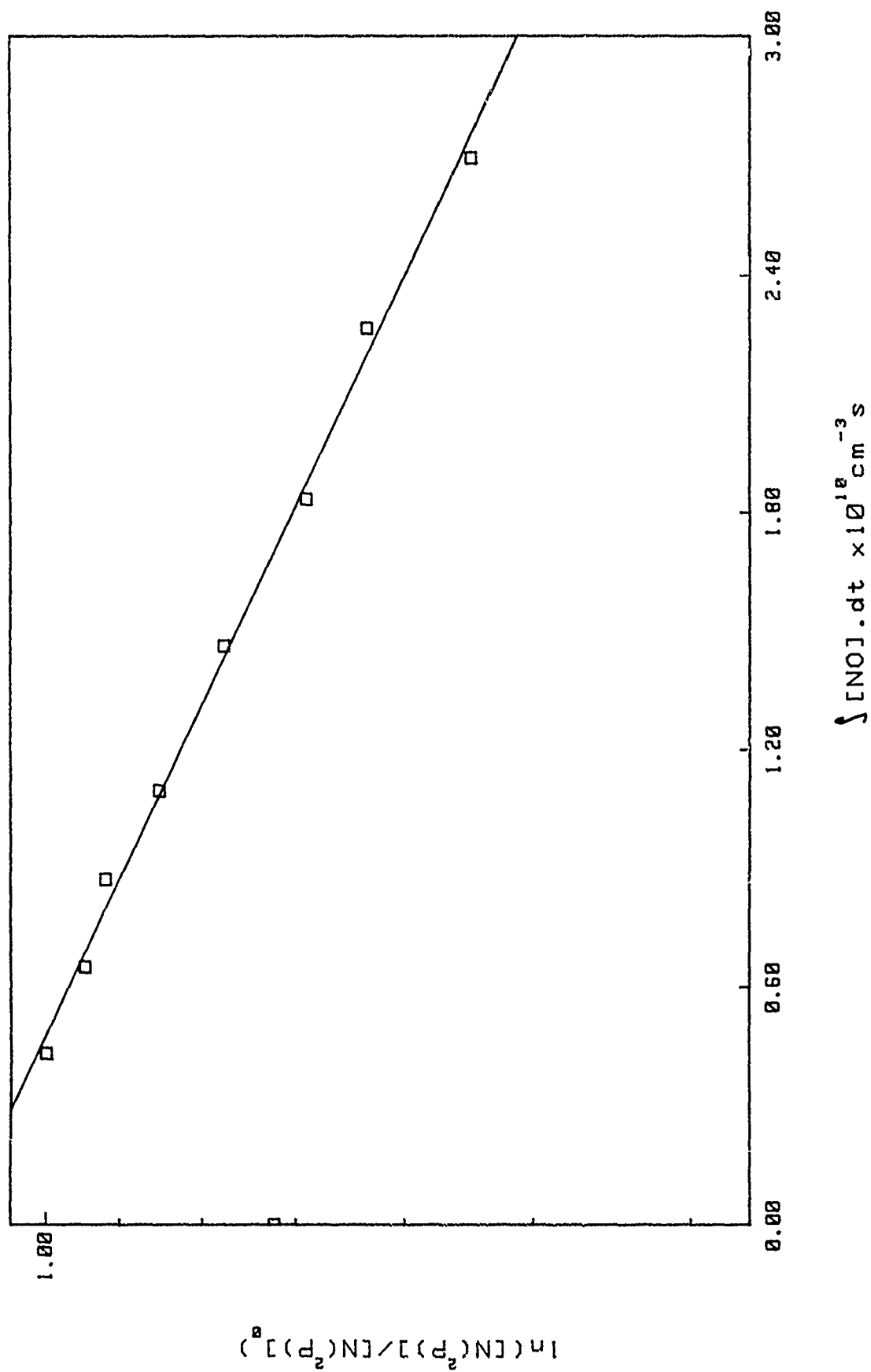


Figure 3.6. As Fig. 3.4 with $t = 2.16 \text{ ms}$, $[N] = 0.211 \text{ mT}$ and $k_{\text{NO}} = (4.32 \pm 0.16) \times 10^{-11} \text{ cm}^3 \text{ s}^{-1}$.

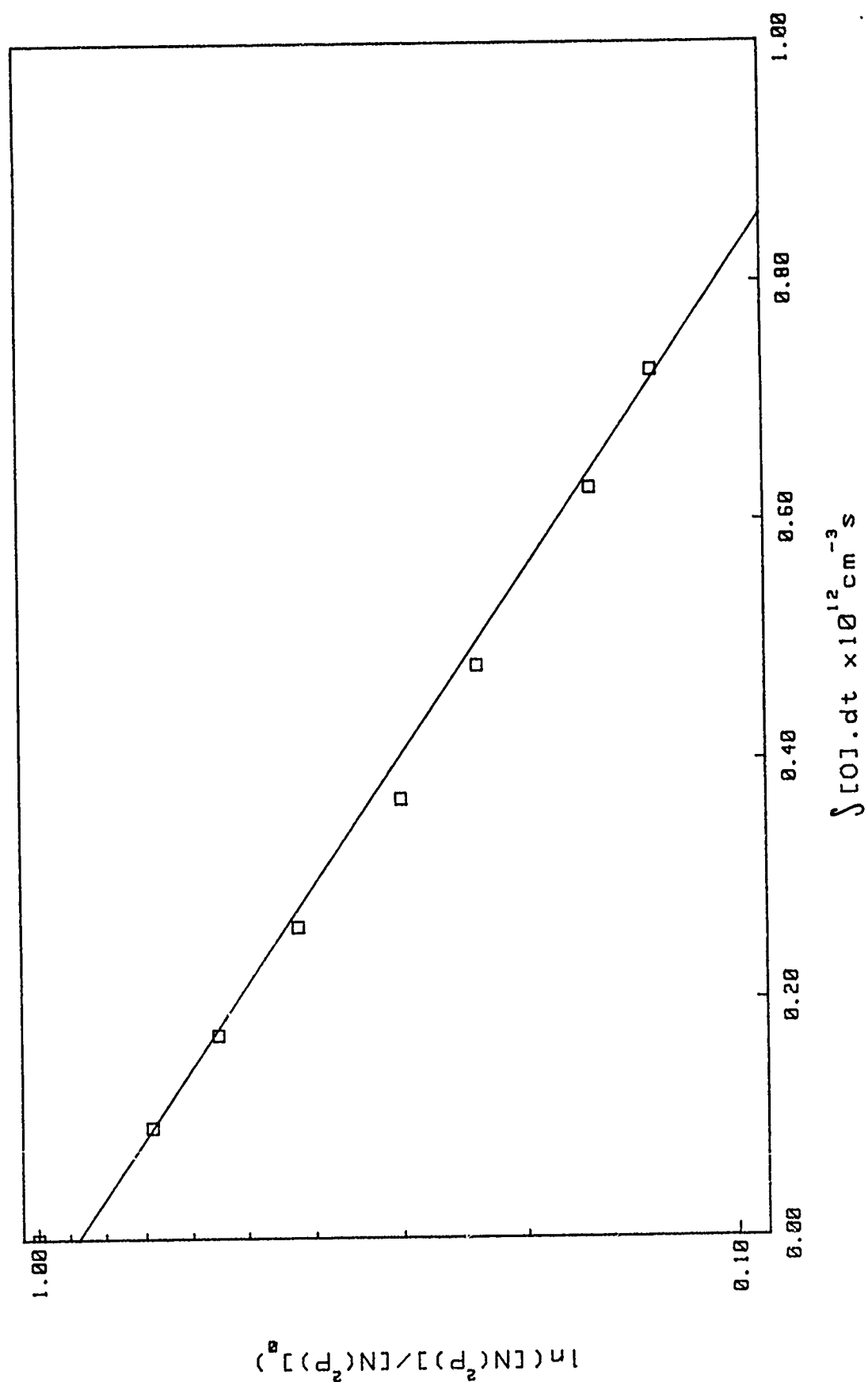


Figure 3.7. Decay of the $N(^2P)$ MPI-signal as a function of $\int [O] dt$. Flowtube pressure = 4.1 Torr, $[N] = 2.39 \text{ mT}$, $t = 22.1 \text{ ms}$ and $k_O = (4.29 \pm 0.14) \times 10^{-12} \text{ cm}^3 \text{ s}^{-1}$.

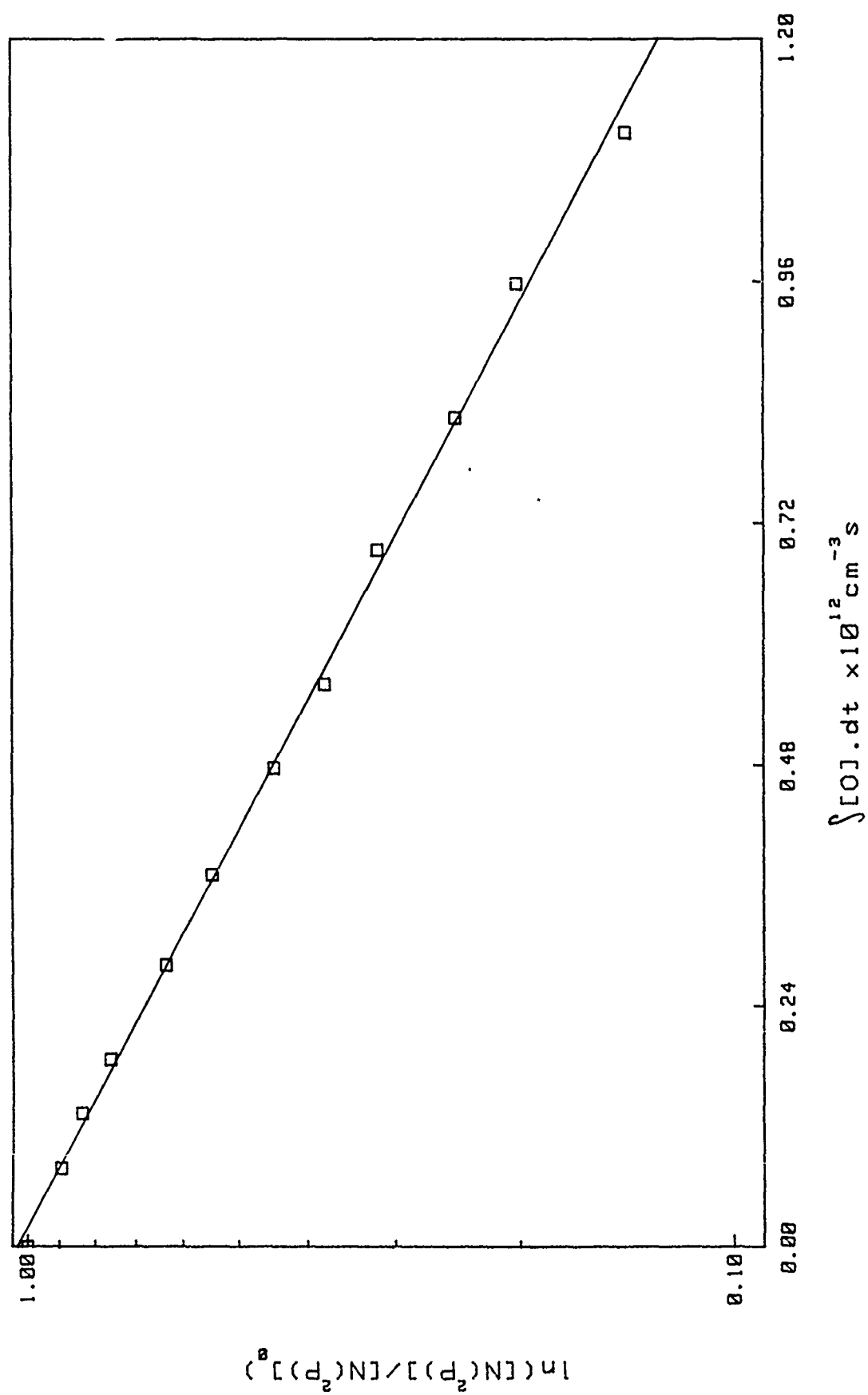


Figure 3.8. As Fig. 3.7 with flowtube pressure = 3.0 Torr, $[N] = 3.06 \text{ mT}$, $t = 27.7 \text{ ms}$ and $k_O = (2.83 \pm 0.04) \times 10^{-12} \text{ cm}^3 \text{ s}^{-1}$.

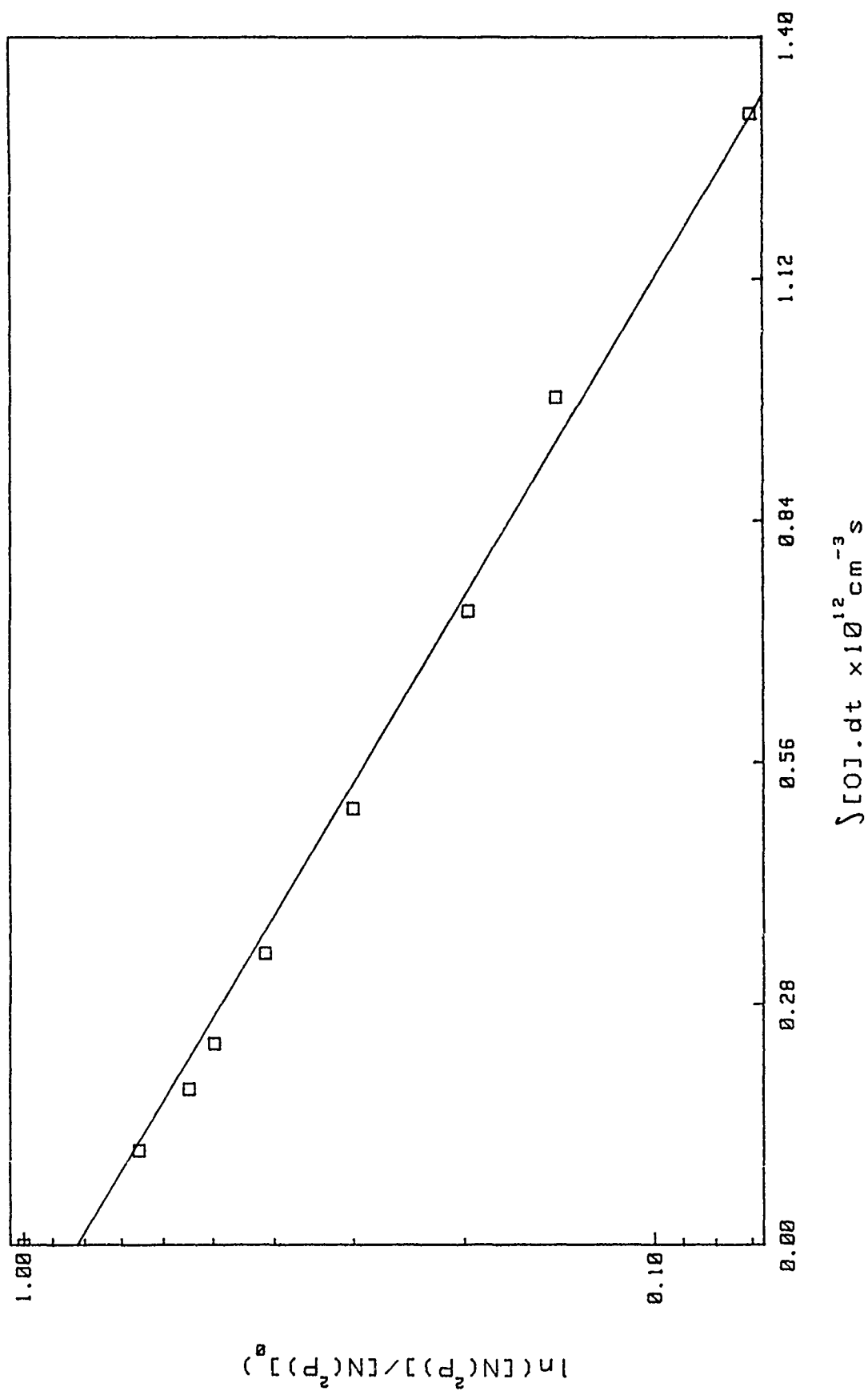


Figure 3.9. As Fig. 3.7 with $[N] = 2.87 \text{ mT}$, $t = 31.5 \text{ ms}$ and $k_O = (3.05 \pm 0.13) \times 10^{-12} \text{ cm}^3 \text{ s}^{-1}$.

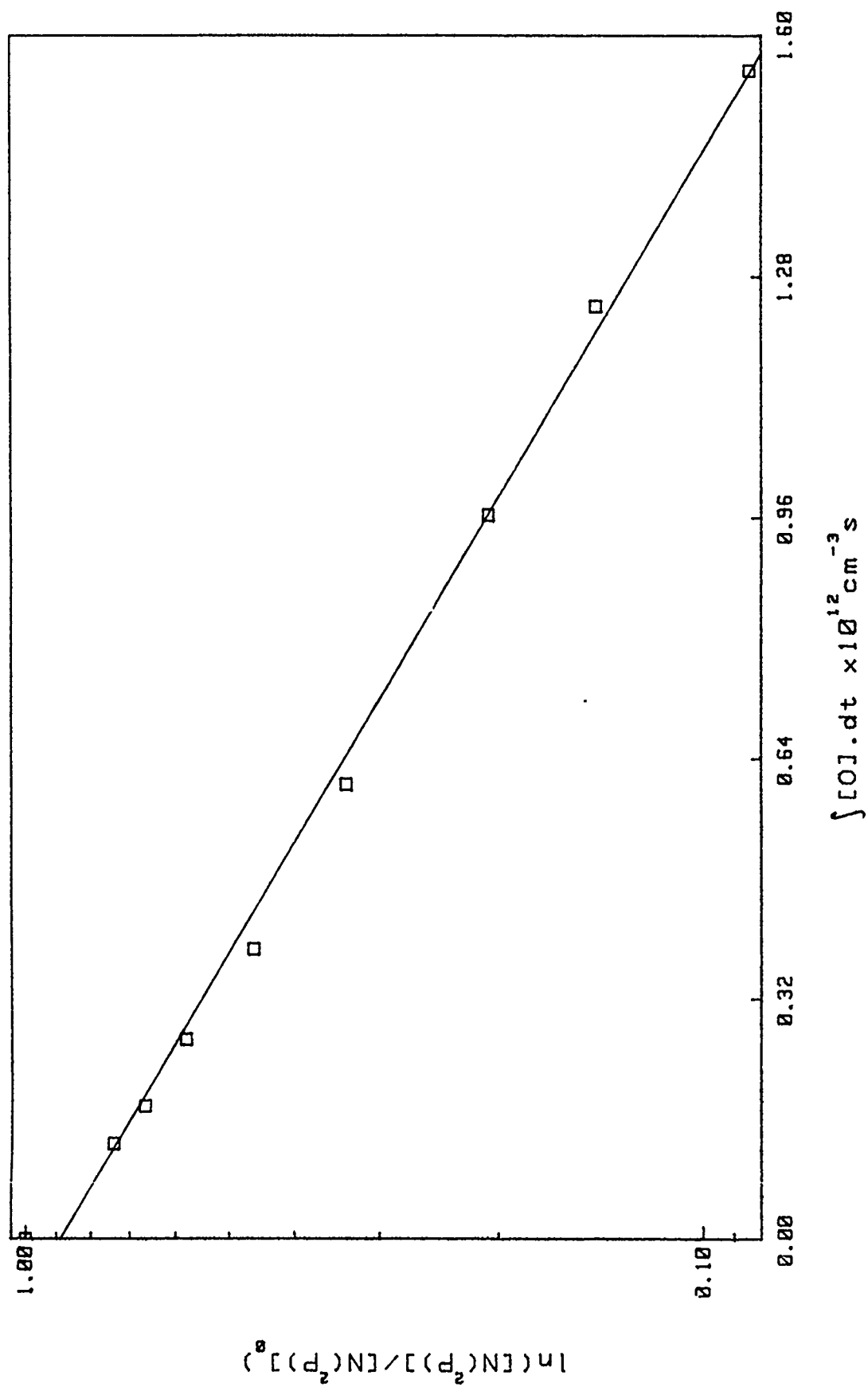


Figure 3.10. As Fig. 3.7 with $[N] = 3.54 \text{ mT}$, $t = 38.1 \text{ ms}$ and $k_O = (2.45 \pm 0.07) \times 10^{-12} \text{ cm}^3 \text{ s}^{-1}$.

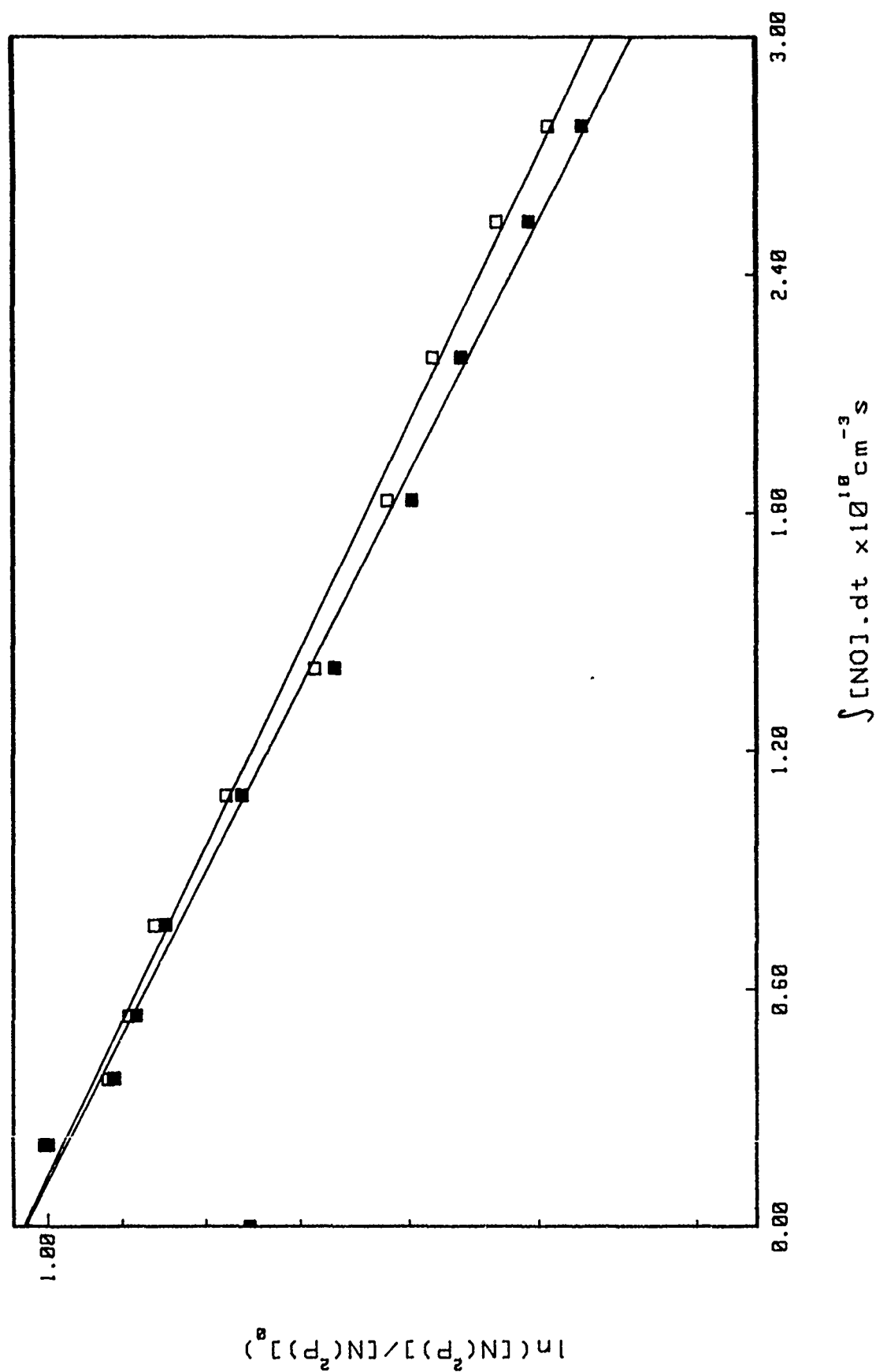


Figure 3.11. Comparison of decay of $N(^2P)$ MPI-signal with (light) and without (shaded) allowance for O-atom quenching. Upper trace gives $k_O = 4.38 \times 10^{-11} \text{ cm}^3 \text{ s}^{-1}$, lower trace $4.64 \times 10^{-11} \text{ cm}^3 \text{ s}^{-1}$.

4. RESEARCH NOTE [Spectrochimica Acta, v. 46A, 1990]

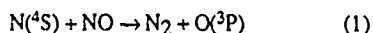
DETECTION OF $N(^4S)$ BY RESONANTLY ENHANCED MULTIPHOTON IONIZATION SPECTROSCOPY

(Received 1 December 1989)

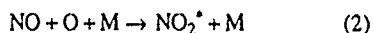
Abstract - We report the first instance of detection of $N(^4S)$ atoms by Resonantly Enhanced Multiphoton Ionization (REMPI). The magnitude of the ion signal, after correction for laser power dependence, is directly proportional to the $N(^4S)$ concentration and, once calibrated, is a direct and highly sensitive method for $N(^4S)$ concentration measurements in fast-flow kinetics experiments.

INTRODUCTION

In experiments utilizing active nitrogen flows, it is generally necessary to know the ground state nitrogen atom concentration. This value is usually determined using a standard NO titration technique [1]. This method makes use of the reactions

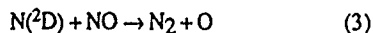


and

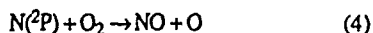


Reaction (1) is rapid [2] and serves to deplete $[N(^4S)]$ stoichiometrically. Monitoring the N_2 first positive emission around 580nm gives a fluorescence signal proportional to $[N(^4S)]^2$ for $[NO] < [N(^4S)]$. Beyond the end point NO_2^* emission following reaction (2) gives a signal proportional to NO in the same spectral range. This technique works well provided that reaction (1) has sufficient time to go to completion and $N(^4S)$ is present in sufficient quantity. If this is not the case then both the N_2 first positive and NO_2^* emission will contribute to the signal level.

Many reactions involving metastable atoms and molecules require fast flow conditions due to the rapid decay of the metastable concentration. The reactions



and



are examples of this [3-5]. In order to calculate the rate coefficient of reaction (3), $[N(^4S)]$ must be known in order to determine the rate of depletion of NO via reaction (1). Under certain conditions, the flow time and $N(^4S)$ concentration may be such that reaction (1) does not go to completion and the standard NO titration technique will no longer give accurate values for $[N(^4S)]$. The use of Resonantly Enhanced Multiphoton Ionization (REMPI) to measure relative $N(^2D)$ and $N(^2P)$ concentrations is well established [5,6]. Here we report, to our knowledge, the first instance of REMPI detection

of $N(^4S)$ atoms. The magnitude of the ion signal is directly proportional to the $N(^4S)$ concentration and, once calibrated, may be used to measure $N(^4S)$ absolutely.

EXPERIMENTAL

These investigations were carried out using the FACELIF afterglow reactor which has been described in detail elsewhere [4,7]. A schematic of the experimental apparatus is shown in Fig. 1. The $N(^4S)$ atoms are generated in a flow of 1-2% N_2 in He, using a microwave discharge. The current created by the photoions, across a pair of Ni wire grids, biased at 90V, is amplified using an Ithaco model 1211 current amplifier and detected on an EG & G model 162 Boxcar Averager. The laser power is also monitored using a Molelectron Pyroelectric joulemeter (J3-09). The fluorescence measurements are made using a photomultiplier tube through a 580 ± 5 nm filter. The NO used for these titrations is a 5% mixture of NO in He and is added through a loop injector upstream of the detection region. Typical flow times were 25-30ms with total tube pressures of 2.5-3.5 Torr. These slow flow/high pressure conditions are best suited to making NO titration measurements of $[N(^4S)]$ giving comparatively intense signals and allowing reaction (1) ample time to go to completion. The $N(^4S)$ concentration could be varied either by adjusting the N_2 to He ratio (this was typically 1-3% N_2 in He) or more conveniently by altering the microwave power.

The transition $N(2p^2 3p^4 D_j^0) \leftarrow N(2p^3 4s_{3/2}^0)$ may be resonantly excited by two 211 nm photons [8], and the atom then ionized by a third photon of the same energy. Laser radiation at 211 nm may be generated by stimulated Raman frequency shifting of the doubled output of a Nd:YAG pumped dye laser [9] but this generally gives pulse energies of less than 100 mJ. Significantly higher pulse energies are desirable for REMPI detection. Here we have used a BBO crystal to double the output from a Nd:YAG pumped dye laser (Quanta-Ray DGR2A, PDL-1, INRAD Autotracker II) directly. Stilbene 420 laser dye gave pulse energies of approximately 0.5 mJ, measured after exiting the flow tube.

This power level decreased rapidly in time with the dye having a useful lifetime of about 20 minutes. The decrease proved advantageous when taking measurements of the power dependence of the ion signals, enabling a large number of data points to be taken without the extensive use of neutral density filters to attenuate the beam. When making quantitative measurements of $[N(^4S)]$, however, it is desirable to keep the laser power as constant as possible to minimize corrections necessary for power normalization of ion signals. We found that the use of ~ four times larger dye reservoirs greatly enhanced the useful life of the dye and also minimized power variations during the course of data acquisition.

ABSOLUTE $[N(^4S)]$ MEASUREMENTS

The $N(^4D_0)$ state is split into four levels, $J=1/2, 3/2, 5/2$, and $7/2$, at 94770.85, 94793.46, 94830.86, and 94881.79 cm^{-1} , respectively. The relative intensities are simply given by the upper state degeneracy $(2J+1)$ and the observed spectrum will be a quartet with intensity ratios of 1:2:3:4 ($J=1/2:3/2:5/2:7/2$). The observed spectrum is shown in Fig. 2. The most intense line was used throughout for all quantitative measurements of $[N(^4S)]$. To normalize the signal levels accurately for variations in laser power, it was necessary to characterize the power dependence of the ion signal precisely prior to any data acquisition. The ion signal is proportional to some power N of the laser intensity I , and therefore a plot of \ln (ion signal) vs. $\ln I$ will have a slope equal to N . The results of doing this are shown in Fig. 3. The slope varies between 2.8 and 1.5 going from low to higher power. This indicates that the two photon transition is becoming saturated at the higher powers. A similar power dependence was observed for $(2+1)$ photon ionization of $N(^2D)$ at 269nm [10], although somewhat different conclusions were drawn in that work regarding the relative saturation of the excitation and ionization steps. The two photon excitation cross-section for this transition has been calculated [9] and therefore the transition rate may be calculated. The fit of the data in Fig. 3 is obtained using a simple rate equation model for a three level system [11]. Strictly speaking, correct normalization of signals for power variations requires that signal and laser power be recorded for each pulse [12]. Here we have recorded the average ion signal and laser power over a large number of pulses with the beam tightly focused between the detector grids. The resulting ion signal therefore consists of contributions over a range of saturation conditions. It is thus inappropriate to comment on the magnitudes of the experimentally observed rates for either the ionization or the two photon excitation. For the purposes of this study it is only necessary to be able to understand the bulk behavior of the system. Fig. 3 indicates that for small variations in average laser power ($\pm 5\%$) it is a reasonable approximation to use the

same laser power dependence factor when normalizing the ion signals.

For conditions where reaction (1) has time to go to completion, $[N(^4S)]$ may be determined by observing the reduction in the ion signal as NO is added. The x-axis intercept on a plot of the ion signal vs. $[NO]$ gives the value of $[N(^4S)]$. The slope of this line serves to calibrate the ion signal level in terms of absolute $[N(^4S)]$ concentrations. In order to verify the accuracy of this technique for $[N(^4S)]$ measurement, comparative measurements were taken using REMPI and the standard fluorescence monitoring titration technique [1]. The results are listed in Table 1. The REMPI results are the x-axis intercept of a weighted linear regression fit of NO titration data sets with $\pm 2\sigma$ error limits. The standard titration measurements may be considered accurate to $\pm 5\%$. The results are in good agreement indicating that the REMPI technique yields accurate values for $[N(^4S)]$.

DISCUSSION

REMPI provides a sensitive method for quantitatively detecting ground state nitrogen atoms. Number densities on the order of 10^{10} atoms cm^{-3} were easily detected compared to a limit, for our flow system, of around 2×10^{13} atoms cm^{-3} using the more usual titration technique. Below this level the fluorescence measurements encountered problems in the form of stray light from the discharge reaching the detector. A more serious problem can arise from fluorescence due to sources other than $N(^4S)$ atom recombination, which contributes significantly to the signal intensity [4,13]. Unlike the standard technique, REMPI offers a state specific method of monitoring $[N(^4S)]$ directly and is therefore less susceptible to extraneous signals. The signal level may be calibrated under slow flow/high $[N(^4S)]$ conditions. The magnitude of the ion signal may then be used to give a direct measurement of $[N(^4S)]$ for experiments requiring fast flows where $[N(^4S)]$ may be low; these conditions are inappropriate for standard titration measurements.

Acknowledgments: This research was performed under contract F19628-86-C-0139 from the Air Force Geophysics Laboratory, and sponsored by the Air Force Office of Scientific Research under Task 2310G4.

Department of Chemistry, C.P. FELL
Massachusetts Institute of Technology, JI STEINFELD
Cambridge, Massachusetts 02139, U.S.A.

Air Force Geophysics Laboratory, S.M. MILLER
Hanscom Air Force Base
Bedford, Massachusetts 01731, U.S.A.

REFERENCES

- [1] F. Kaufman and J.R. Kelson, *7th International Symposium on Combustion* (Oxford University, Oxford, 1958), p 53.
- [2] J.H. Lee, J.V. Michael, W.A. Payne and L.J. Steif, *J. Chem. Phys.* 69, 3069 (1978).
- [3] C.-L. Lin and F. Kaufman, *J. Chem. Phys.* 55, 3760 (1971).
- [4] C.P. Fell, J.I. Steinfeld, and S.M. Miller, *J. Chem. Phys.*, in press.
- [5] C.M. Phillips, J.I. Steinfeld and S.M. Miller, *J. Phys. Chem.* 91, 500 (1987).
- [5] G. Black and L.E. Jusinski, *Chem. Phys. Lett.* 139, 41 (1987).
- [7] I.C. Winkler, R.A. Stachnik, J.I. Steinfeld and S.M. Miller, *J. Chem. Phys.* 85, 890 (1986).
- [8] C.E. Moore, *Atomic Energy Levels*; NSRDS-NBS35, Vol. 1; U.S. Government Printing Office: Washington, D.C., (1971).
- [9] W.K. Bischel, B.E. Perry and D.R. Crosley, *Appl. Opt.* 21, 1419 (1982).
- [10] L.E. Jusinski, G.E. Gadd, G. Black and T.G. Slanger, *J. Chem. Phys.* 90, 4282 (1989).
- [11] J.I. Steinfeld, J. Klaassen, and C.P. Fell (to be published).
- [12] C. Jacobs, R.J. Madix and R.N. Zare, *J. Chem. Phys.*, 85, 5469 (1986).
- [13] L.G. Piper, Report No. PSI-050-TR-509 (Physical Sciences Inc., Wakefield, Mass., 1985).

Table 1. Comparison of $[N(^4S)]$ titrations by NO using standard chemiluminescence detection and direct MPI detection under flow conditions. $[N(^4S)]$ given in mTorr.

| Standard NO Titration | MPI-Titration |
|-----------------------|-----------------|
| 4.38 | 4.48 ± 0.18 |
| 3.28 | 3.40 ± 0.10 |
| 2.65 | 2.50 ± 0.14 |
| 2.02 | 1.96 ± 0.12 |
| 1.97 | 1.97 ± 0.12 |
| 1.42 | 1.51 ± 0.07 |

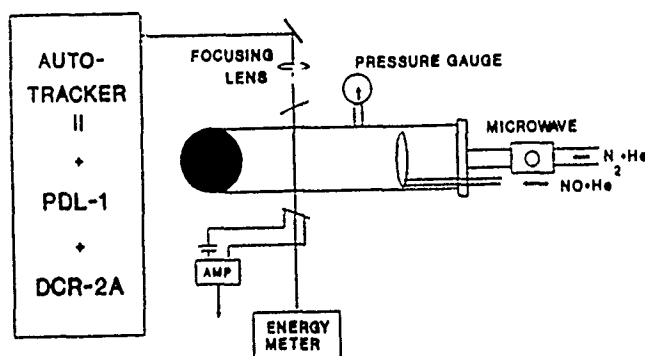


FIG. 1. Schematic of FACELIF experimental apparatus. The solid circle represents a right angle connection to the pumping system.

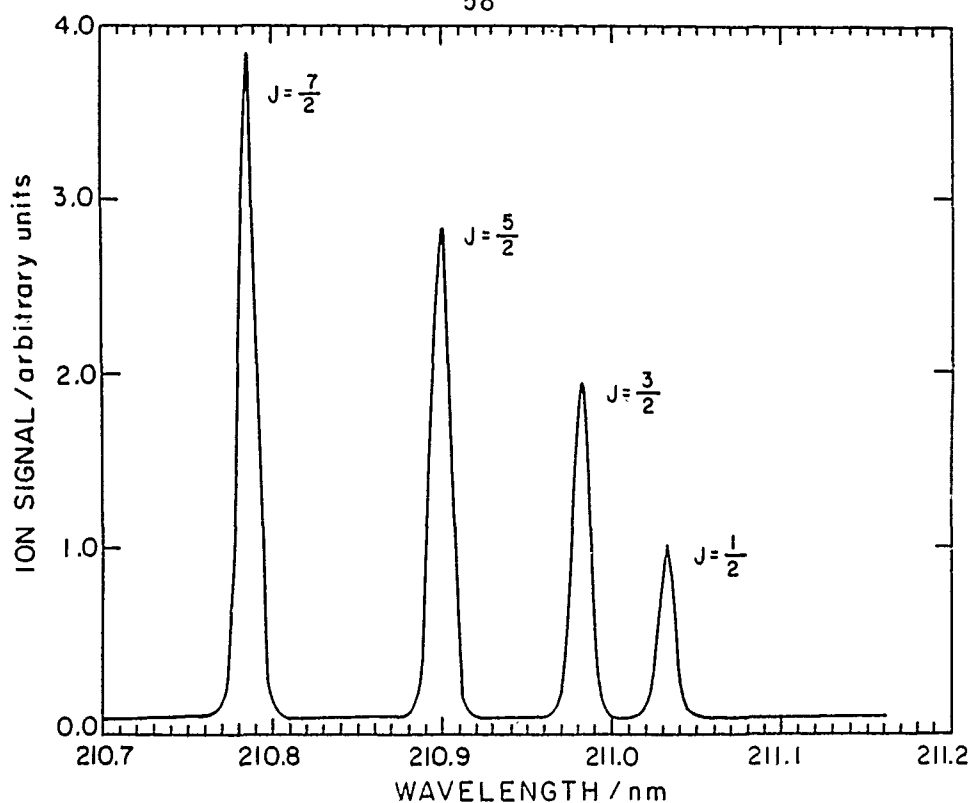


FIG. 2. Three photon (two to resonance) ionization spectrum of $N(^4S)$.

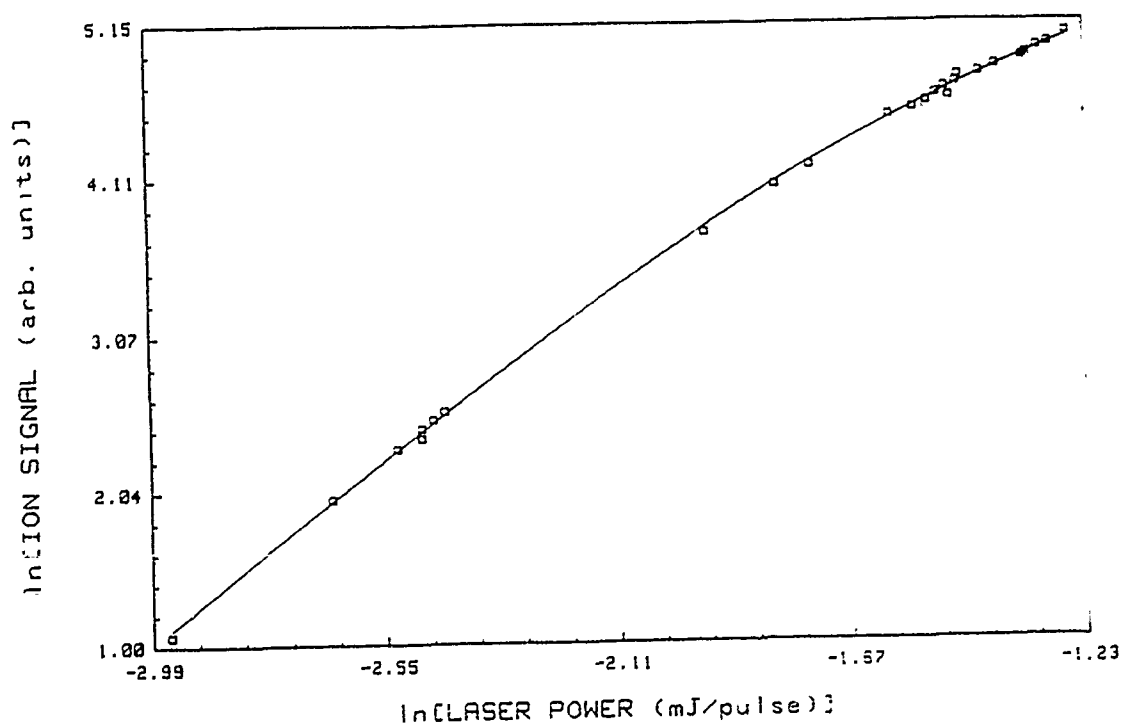


FIG. 3. Power dependence of $N(^4S)$ ionization signal.

5. A Kinetic Model for Resonantly Enhanced Multiphoton Ionization of NO

I. INTRODUCTION

Multiphoton ionization (MPI) is one of the most sensitive techniques for state specific detection of gas phase molecules. For accurate treatment of the population distributions measured by MPI, the dependence of the ion signal on laser intensity and the state specific transition must be known. The dynamics of MPI are complicated. Formal density matrix treatment and inclusion of all the nonlinear processes would be cumbersome, to say the least. Fortunately, for most experimental conditions, a more intuitive rate equation approach may be taken.¹⁻⁷ Such is the case for (1+1) MPI of NO.

The availability of tunable u.v. lasers at 226 nm and the low ionization potential of NO make the NO γ -band $^2\Sigma^+ \leftarrow ^2\Pi$ an ideal system for (1+1) MPI spectroscopy.^{6-12,14} From a rate equation model of MPI, a two photon process would depend quadratically on the intensity of radiation. But, for a sufficiently intense source, the ground to intermediate state resonance will saturate, ionization will be the rate limiting step, and the dependence will be linear.¹¹ Because of this linearity, many investigators try to work in this regime. Shot to shot variations in laser intensity may be corrected by averaging the laser power via boxcar. But this linear region is really a transition between quadratic and zeroth order behavior (see Section III and ref. 2). The laser power necessary for first order dependence will vary for different vibrational subbands and will even vary among rotational transitions.¹⁴

Zare and Jacobs¹³⁻¹⁴ have proposed an excellent method for empirically fitting the ion signal to integrated laser intensity. Their "isopower" spectra are correctly adjusted for variations in laser intensity. But the relationship between populations of different vibrational bands is still ambiguous. In this paper, we will show a simple kinetic model based on the spectroscopic parameters for NO that predicts the form of isopower spectra.

The model is used to relate ion signals from different vibrational subbands to a common scale. We will use these results to discuss the correction of the state specific kinetics for the $N(^4S) + O_2 \rightarrow NO(v=0-7)$ reaction measured via MPI.¹²

2. METHODOLOGY

2.1. THE KINETIC MODEL

To simulate (1+1) MPI spectra, it is necessary to define the frequency at which transitions occur and the magnitude of the ion signal. The resonant ground to intermediate state energy separation is the frequency of the transition. In the case of NO $A^2\Sigma^+ \leftarrow X^2\Pi$ these frequencies may be determined using the equations given by Herzberg²⁰ and the molecular constants for NO.¹⁸ Of more interest here is the magnitude of the ion signal and its dependence on laser power. The ion signal is proportional to the number of ions produced during a laser pulse. The kinetic model assumes a tunable, pulsed laser produces radiation of intensity I ($mW/cm^2 s^{-1}$) and pulse duration Δt having a rectangular temporal width. When the laser is tuned to a specific ro-vibrational transition, the processes of induced absorption, stimulated emission, and ionization will proceed for the duration of the pulse.

By solving the kinetic equations appropriate to the transition in resonance, the fraction of the NO number density converted to ions is determined. The product of this parameter and the Boltzmann factor for the transition is proportional to the observed ion signal.

It is instructive to consider the energy level diagram for the NO γ -band to discern the nature of the transitions. When the separation between $^2\Pi_{3/2}$ and $^2\Pi_{1/2}$ is large, as is the case in NO, the multiplets may be separated into two subbands. Selection rules, $\Delta J = 0, \pm 1$ and $+\leftrightarrow-$, allow six transitions in each subband, twelve total. Transitions which originate on the same J'' but terminate on different J' within the same K' are separated only by the spin splitting in the $^2\Sigma^+$. This separation is very small, and is not resolved in MPI. For the kinetic model, the equations for the four pair of coincident transitions must be solved differently than for the noncoincident transitions. The equations for noncoincident transitions have analytic solutions whereas the equations for coincident transitions must be solved numerically.

For the case of noncoincident transitions, the kinetics are described by a three level system (Fig 5-1a). X represents the population in a J'' level of the $^2\Pi$ state. A represents the population in a J' level of the $^2\Sigma^+$ state corresponding to a P, Q, or R transition. C represents the continuum of ion states. The rate constants k_{12} and k_{21} are for induced absorption and stimulated emission. k_{ion} corresponds to the ionization cross section. The spontaneous emission rate, $1/\tau$, is negligible assuming a 5ns laser pulse, but is included for completeness. The intermediate state lifetime is taken as 216 ns.²¹

Equations 5-1 to 5-3 are differential equations for the rate of change of population in X, A, and C.

$$dX(t)/dt = -k_{12}X + k_{21}A \quad (5-1)$$

$$dA(t)/dt = -(k_{12} + k_{\text{ion}} - 1/\tau)A + k_{12}X \quad (5-2)$$

$$dC(t)/dt = k_{\text{ion}}A \quad (5-3)$$

Equations 5-1 and 5-2 are simultaneously solved to yield expressions for X(t) and A(t).

$$X(t) = (r_2 + k_{12}/r_1 - r_2)[e^{r_2 t} - e^{r_1 t}] \quad (5-4)$$

$$A(t) = \{(r_1 + k_{12})(r_2 + k_{12})/k_{21}(r_1 - r_2)\}[e^{r_2 t} - e^{r_1 t}] \quad (5-5)$$

$$r_1 = \{-(m + k_{12}) + [(m + k_{12})^2 - 4(mk_{12} - k_{12}k_{21})]^{1/2}\}/2$$

$$r_2 = \{-(m + k_{12}) - [(m + k_{12})^2 - 4(mk_{12} - k_{12}k_{21})]^{1/2}\}/2$$

$$m = k_{21} + k_{\text{ion}} + 1/\tau$$

Equation 5-5 is substituted into equation 5-3 for a solution to C(t)

$$C(t) = \{k_{\text{ion}}(r_1 + k_{12})(r_2 + k_{12})/k_{21}(r_1 - r_2)\} \{(e^{r_2 t} - 1)/r_2 - (e^{r_1 t} - 1)/r_1\} \quad (5-6)$$

The initial conditions set A(0) and C(0) equal to zero and X(0) equal to one. By letting X(0)=1, X(t), A(t), and C(t) at all later times are the fraction of the NO number density in these levels.

For the case of coincident transitions, the kinetic system includes two separate intermediate levels (Fig 5-1b). The differential equations for this four-level system are Eqs. 5-7 to 5-10.

$$dX(t)/dt = k_{21}A + k'_{21}A' - (k_{12} + k'_{12})X \quad (5-7)$$

$$dA(t)/dt = k_{12}X - (k_{21} + k'_{21} + 1/\tau)A \quad (5-8)$$

$$dA'(t)/dt = k'_{12}X - (k'_{21} + k'_{21} + 1/\tau)A' \quad (5-9)$$

$$dC(t)/dt = k_{\text{ion}}A + k'_{\text{ion}}A' \quad (5-10)$$

An analytic solution for the four-level system may be found using Laplace transforms, but the equations are more easily integrated numerically.

To complete the model of predicting MPI ion signals from first principles, the rate coefficients, k_{12} and k_{21} , must be determined from spectroscopic parameters. From Einstein's theory for two-level systems the induced absorption and stimulated emission rates are written:

$$W_{12} = B_{12}\rho_{\omega}N_1 \quad (5-11)$$

$$W_{21} = B_{21}\rho_{\omega}N_2 \quad (5-12)$$

W_{12} and W_{21} are the rates of induced absorption and spontaneous emission. B_{12} and B_{21} are the Einstein B coefficients with units of $s^{-1}(\text{Jcm}^{-3}\text{\AA}^{-1})^{-1}$. ρ_{ω} is the energy density in units of $\text{Jcm}^{-3}\text{\AA}^{-1}$. The rate coefficients k_{12} and k_{21} are the product of the Einstein B coefficient and the energy density.

The Einstein B coefficients are related to the line strength, S , of a ro-vibrational transition according to Eqs 5-13 to 5-14.

$$B_{12} = (2\pi^2\lambda^2/3h^2\epsilon_0cg_1)S \quad (5-13)$$

$$B_{21} = (2\pi^2\lambda^2/3h^2\epsilon_0cg_2)S \quad (5-14)$$

g_1 and g_2 are the electronic statistical weights for levels 1 and 2. For diatomics, the electronic statistical weight is expressed as

$$(2-\delta_{0\Lambda})(2S+1). \quad (5-15)$$

The Kronecker delta, $\delta_{0\Lambda}$, is one for $\Lambda = 0$, that is Σ states, and zero for all other states. This gives an electronic statistical weight of 2 to the $^2\Sigma^+$ state and 4 to the $^2\Pi$ state.¹⁶

The line strength is the product of the band strength and the Hönl-London factor for the transition divided by the sum of the Hönl-London factors for all transitions in the band.¹⁶

$$S = (\text{Hönl-London})(\text{Band strength})/(2-\delta_{0\Lambda})(2S+1)(2J+1) \quad (5-16)$$

The Hönl-London factors have been tabulated for the $^2\Sigma-^2\Pi$ case.¹⁵ Absolute values of the band strength for the $\gamma(0,0)$, $\gamma(1,0)$, $\gamma(2,0)$, and $\gamma(3,0)$ bands have been measured.¹⁹ For other bands the band strength may be approximated as the product of a Franck-Condon factor and the square of the electronic transition moment.

$$\text{Band strength} = q_{v',v''}R_e^2 \quad (5-17)$$

The electronic transition moments have been reported as a function of the r -centroid for the $v' = 0$.

1, 2, and 3 progression.¹⁷ These are relative transition moments for each progression expressed as $R_v = (\text{constant}) \times f(r\text{-centroid})$. Comparison of the $q_{v',v''} R_e^2$ product and the absolute band strengths¹⁸ allows the constant to be evaluated and all band strengths to be on an absolute scale.

The rate constant k_{ion} is derived from the ionization cross sections reported for $v' = 0, 1$, and 2.²² The Einstein B coefficient is related to the cross section through the relation²³

$$B_{12} = \int \sigma_v dv / h\nu_0. \quad (5-18)$$

σ_v is the experimental ionization cross section at the frequency ν_0 . The integral is over the laser bandwidth which is approximated as a gaussian. The resulting B coefficient is changed to units appropriate to energy density by multiplication by the speed of light. NO has a very high ionization cross section. The rate constant for ionization may be of the same order of magnitude as the induced absorption and spontaneous emission rate constants for weaker transitions.

3. RESULTS AND DISCUSSION

A. COMPARISON WITH EXPERIMENT

With the connection made between the rate constants and the spectroscopic parameters, the ion yield for given laser intensity and pulse duration may be calculated. Figure 5-2 shows a plot of level population vs. time for the $\gamma(0,0)$ $R_{21}(10.5)$ transition of NO with a laser intensity of 150 mW/cm², bandwidth of 1 cm⁻¹. The populations of X and A reach a steady state value determined by the ratio of statistical weights (electronic and rotational) for the two levels. As time increases the population of these two levels decreases due to production of ions and the spontaneous emission from A to other v'' and J'' in X. The population of C and hence the ion signal is not separately a function of laser intensity and pulse duration but depends on the fluence, $I\Delta t$. For the rest of this paper, ion signals will be reported as functions of $I\Delta t$ in mJ/cm².

Zare *et. al.*¹⁴ reported isopower spectra for a portion of the $\gamma(0,0)$ band at differing integrated laser powers (Fig. 5-3a). Fig 5-3b shows the same spectra as produced using the kinetic model described above. For converting from the reported integrated laser power to energy density, a bandwidth of 0.7 cm⁻¹ has been assumed, estimated from the resolution of rotational lines. The transition frequencies for the Q_1+P_{21} and R_{21} branches as determined by the molecular constants¹⁷ do not match exactly with the positions in the experimental spectra. In the synthesized spectra the Q_1+P_{21} branch was shifted to give the same overlap as in the experimental spectra. The relative agreement between the features of the experimental and synthesized spectra for different integrated laser powers illustrates the effectiveness of the the kinetic model.

The quantitative capabilities of the kinetic model are better exemplified by comparison with a plot of ion signal vs. integrated laser intensity. Fig. 5-4a is such a plot for the $R_{21}(10.5)$ transition in the $\gamma(0,0)$ band as obtained experimentally.¹⁴ Fig 5-4b shows the ion signal dependence on laser power for the same transition as obtained from the kinetic model. Since in the experimental spectra the $R_{21}(10.5)$ line is not distinguished from the $Q_1+P_{21}(21.5)$ the ion signal is taken as the sum of the two transitions.

Since $(1+1)$ MPI requires the absorption of two photons for an ionization event, the dependence of the ion signal on the laser power should be quadratic. When the resonant ground to intermediate state step is saturated, the ion signal depends only on the rate of ionization and should be linear with respect to the laser power. Fig 5-4 shows that the ion signal is neither quadratic nor linear with respect to the laser power. To understand more clearly this intermediate behavior of the ion signal, it is useful to prepare a plot of the $\ln(\text{ion signal})$ vs. $\ln(\text{integrated laser power})$, Fig. 5-5. Since the ion signal is proportional to the laser power to some exponent, $S \propto I^\alpha$, the slope of a log plot indicates the laser power dependence. The figure shows that over a great range the dependence is quadratic, and at high powers goes to zero. The zero dependence on the integrated laser intensity means the energy density is great enough that within the duration of the laser pulse all molecules within the beam are converted to ions. Clearly this would be the ideal region to work in, but it is unfortunately a few orders of magnitude away from current laser powers. The transition region between the quadratic and zero dependences is where current laser powers allow experiments to be performed. Unfortunately this is also the region where the analysis of the ion signal is most difficult.

B. VIBRATIONAL SUBBAND RELATIONS

An expression for the ion signal may be written as in equation 5-19 where S is the ion signal, a is an instrument constant, N_{ion} is the fraction of the NO number density within the laser beam converted to ions in one pulse, and $[\text{NO}]$ is the NO number density.

$$S = aN_{\text{ion}}[\text{NO}] \quad (5-19)$$

The quantity of interest here is the fraction of ions produced, N_{ion} . It has been assumed in $(1+1)$ MPI studies of the vibrational population distribution of ground state NO molecules⁶⁻¹² that at saturation conditions the differences in bandstrengths will no longer have an effect on the spectra. The form of the spectra is determined only by the differences in the statistical weights of the X and A levels and the Boltzmann distribution in the X state. The ion signals should be linear with respect to laser fluence, and recording signals in A/B mode should correct for fluctuations in laser power. This picture assumes a very rapid equilibration between the X and A levels, an ionization rate much less than the induced absorption or stimulated emission rates, and an ionization cross section independent of wavelength and intermediate state quantum numbers. These conditions are not met exactly, but with the kinetic model described above, it is straightforward to calculate how the ion signal varies for different vibrational bands. Figure 5-6 shows N_{ion} divided by the integrated pulse energy as a function of integrated pulse energy for the first four vibrational levels of NO at the $R_{21}(10.5)$ line. At sufficiently high laser fluence, the flat slope expected for linear dependence is observed, but the fraction of ions produced in the different vibrational bands is different at all integrated laser intensities. This means the same ion signal measured at the same laser power for different vibrational bands corresponds to *different* ground state number densities. Clearly any measurements of the vibrational population distribution will need to correct for this variation.

For measuring vibrational populations using $(1+1)$ MPI, we make the following suggestions. Ion signals should be recorded in the method outlined by Jacobs and Zare¹³. From the curves of

ion signal vs. integrated laser intensity, a common, central integrated laser intensity is chosen. The bandwidth of the laser and the average pulse duration should be well-known experimentally. The fraction of the ground state number density converted into ions at these conditions is calculated for each of the vibrational bands measured using a model such as described above or perhaps a more complicated model if the experimental conditions necessitate it.⁶ A calibration curve of the ground vibrational state is made using known number densities. The ratio of the fraction of ions produced in the ground vibrational level to all of the other vibrational levels is used to correct the ion signals to the calibration curve for the ground state. For example, if 20% of the γ -(0,0) band is converted to ions but only 10% of the γ -(1,1) band is, the ion signal for the γ -(1,1) band must be multiplied by two to represent the same percent of the number density at which the calibration curve was made.

C. CORRECTION OF PREVIOUS KINETIC RESULTS

In reference 11 the product vibrational distribution of the $N(^4S) + O_2 \rightarrow NO(v=0-7)$ was measured using (1+1) MPI. The variations in ion signal for the different vibrational levels was not taken into consideration when this work was done. We will correct these kinetic results using the methods outlined here. The kinetic runs were recorded in A/B mode, so from a plot such as was shown in Fig. 5-6, we will be able to correct for the different ion fractions for each of the subbands. Unfortunately the data was recorded at the P_1 bandhead. While this is the most intense spectral feature, it is composed of many transitions. This makes estimating the fraction of ions produced more difficult because many lines must be summed. Figure 5-7a to 5-7g is a plot similar to figure 5-6 except these are the ion fractions for the P_1 bandhead.

4. CONCLUSIONS

A method of relating ion signals measured in (1+1) MPI to ground state number densities for different vibrational bands has been presented.

The kinetic model outlined in this paper gives good agreement with the experimental ion signal dependence on laser fluence. The good agreement with experiment suggests that the model may be used as a method of obtaining absolute ionization cross sections. Experimental ion signal versus integrated laser power curves may be fitted by the model using the ionization cross section as the only adjustable parameter.

Using normalization, Franck-Condon and our knowledge of the usual form of linear surprisals along with the approach outlined here, we should be able to correct the results for the $N(^4S) + O_2 \rightarrow NO(v=0-7) + O(^3P)$ reaction.

REFERENCES

- ¹J.R. Ackerhalt and B.W. Shore, Phys. Rev. A **16**, 277 (1977).
- ²D.S. Zakheim and P.M. Johnson, Chem. Phys. **46**, 263 (1980).
- ³P. Cremaschi, P.M. Johnson, and J.L. Whitten, J. Chem. Phys. **69**, 4341 (1978).
- ⁴D. H. Parker, J.O. Berg, and M.A. El-Sayed, in *Advances in Laser Chemistry*, edited by A.H. Zewail (Springer, New York, 1978).
- ⁵P.M. Johnson and C.E. Otis, Ann. Rev. Phys. Chem., **32**, 139 (1981).
- ⁶W.Gary Mallard, J. Houston Miller, and Kermit C. Smyth, J. Chem. Phys. **76**, 3483 (1982).
- ⁷M. Asscher, W.L. Guthrie, T.H. Lin, and G.A. Somorjai, Phys. Rev. Lett. **49**, 76 (1983).
- ⁸N. Goldstein, G. Greenblatt, and R. Wiesenfeld, Chem. Phys. Lett. **96**, 410 (1983).
- ⁹Charles S. Feigerle and John C. Miller, J. Chem. Phys. **90** 2901 (1989).
- ¹⁰C.S. Feigerle and J.C. Miller (to be published).
- ¹¹I.C. Winkler, R. Stachnik, J.I. Steinfeld, and S. Miller, Spectrochim. Acta Part A **42** 339 (1986).
- ¹²I.C. Winkler, R.A. Stachnik, J.I. Steinfeld, and S.M. Miller, J. Chem. Phys. **85**, 890 (1986).
- ¹³D.C. Jacobs and R.N. Zare, J. Chem. Phys. **85**, 5457 (1986).
- ¹⁴D.C. Jacobs, R.J. Madix, and R.N. Zare, J. Chem. Phys. **85**, 5469 (1986).
- ¹⁵L.T. Earls, Phys. Rev. **48**, 423 (1935).
- ¹⁶J.B. Tatum, Astrophys. J. Suppl. Ser. XIV, No. 124, **21** (1967).
- ¹⁷D.C. Jain and R.C. Sahni, Trans. Faraday Soc. **64**, 3169 (1968).
- ¹⁸R. Engleman, Jr. and P.E. Rouse, J. Mol. Spectrosc. **37**, 240 (1971).
- ¹⁹A.J.D. Farmer, V. Hasson, and R.W. Nicholls, J. Quant. Spectrosc. Radiat. Transfer. **12** 627 (1972).
- ²⁰G. Herzberg, *Molecular Spectra and Molecular Structure. II. Infrared and Raman Spectra of Polyatomic Molecules* (Van Nostrand Reinhold, New York, 1945).
- ²¹H. Zacharias, J.B. Halpern and K.H. Welge, Chem. Phys. Lett., **43**, 41 (1976).
- ²²F. deRougmont, H. Zacharias, T.F. Heinz, and M.M.T. Loy, CLEO (1989).
- ²³J.I. Steinfeld, *Molecules and Radiation, 2nd ed.* (MIT Press, Cambridge, MA, 1985).

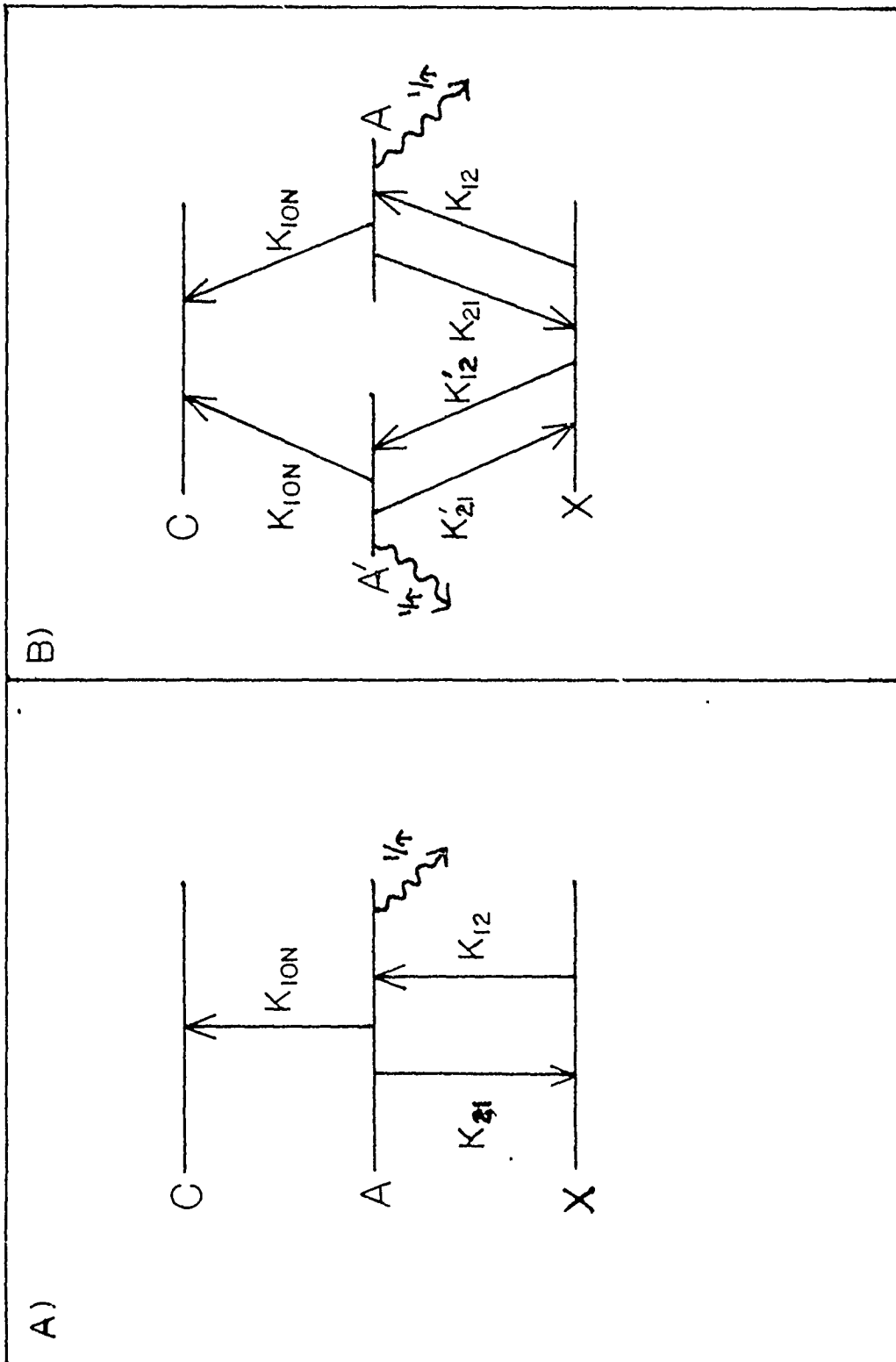


FIG. 1. A) Schematic drawing representing the processes of induced absorption, stimulated emission, spontaneous emission, and ionization for a noncoincident transition, a 3-level system. B) Similar schematic for a coincident transition, a 4-level system.

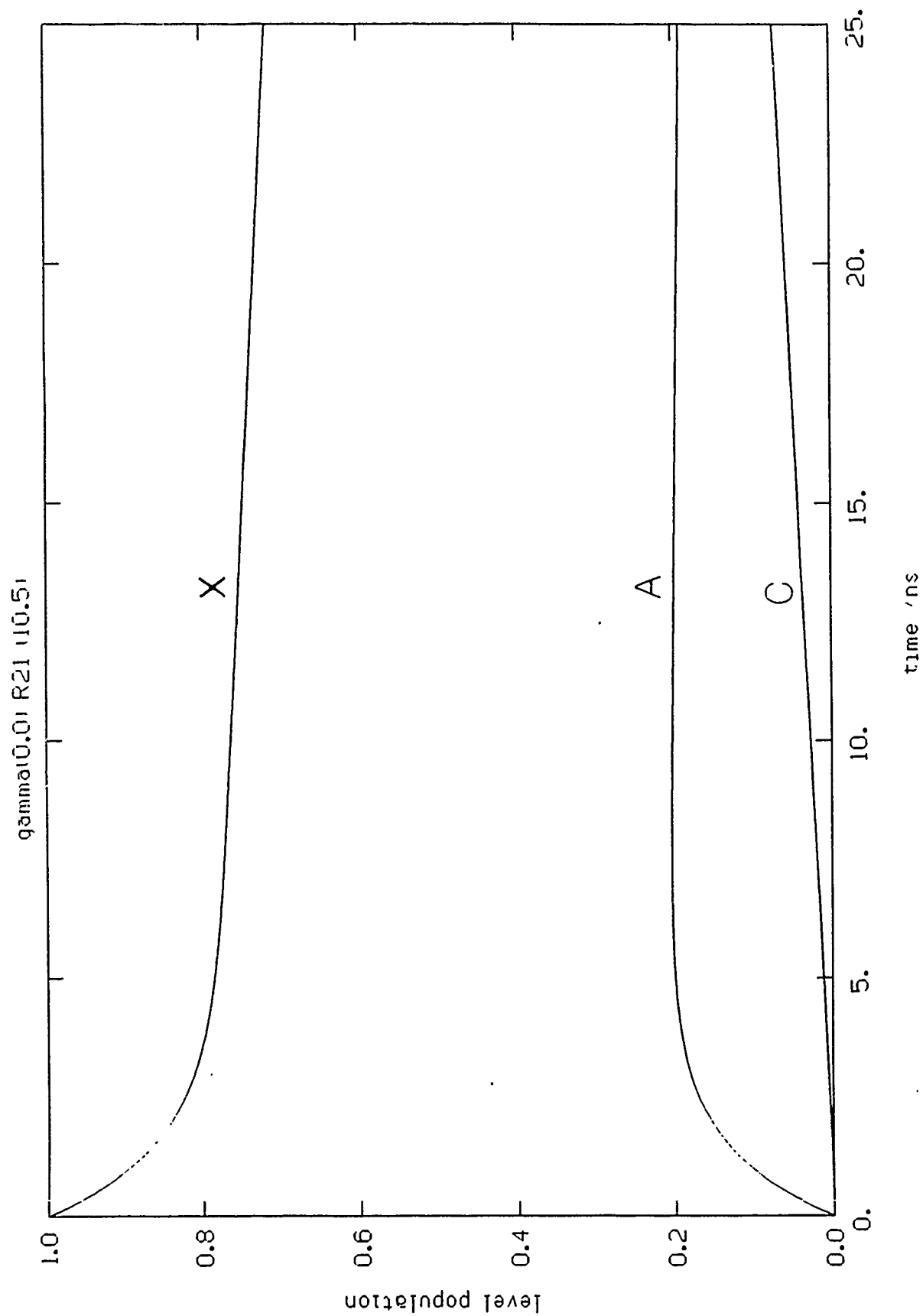


FIG. 2. The drawing shows the time evolution of the ground (X), intermediate resonant (A), and ion states (C) at a laser intensity of 1 mW/cm^2 .

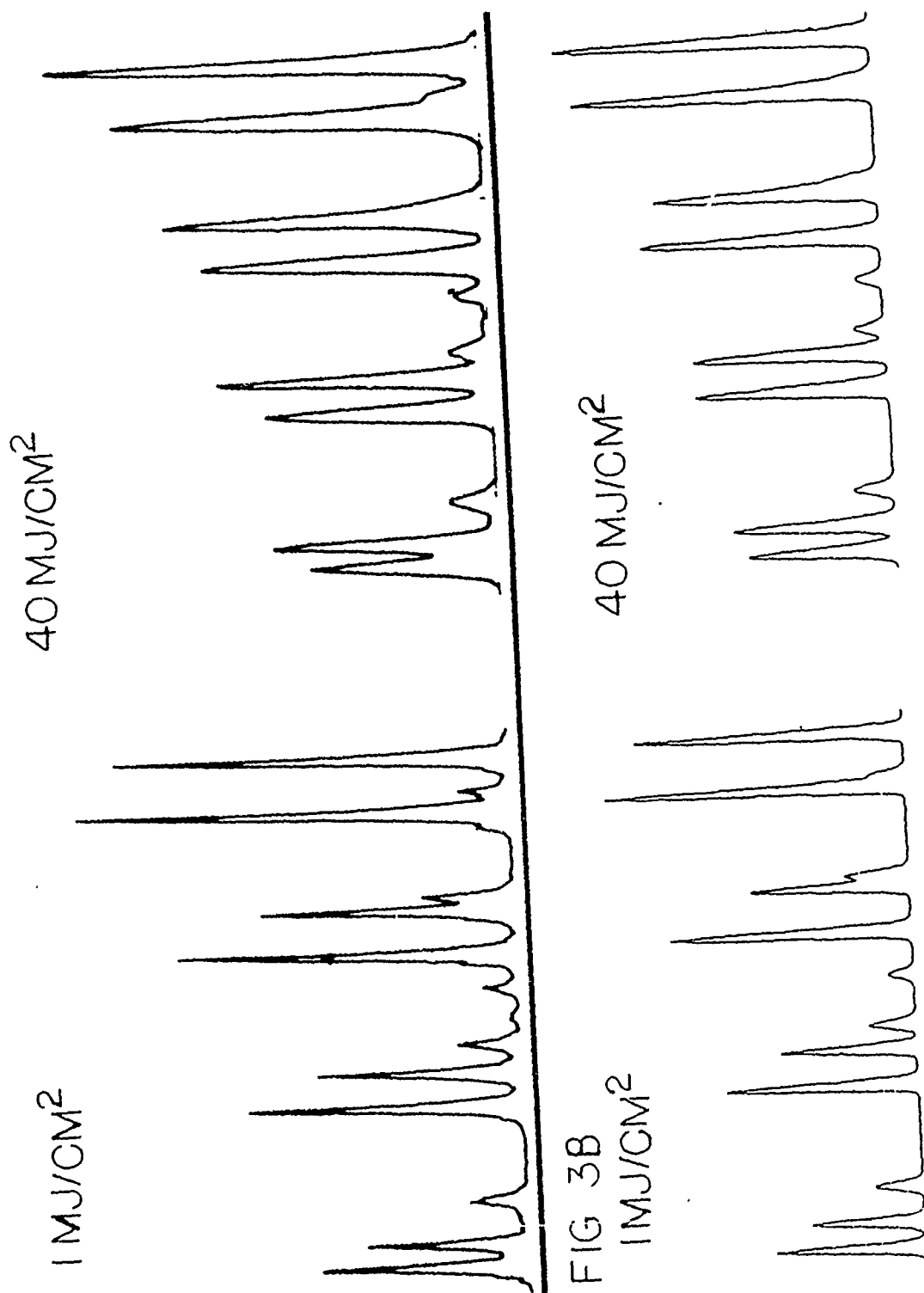


FIG. 3. A) A portion of the NO $\gamma(0,0)$ band at 225.50 nm recorded under isopower conditions (ref. 14). B) Calculated spectra under the same conditions using the kinetic model.

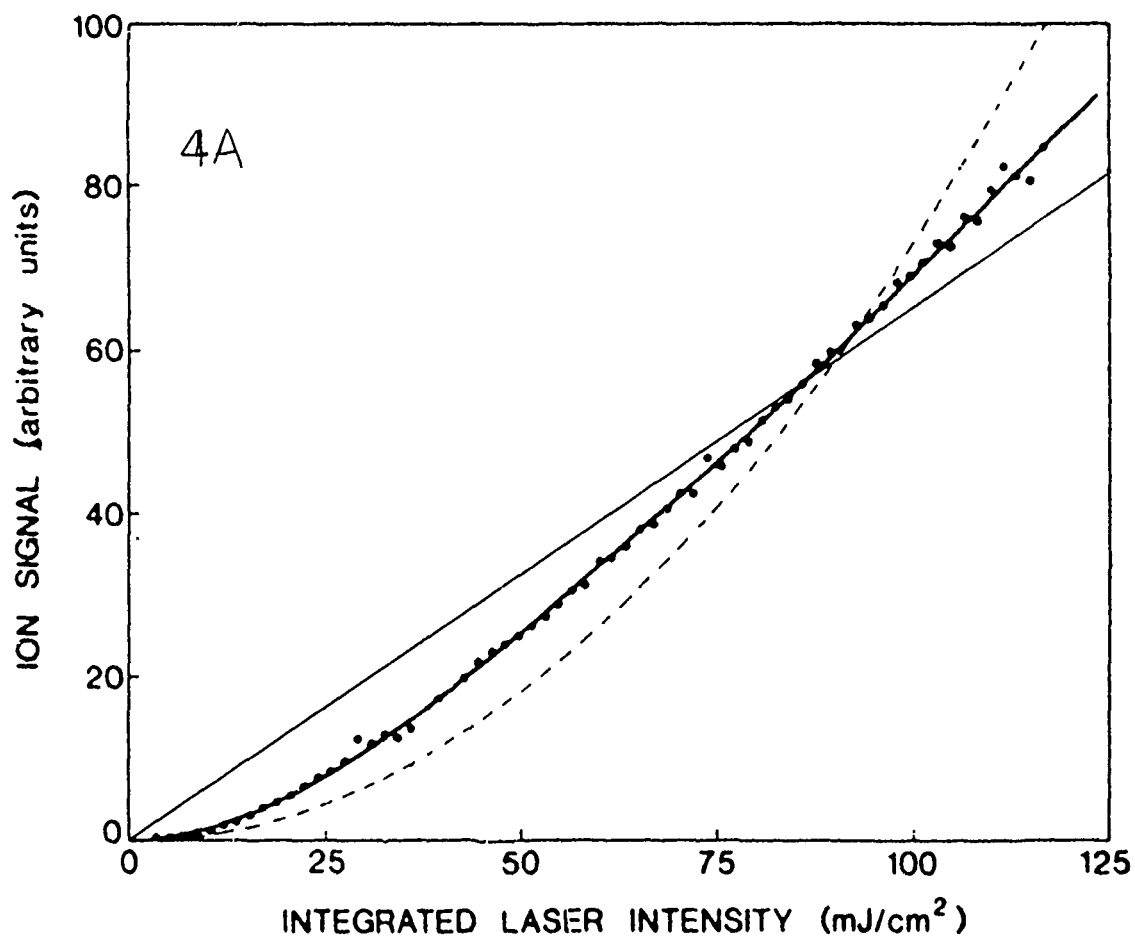
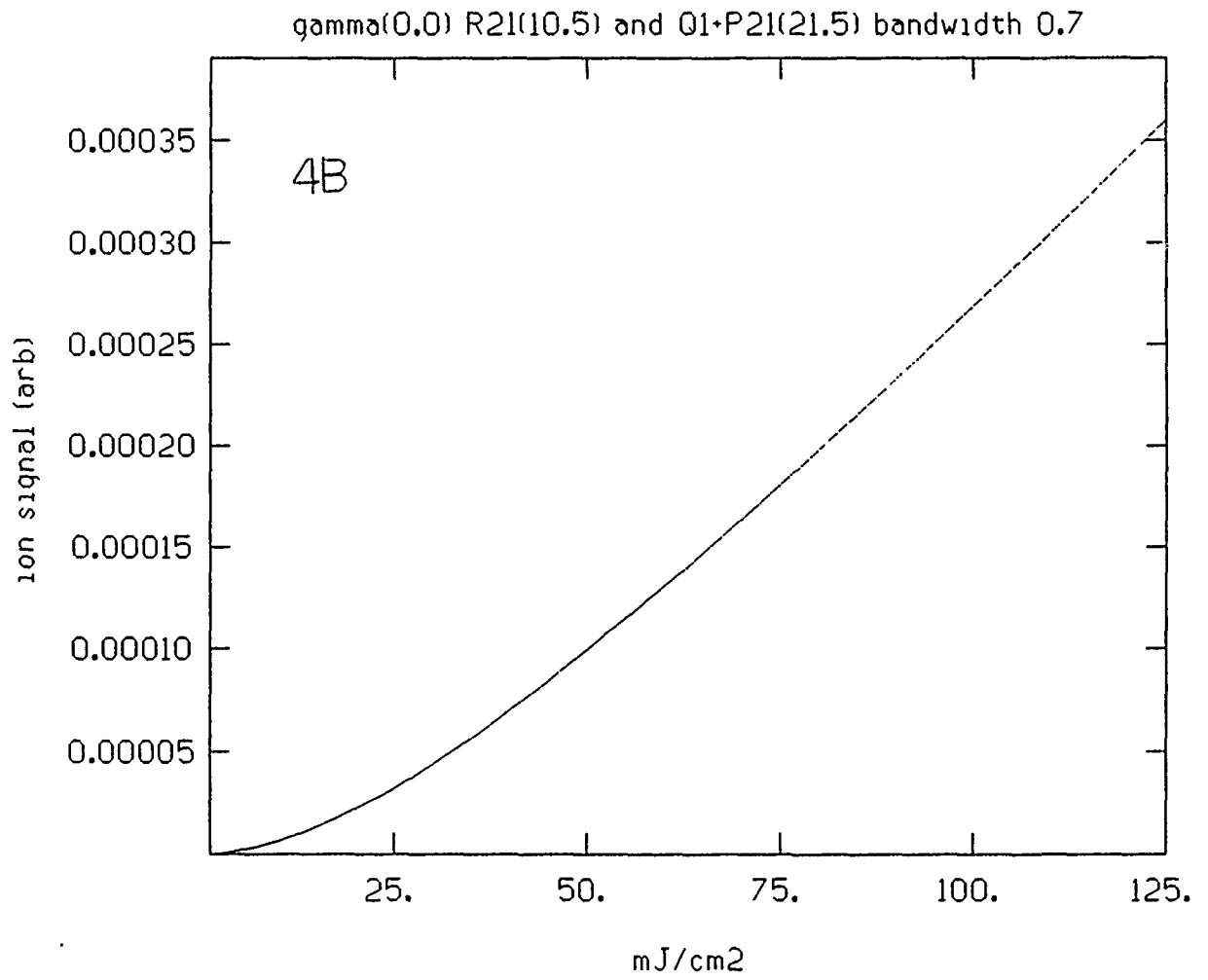


FIG. 4. A) A plot of ion signal vs. laser fluence showing intermediate behavior between linear and quadratic (ref. 14). B) A plot for the same transition as in A), but using data from the kinetic model.



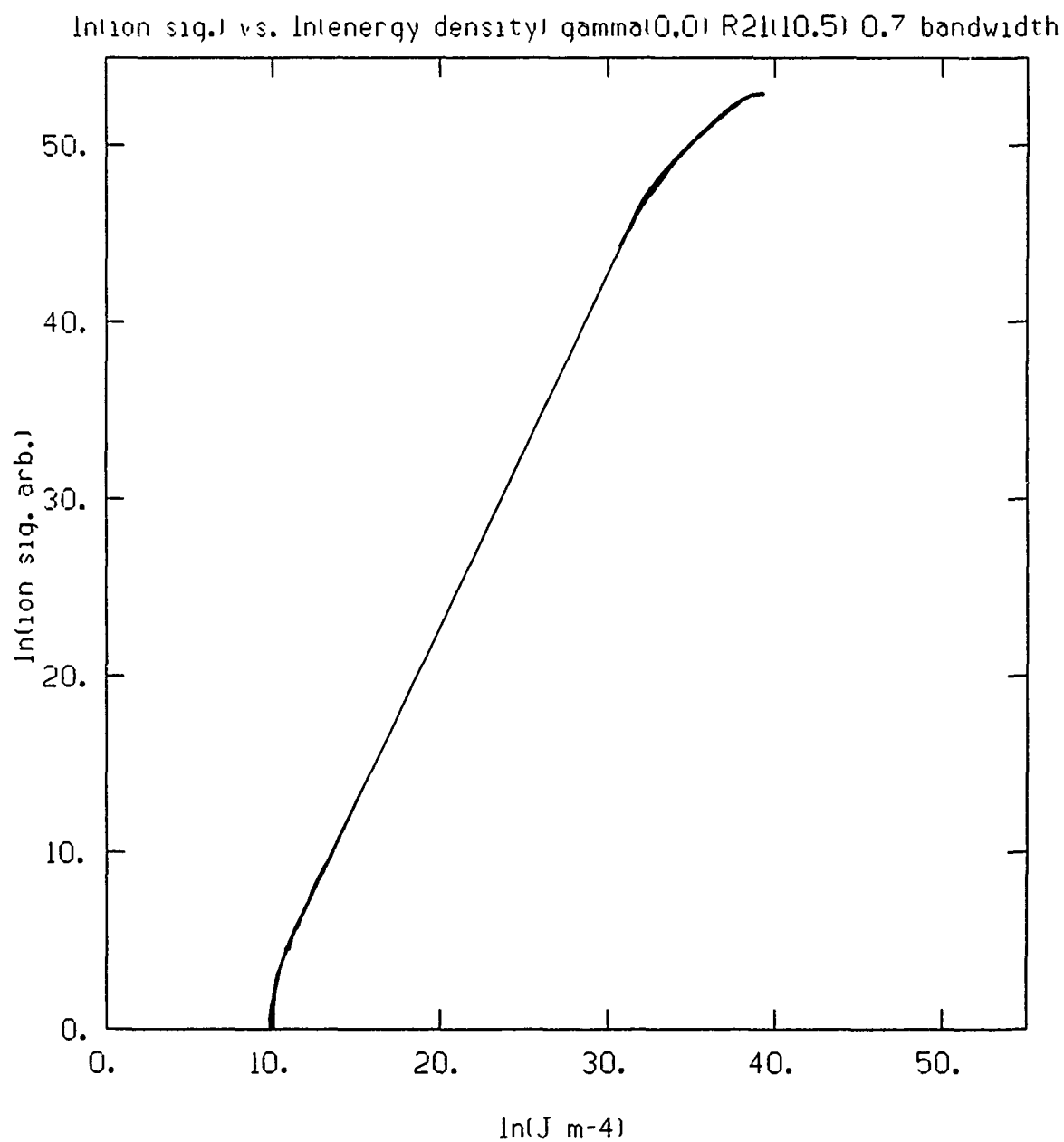


FIG. 5. A plot of the natural log of the ion signal vs. the laser energy density showing that linear dependence of the ion signal on laser power is really a transition between quadratic and zeroth order behavior.

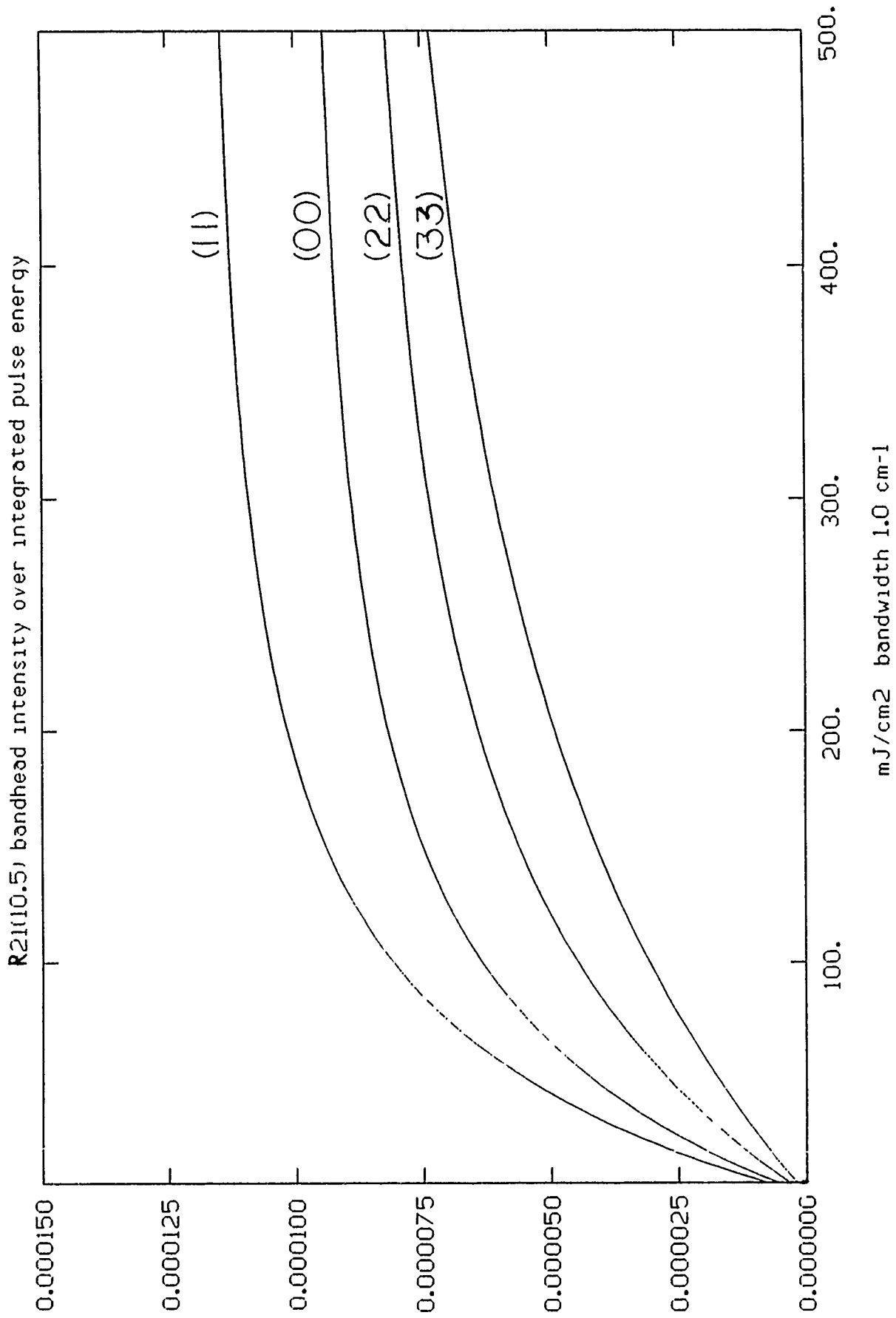


FIG. 6. A plot showing the expected dependence of the ion signal on laser fluence for the $R_{21}(10.5)$ line as recorded in A/B mode.

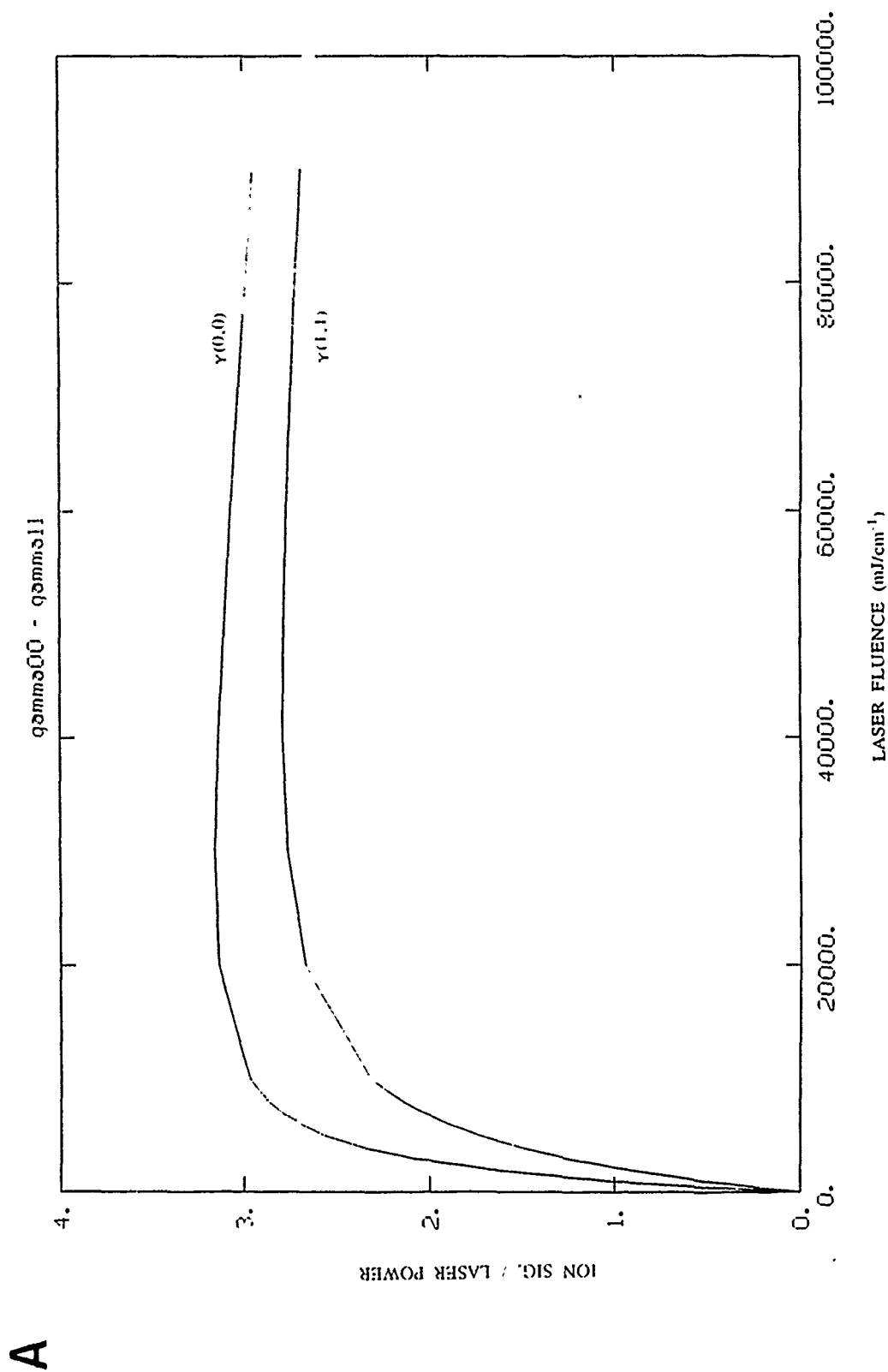
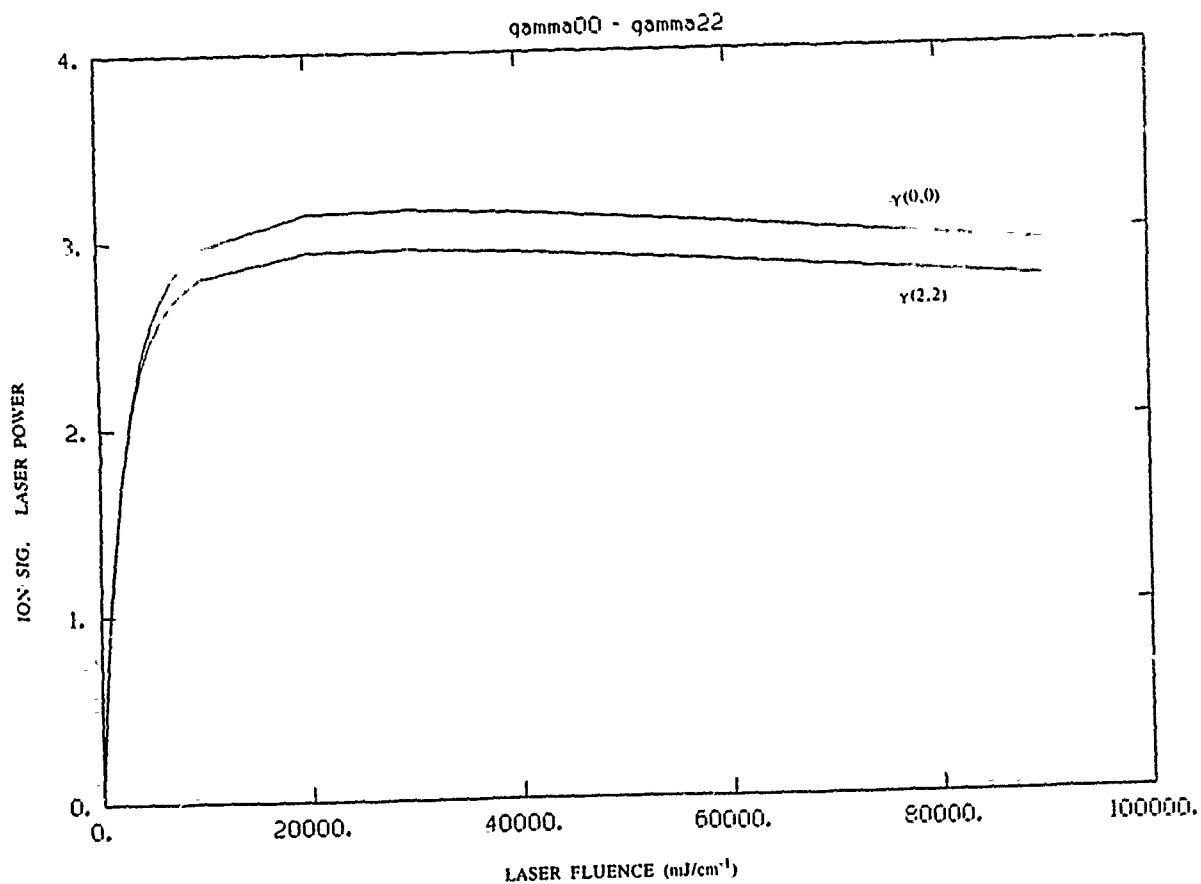
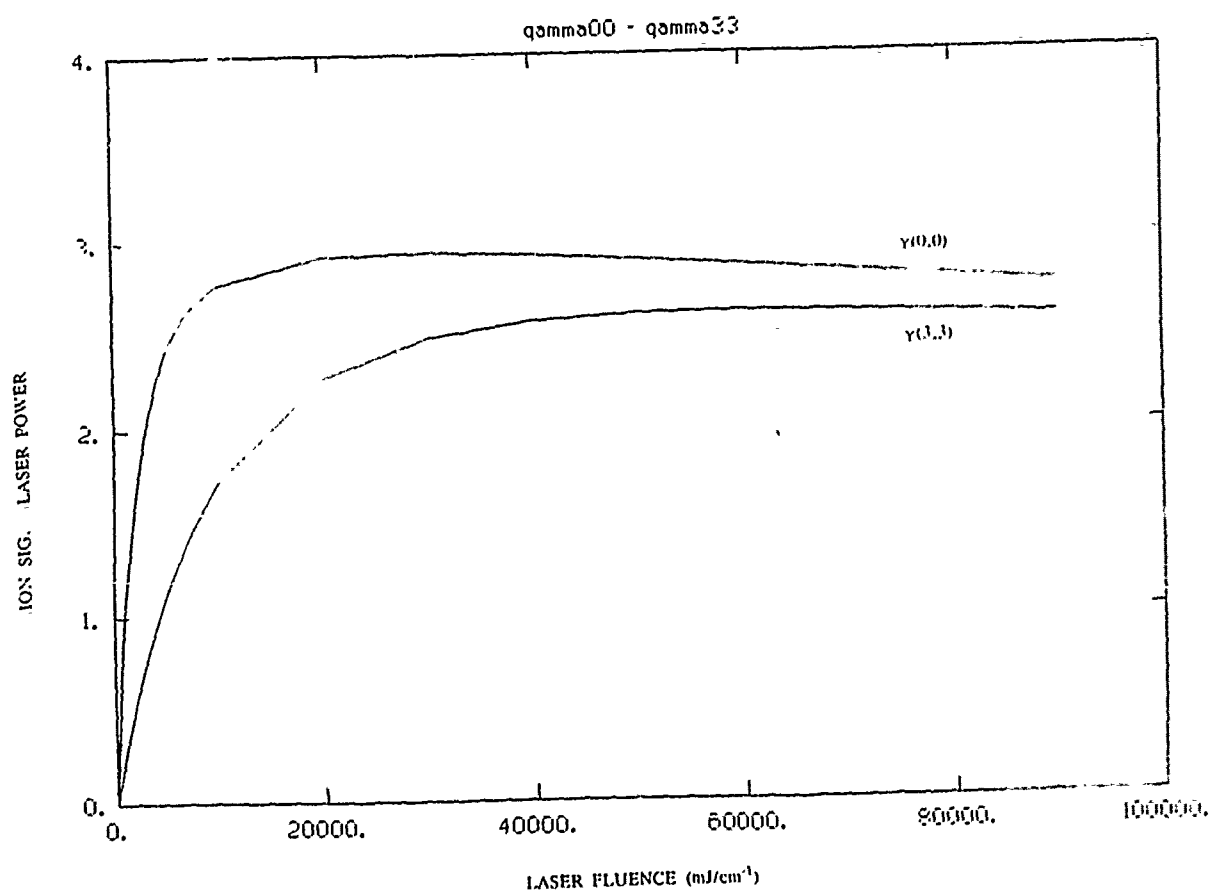
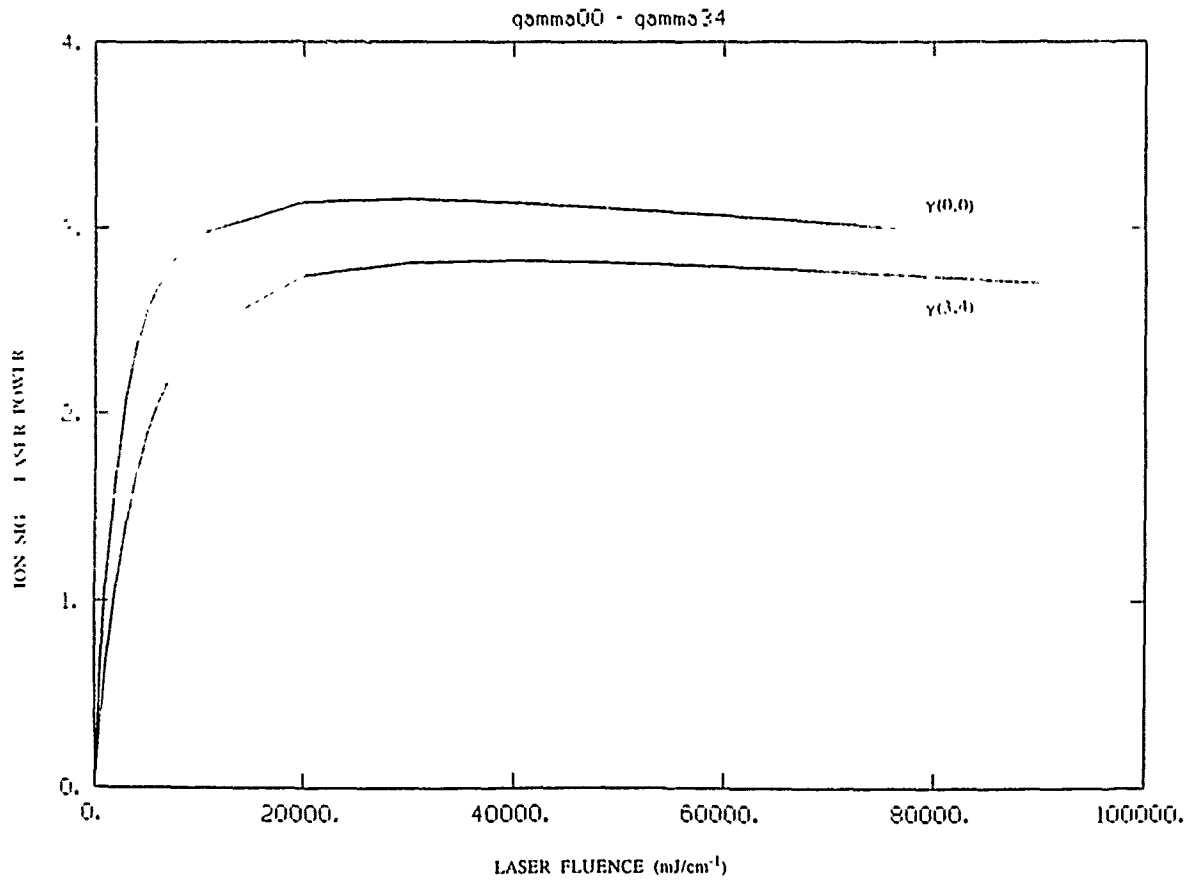


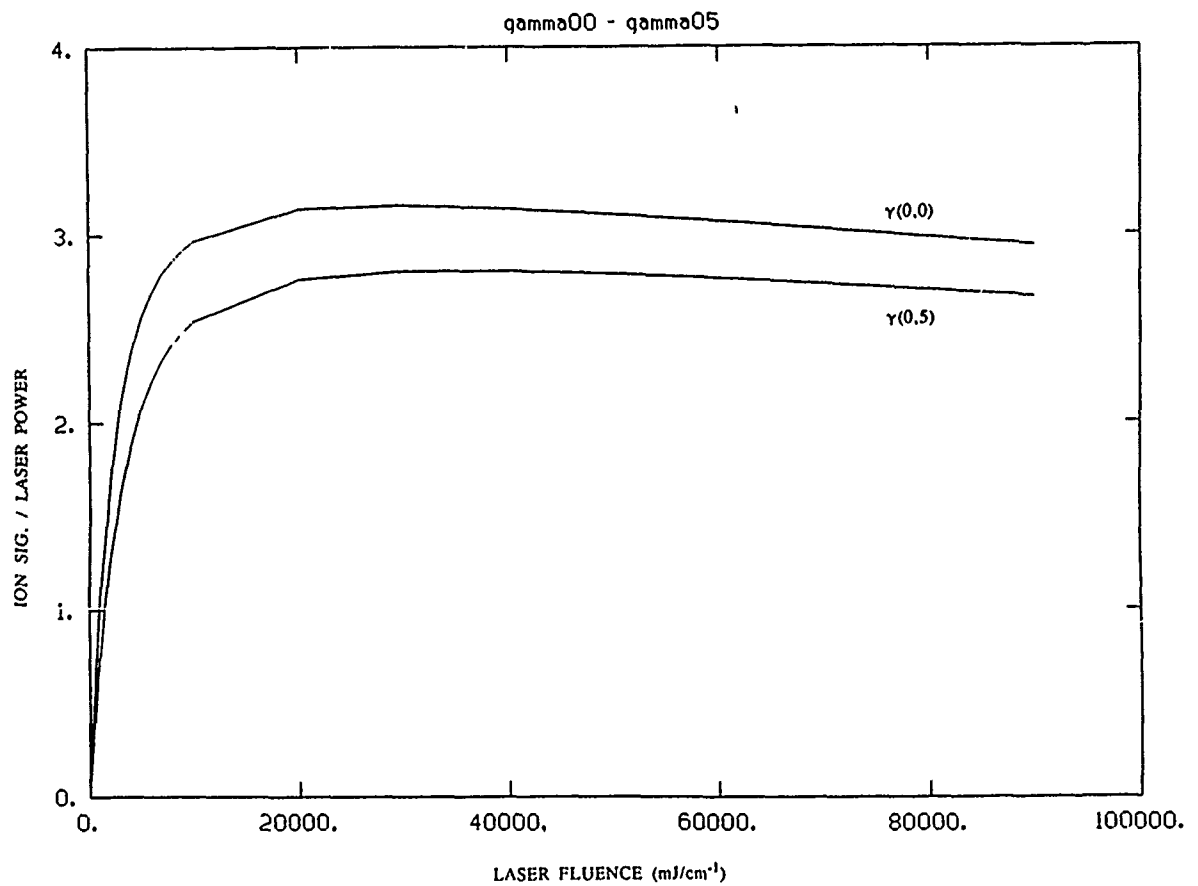
FIG. 7 (Next four pages) Predicted dependence of the ion signal on laser fluence for the P_1 bandhead, normalized by laser fluence. The gamma (0,0) band intensity is included on each panel for reference. (A) Gamma (1,1) band. (B) Gamma (2,2) band. (C) Gamma (3,3) band. (D) Gamma (3,4) band. (E) Gamma (0,5) band. (F) Gamma (1,6) band. (G) Gamma (1,7) band.

B**C**

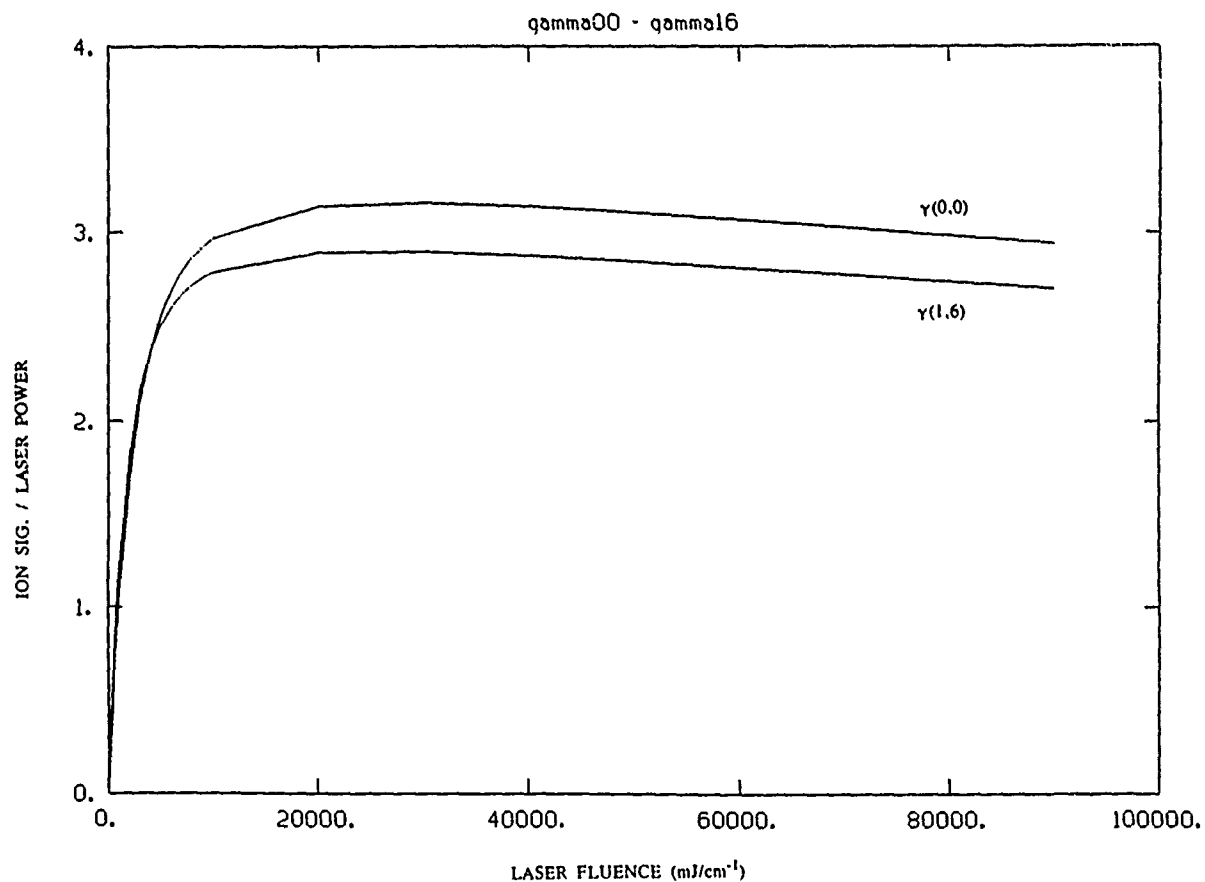
D



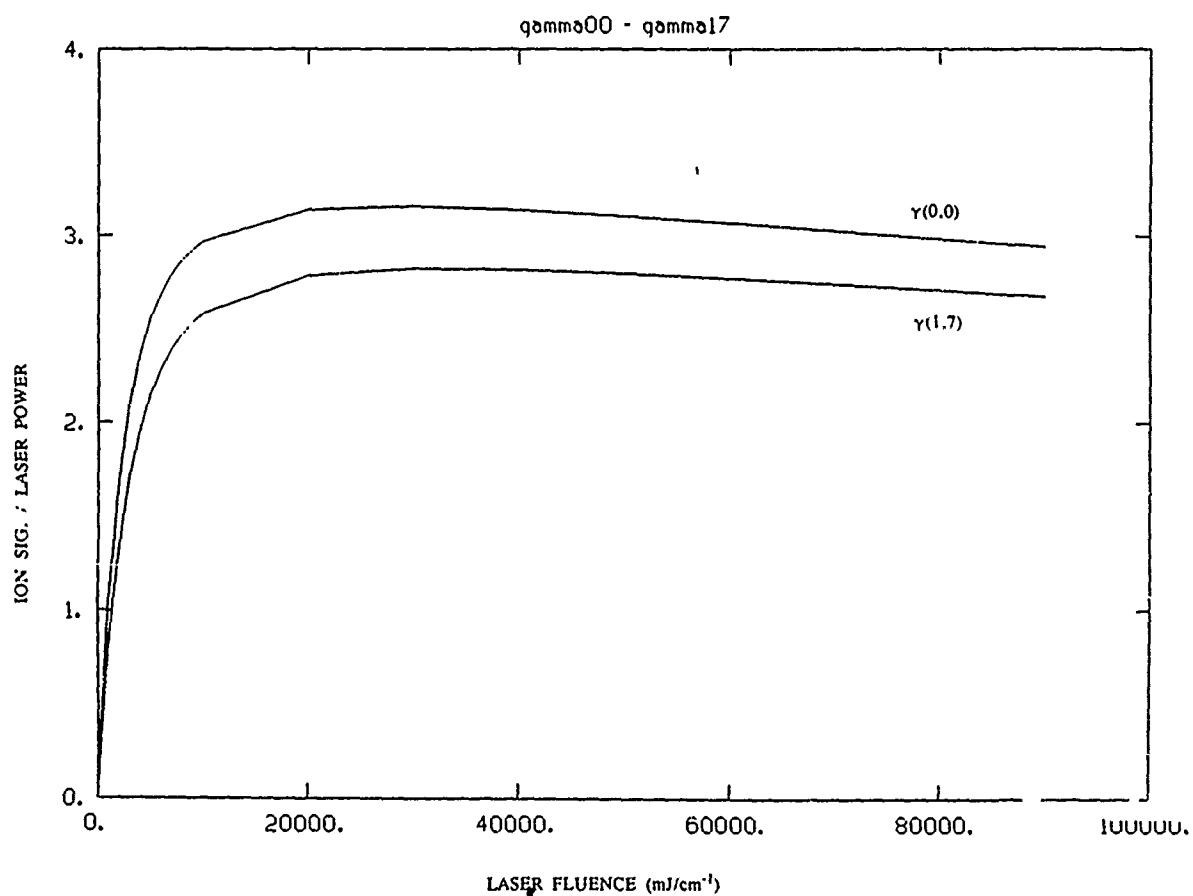
E



F



G



6. Stimulated-Emission-Pumping of Nitric Oxide

6.1. Introduction

There is much interest in dynamics of high vibrational levels of nitric oxide. NO($v=1$ to 18) is formed chemically in the upper atmosphere, and contributes significantly to atmospheric infrared luminosity¹. By dissociating NOCl in a pulsed electrical discharge, Deutsch observed NO infrared laser action in the 5.84 to 6.43 μm range, corresponding to the $v=6-11$ fundamental emission². Experiments on an ultraviolet NO laser, pumping the $\gamma(0,0)$ band at 227 nm, have produced 10 μJ pulses at 237 and 248 nm, corresponding to the $\gamma(0,1)$ and $\gamma(0,2)$ bands³. In order to obtain a quantitative description of these phenomena, it is necessary to determine the state-specific vibrational-to-vibrational (V-V) and vibrational-to-translational (V-T) energy transfer rates. Studies indicate that deactivation of NO ($v''=1$) by a variety of collision partners is extremely efficient, compared to species of similar size and vibrational frequency such as CO, N₂, and O₂.^{1,4-9} Room temperature NO self-collisions are roughly 10^5 times more efficient in $v=1 \rightarrow 0$ deactivation than self-collisional deactivation in these other gases, and this efficiency increases as the temperature decreases below 200K.¹⁰ Two suggestions have been made to explain this unusual behavior. The first of these, proposed by Nikitin,¹¹ is that of the two interaction potentials between two $v=0$ free radicals, such as NO with its odd electron, one (Σ_g) is bound, while the other (Σ_u) is antibonding. The $v=1 + v=0$ surfaces are the same, except shifted up in energy by one vibrational quantum. Therefore, the binding surface of the $v=1 + v=0$ interaction crosses the antibonding surface of the $v=0 + v=0$ interaction. Thus, vibrational relaxation may be viewed as collision-induced intersystem crossing. While this may explain the highly efficient collisional deactivation, further examination of this scheme¹² indicates that the rates should decrease with temperature, contrary to observation. The second suggestion¹³ arises from the observation that the bonding well in these interactions is approximately 1.6 kcal mole⁻¹ (560 cm⁻¹, which is about 2.5kT at 300K). In such a case, a collision complex may form.

In addition to self-collisional deactivation rates, the deactivation rates with O₂ are rather high as well. Studies¹ have shown the NO($v=1-7$) + O₂ collisions are 10 to 100 times as efficient as

NO-noble gas collisions in inducing vibrational relaxation. These rates scale roughly with v^2 . This is in conflict with theories on V-T transfer, such as SSH (Schwartz-Slawsky-Herzfeld), which predicts the rates to scale linearly with v ¹⁴.

Much work has been done to measure these rates. Most of this work entailed collisionally exciting NO, and monitoring the decay of the infrared emission. Methods which have been used to collisionally activate NO include: high energy electron bombardment,^{1,2} electronic-to vibrational energy transfer from mercury atoms,⁹ and gas discharge¹⁵. These methods populate a range of vibrational levels, rather than individual levels. Therefore, extensive deconvolution of the data is required in order to retrieve the relaxation rates of individual quantum states. Additionally, it is often impossible to distinguish V-V from V-T energy transfer rates in these experiments, leading to large uncertainties.

A number of experimental programs under way in the Optical Physics and Infrared Technology Divisions of the Air Force Geophysics Laboratory require detailed state-to-state vibrational relaxation information for NO, including the COCHISE¹⁶⁻¹⁹, LABCEDE¹, FAKIR^{17,19}, and FACELIF²⁰ experiments. The observation of NO vibrational distributions is common to all of these experiments. However, in these experiments, some vibrational relaxation occurs between formation and detection of these distributions. While vibrational deactivation rates are determined in the LABCEDE work, vibrational excitation is not state-specific, and the assumptions which must be made in the deconvolution result in significant uncertainty (20-50% for $v=2-6$). More accurate rates, especially for deactivation by O₂, would improve the accuracy of all of these experimental results. This improvement may be realized by employing an experimental method in which one populates a single vibrational level and monitors the decay of this population. In this, there is no repopulation from a higher vibrational level (cascading mechanism), and the analysis is considerably less complex.

As an example of this need for improved measurement of NO(v) deactivation, consider the results from FACELIF.²⁰ Plots of [NO(v)] versus [O₂] show downward curvature at high [O₂]. The NO concentration is low enough in these experiments that self-collisional relaxation is not

thought to introduce significant error. However, the O_2 reactant is in high concentration, so that errors in the rates of O_2 -induced relaxation processes can lead to considerable uncertainty in the nascent vibrational distribution, and thus in the state-specific formation rates. This curvature has been analyzed to estimate the rate for deactivation by O_2 . Agreement between these results and the LABCEDE results was within experimental error (about 30%).

In addition to bettering the accuracy of the rates of these important atmospheric reactions, selective excitation of individual $NO(v)$ states would allow direct investigation of interesting mechanisms which seem to be occurring in these reactions. Most notably, the formation of high-J band heads in COCHISE has been attributed to the $N(^2P)$ reaction. However, one may also suggest that $NO(v) + O_2$ vibrational deactivation may proceed preferentially by vibration-to-rotation energy transfer to high-J levels. This suggestion is further strengthened by noting that one possible explanation for the extremely fast deactivation is the formation of an orbiting collision complex.

Two methods of selectively populating vibrational levels can be considered. The first, direct overtone pumping, has been used to study $v=2$ relaxation rates, including rotational and spin relaxation.²¹ However, because overtone absorption cross-sections tend to decrease geometrically with the change in v , higher vibrational levels cannot be populated directly. Stimulated emission pumping (SEP) was suggested as a more effective method of populating levels $v=6$ through $v=16$.

Kittrell and coworkers have demonstrated stimulated emission pumping of iodine.²² The "folded double resonance" or "pump/dump" technique utilizes two fully allowed transitions: excitation to an upper electronic state ("pump"), followed by stimulated emission to a selected vibrational level in the ground electronic state ("dump"). This technique is limited only by Frank-Condon factors, and has been applied to a number of chemical species, including HCN,²³ formaldehyde^{24,25}, and p-difluorobenzene.²⁶⁻²⁹ One may tune the dump laser while monitoring the fluorescence from the initially pumped state. When the dump laser wavelength corresponds to a resonance, one will see a decrease in the fluorescence due to the depletion of the population in the initially excited state. This is called, appropriately enough, "Fluorescence Dip Spectroscopy."

This is used more as a diagnostic for correctly setting the dump laser wavelength, but can be used to elucidate the spectroscopy of molecules which had not been determined by conventional means (e.g. dispersed fluorescence spectroscopy).

Once the population in the target vibrational state has been generated, the decay of this population may be followed using any number of probe techniques. These include Laser Induced Fluorescence, Multiple Photon Ionization, and Infrared Fluorescence or Absorption. If LIF is used, the technique is commonly called "Triple Resonance", in which the target level population is mapped out as the probe laser is delayed in time.

6.2 Evaluation of Available Pump Sources

6.2.1. SEP of NO using the ArF excimer pump

Our initial experiments used an ArF excimer laser as the pump source. NO absorbs 193 nm light via high J transitions of the $B^2\Pi(v'=7) \leftarrow X^2\Pi(v'=0)$ [$\beta(7,0)$] band³⁰. Because of the broad-band nature of the ArF excimer (approximately 100 cm^{-1}), many rotational states are populated via the transitions P(25-30) and R(28-33). One needs to stimulate emission from all of these levels in each laser shot for two reasons. First, if only one rotational level is depopulated, only a slight decrease in the fluorescence may be observed, rendering it very difficult to locate the fluorescence dip signal. Second, those molecules remaining in the upper state are then free to spontaneously radiate, thus jeopardizing the selectivity of the process. This is particularly hazardous in the NO $B \leftarrow X$ transitions, where the Franck-Condon distribution is quite broad. Therefore, in order to depopulate all of these levels, it is necessary to use a broad band source as the dump laser. As the output of this laser could not be frequency doubled, we were constrained to visible transitions, with target levels from $v''=19$ to 23.

The specifications of the Lumonics Excimer Laser limited the effectiveness of this approach. Because the ArF excimer is broad-band, the spectral brightness is low. The output beam is also quite large and divergent, necessitating the use of apertures and spatial filters, which lead to significant loss of power. Finally, this fixed frequency laser cannot be tuned to the band head, and

therefore accesses only high- J'' levels at the tails of the thermal rotational population distribution. We had intended to use isotopically substituted $^{15}\text{N}^{18}\text{O}$ to shift the maximum of the rotational distribution into better resonance with the laser. This technique has been used successfully in our laboratory, in which isotopically substituted methane($^{13}\text{CD}_4$) is used to bring a selected rovibrational transition into resonance with a fixed-frequency CO_2 laser line.^{31,32} In this case, as is shown below, such isotopic shifting was not sufficiently effective to overcome the other inherent problems.

In order to quantify the limitations of the ArF excimer approach to the stimulated emission pumping of NO, we can compare it to the work done in Professor A.E.W. Knight's laboratory at Griffith University (Queensland, Australia) on I_2 in a free jet expansion. This way, we can obtain a good estimate of the signal-to-noise ration which may be expected, based on experience.

In these experiments, the output from one Nd:YAG laser (Molelectron) was split, and used to pump the two dye lasers (Molelectron and Lumonics) which were used in the SEP pump-dump step. Another Nd:YAG-pumped dye laser (Molelectron) was used as the probe. Each of these provided 10 ns pulses with a few mJ in the visible. The (20,0) transition near 560 nm was pumped, and fluorescence from the $v'=20$ level was dispersed. We set the monochromator on the (20,4) dump transition at 586 nm, then tuned the dump laser until scattered light at this wavelength was maximized. The PMT was equipped with a band-pass filter ($\lambda_c=532$ nm, $\Delta\lambda=10$ nm FWHM) to protect it from scattered light, and also from fluorescence due to pump only. With this mounted on the vacuum chamber, we tuned the probe laser to the (24,4) transition at 555 nm, and observed the (24,0) fluorescence at 532 nm. The triple-resonance signal was obtained quite easily ($S/N > 25$). However, because lifetimes in the $X^3\Sigma$ state are much longer than in the $B^3\Pi$ state, molecular flow out of the detection region dominated any collision dynamical effects.

First, consider the pumping rate for the (20,0) transition at 560 nm. The fluorescence lifetime is $0.66 \mu\text{s}$.³³ Using the relations $A=\tau^{-1}$ and

$$B_{12}^I = \frac{c^3}{8\pi h f^3} A \quad (6-1)$$

we obtain a value for the Einstein B coefficient for I_2 $B^3\Pi \leftarrow X^3\Sigma$ vibronic transitions, for light intensity in $\text{erg s}^{-1} \text{cm}^{-2}$:

$$B^I = 5.3 \times 10^7 \text{sec g}^{-1}$$

Typically, with the second harmonic of the Nd:YAG laser pumping two dye lasers, 10 ns pulses of 1 mJ/pulse and $\Delta\nu=1 \text{ cm}^{-1}$ are obtained. The pump rate $k_{I_2}^{\text{pump}} = BI/\Delta\nu$. For these parameters $k_{I_2}^{\text{pump}} = 7.1 \times 10^{11} \text{ s}^{-1}$, five orders of magnitude faster than the spontaneous fluorescence rate. Therefore, the pump transition is saturated, and 50% of the population is moved.

The stimulated emission rate, or $k_{I_2}^{\text{dump}}$ is obtained by correcting for Franck-Condon factors³⁴ and transition frequencies. For dumping into $v''=4$ at 586 nm, the rate is $9 \times 10^{11} \text{ s}^{-1}$. Therefore, this transition is also saturated. Thus, 25% of the initial population in the ground state is moved into the selected target vibrational level.

Only one rotational level may be accessed with this narrow-band laser. The laser is tuned to transitions from J''_{max} . At $X/D=5$, $T=12\text{K}$, and the rotational degrees of freedom have not yet frozen out. The rotational constant of I_2 is $.04 \text{ cm}^{-1}$,³⁵ resulting in $J_{\text{max}} = 10$. $\theta_{\text{rot}} = .054\text{K}$, so $q_{\text{rot}} = 222$.³⁶ The fraction of molecules in $J''=10$ which are available for pumping, $P_{J_{\text{max}}}$, is 0.06.

The actual number density of I_2 molecules in the jet, under typical operating conditions (2% I_2 in Ar, $p_0 = 1 \text{ atm}$, $X/D=5$), ρ_{I_2} , is $10^{17} \text{ molec cm}^{-3}$. Using

$$\rho_{I_2, v''=4} = \rho_{I_2} \times P_{J_{\text{max}}} \times P_{\text{dump}} \times P_{\text{pump}} \quad (6-2)$$

we find the population of molecules in the target vibrational levels to be:

$$\rho_{I_2, v''=4} = 3 \times 10^{13} \text{ molec cm}^{-3}$$

The corresponding parameters for NO $\beta(7,0)$ are $A = 2.5 \mu\text{s}$,³⁷ $B^I=5.3 \times 10^5 \text{ sec g}^{-1}$, and the laser pulses are 10 ns long, with about $100 \mu\text{J/pulse}$, $\Delta\nu = 100 \text{ cm}^{-1}$. The pulse energy is lower than one would expect because of the difficulties of shaping and steering the excimer beam. Following an analogous calculation to that above for I_2 , we determine that the pumping rate for the

NO $\beta(7,0)$ transition is $1.7 \times 10^6 \text{ s}^{-1}$. This must be compared to the inverse of the zero pressure lifetime (including spontaneous fluorescence and predissociation) of $0.331 \mu\text{s}$,³⁰ giving a rate of $3 \times 10^6 \text{ s}^{-1}$. Since these rates are of the same order of magnitude, we must delve further to determine the actual fraction of molecules pumped under these conditions.

Toward this end, we can consider this as a three-level system, as shown in Figure 6-1. The rate equations for this system have been solved.³⁸ Including the simplification that $k_1 = k_{-1}$ [$B_{01} = B_{10}$], the number densities in all three levels are described by the following equations:

$$N_0 = \frac{m_2 - k_1}{m_2 - m_1} e^{-m_1 t} + \frac{k_1 - m_1}{m_2 - m_1} e^{-m_2 t} \quad (6-3a)$$

$$N_1 = \frac{k_1}{m_2 - m_1} \{e^{-m_1 t} - e^{-m_2 t}\} \quad (6-3b)$$

$$N_{\text{out}} = 1 + \frac{m_1}{m_2 - m_1} e^{-m_2 t} - \frac{m_2}{m_2 - m_1} e^{-m_1 t} \quad (6-3c)$$

where:

$$m_1 = 1/2[(2k_1 + k_2) - (4k_1^2 + k_2^2)^{1/2}]$$

$$m_2 = 1/2[(2k_1 + k_2) + (4k_1^2 + k_2^2)^{1/2}]$$

$$m_2 - m_1 = (4k_1^2 + k_2^2)^{1/2}$$

Figure 6-2 shows the results of these calculations. The lower plot is for the more general case, indicating that the pumping rate must be approximately two orders of magnitude greater than the rate of removal from the Rabi cycle in order to ensure saturation. The upper plot is for this case, with parameters particular to the Lumonics Excimer laser (1 mm² spot size, $\Delta\nu = 100 \text{ cm}^{-1}$, and the laser pulse is approximated by a 10 ns square pulse). From this we see that, with 100 $\mu\text{J}/\text{pulse}$, only about 1% of the population is moved into $B^2\Pi$ ($v'=7$).

Now consider the "dump" transition. k_{dump} may be obtained by correcting k_{pump} for Franck-Condon factors,³⁹ transition frequency, and laser power, in the same way as was done for I_2 above. The BBDL delivers about 300 $\mu\text{J}/\text{pulse}$, which gives a dump rate for the $\beta(7,23)$ transition at 610 nm as $k_{\text{dump}} = .84 \times 10^6 \text{ s}^{-1}$. Approximately

$$\int dt \sim \Delta t \text{ and } \int b_{23}(\omega - \omega_0) I_{\omega}(\omega - \omega_0) d\omega \sim k_{\text{dump}}$$

and using the expression from Kittrel, et al.:²²

$$n_2(\omega, \tau) = (1/2)n_2(\omega, 0) \times [1 + \exp(-2k_{\text{dump}}\Delta t)] \quad (6-4)$$

$$\text{then: } n_2(\omega = 10\text{ns}) = 0.92 n_2(\omega, \tau)$$

and only 8% of the population is moved from $B(v'=7)$ into the target vibrational state in X.

We follow a similar calculation to that above to determine the populations in the relevant rotational states. The spectroscopic constants are found in Huber and Herzberg.³⁵ If the $^{14}\text{N}^{16}\text{O}$ is used, $J=25-28$ may be pumped. The total fraction in these states is about .012. These high rotational levels are pre-dissociative, giving rise to higher oxides of nitrogen in recombination reactions. In order to freeze out these impurities, the sample must be held over a liquid nitrogen trap. NO has a vapor pressure of about 100 mTorr at 77K.⁴⁰ At 100 MTorr, $\rho_{\text{NO}} = 3.5 \times 10^{15} \text{ molec cm}^{-3}$, and

$$^{14}\text{N}^{16}\text{O}: \rho_{v''=23} = 3.5 \times 10^{10} \text{ molec cm}^{-3}$$

The isotope $^{15}\text{N}^{18}\text{O}$ helps somewhat, giving access to $J'' = 15-18$, so

$$^{15}\text{N}^{18}\text{O}: \rho_{v''=23} = 2.1 \times 10^{11} \text{ molec cm}^{-3}$$

The probe and detection transitions for both experiments are similar in that they have large Franck-Condon factors, the lasers used are of similar bandwidth and power, and that a band-pass filter is used to separate the desired triple resonance fluorescence from the fluorescence due to the pump only step. However, we can see that the number density in the $^{14}\text{N}^{16}\text{O}$ target level, even in the best case, is a factor of 10^3 lower than that for I_2 SEP work. Empirically, we obtained a signal-to-noise ratio in the I_2 work of about 25. Scaling this to the NO work, we would expect a signal-to-noise ratio of .025. Even with the heavy isotope, S/N is still below 1, rendering it nearly impossible to find the triple resonance signal at all.

6.2.2 SEP of NO using a Two-Photon Pump

Given the limitations of using the ArF excimer laser as a pump source, we must consider available tunable, narrow-band sources for exciting NO. The $\gamma(0,0)$ transition at 226 nm is well known, and has been the basis of a number of experiments. However, the γ -bands follow a $\Delta v=1$ propensity rule, due to the similarity between the $X(^2\Pi)$ and $A(^2\Sigma)$ potentials. As a result, $A(^2\Sigma)(v'=0)$ has small Franck-Condon overlap with any high vibrational levels of $X(^2\Pi)$, limiting our ability to populate any of these levels of interest. Higher vibrational levels of the available excited electronic states (A, B, and C) have more advantageous Franck-Condon overlaps, but transitions into these states are 205 nm and below, beyond the range of available doubling crystals. Tunable, narrow-band VUV radiation has been generated by third-harmonic generation in a strontium-xenon mixtures,⁴¹ by four-wave mixing in mercury vapor,⁴² or by frequency-doubling and Raman shifting the output of a single dye laser.⁴³ The pulse energies obtained with these systems are on the order of several μJ , which is sufficient for one-laser excitation experiments, but is not enough to actually significantly populate the upper state. One may suggest an excimer laser in which one mode is selected by prisms in an oscillator cavity, and is amplified in another cavity. This would give high-power, narrow bandwidth VUV radiation, and has been successfully applied to KrF output near 248 nm. However, experience⁴⁴ has shown that extension of this to ArF output near 193 nm is unreliable at best. Recently, Sum Frequency Generation in barium borate (BBO) nonlinear crystals has been reported. In this, 248.5 nm (obtained by frequency doubling the output of a dye laser, *not* from a KrF excimer laser) and 800 nm light are mixed to give 10-100 $\mu\text{J}/\text{pulse}$ near 191 nm.⁴⁵ This may be promising, despite the limitation that the full triple resonance scheme would then require four dye lasers, three of which are pumped by the same source.

While generating high-power VUV radiation remains elusive, progress has been made in lasers operating in the visible and near UV. Excimer-pumped dye lasers, delivering pulse energies of tens of mJ, have introduced the possibility of nearly saturating a *two*-photon transition. As will be shown below, pumping transitions at the two-photon equivalent of VUV frequencies, followed

by dumping with one UV photon, is an efficient method of generating significant populations in selected vibrational levels of the ground electronic state of NO.

As before, let us calculate the population in the target vibrational level we may obtain using this method. Several values for the two-photon absorption cross-section for the $\gamma(0,0)$ [$R_{22} + S_{12}$ ($J''=9.5$)] transition, integrated over the Doppler line-width of 0.1 cm^{-1} , have been reported in the literature.⁴⁶⁻⁴⁹ These values range from 3×10^{-48} to $3 \times 10^{-49} \text{ cm}^4 \text{ sec}$. In this order-of-magnitude calculation, let us simply use $10^{-48} \text{ cm}^4 \text{ sec}$. So, for a laser pulse with a band-width equal to the Doppler width, the rate of pumping is:

$$k_{\text{pump}} = \frac{2\pi\sigma I^2}{(h\nu)^2} \quad (6-5)$$

If we pump the $\gamma(3,0)$ transition near 391 nm under typical experimental conditions (0.05 mm^2 spot size, etalon-narrowed bandwidth of $\Delta\nu=0.04 \text{ cm}^{-1}$), we obtain a pumping rate per mJ of laser pulse energy:

$$k_{\text{pump}}/\text{mJ} = 2.32 \times 10^6 \text{ mJ}^{-2}\text{sec}^{-1}.$$

This vibrational level is not above the dissociation limit, so the only method of removal from the Rabi cycle is via spontaneous fluorescence. The fluorescence lifetime is 200 ns.⁵⁰⁻⁵³ which gives k_{out} equal to $5 \times 10^6 \text{ sec}^{-1}$. Using the same method as depicted in Figure 6-1, with the exception that k_1 and k_{-1} are two-photon processes, we may calculate the fraction in each of the levels after a 10 ns pulse, as a function of laser pulse energy. The results of this calculation are given in Figure 6-3.

6.3 Experimental

6.3.1. Two-Photon Pumping

This calculation of two-photon pumping efficiency was experimentally tested. The etalon-narrowed output of a XeCl excimer-pumped dye laser (Lambda Physik EMG201/FL3002) is focussed into a cell containing 100 mTorr neat NO. Fluorescence is filtered from scattered laser

light (Corion) and imaged onto a photomultiplier tube. The laser is pressure scanned with nitrogen, and a small portion of the two-photon laser excitation spectrum is given in Figure 6-4 with assignments after Zacharias, et al.⁵² The laser is then set on the $P_{11}(9\ 1/2)$ transition. A back reflection impinging on a photodiode is used to measure relative laser energy, and the beam is dumped into a joule meter (Laser Precision) for absolute laser energy measurements. The laser is attenuated by a series of glass microscopy cover slips (each attenuates by about 10%), and the pulse energy and fluorescence intensity are simultaneously measured over a wide range of energies. The output of the PMT and the photodiode are integrated (EG&G/PAR) and collected on a laboratory computer (IBM PC).

The data are then transferred to a mainframe computer (VAX) for analysis. Laser pulse energy is scaled to the absolute values given by the joule meter. The maximum signal intensity is then scaled to the level given by the calculation. As shown in Figure 6-5, there is good agreement between experiment and the functional form of pumping efficiency versus pulse energy, even with this simple scaling scheme, throughout the range of energies obtained. Therefore, we may be confident of the veracity of the scheme depicted in Figure 6-3.

6.3.2. "Two minus One" SEP

With reasonably efficient two-photon pumping of the $\gamma(3,0)$ $P_{11}(9\ 1/2)$ transition, we may now include the second step, the dump of population into the target vibrational level of $X(2\Pi)$ state. For this, two cells containing 400 mTorr NO (1.4×10^{16} molecules cm^{-3}) are used. The pump beam is focussed into both (400 mm focal length), and the LIF signals from these are differentially amplified and balanced to give a zero baseline. In order to maximize the pumping efficiency, the pump beam was not split, but rather focussed consecutively into these two cells. With a typical pump energy of 1.0 mJ, our calculation above indicates that approximately 2% of the molecules in the focal region are pumped. The dump laser output (Lambda Physik EMG200/FL2002, operating with Coumarin 460) is frequency doubled to give 200 μJ pulses near 228 nm., the $\gamma(3,4)$ band. This is optically delayed by 10 ns, then is loosely focussed (600 mm focal length) and directed colinear and counter propagating to the pump beam through one of the

cells. It is prevented from entering the other cell with a glass microscope slide. The output of the differential amplifier is integrated and averaged as before. As the dump laser is tuned into resonance with allowed rovibronic transitions in the $\gamma(3,4)$ band, we observe the dips in the differential fluorescence signal, corresponding to depletion of the $A(^2\Sigma)(v'=3, J=8\ 1/2)$ rovibronic level population. A schematic of the relevant levels and transitions is given in Figure 6-6, and the experimental fluorescence dip spectrum in Figure 6-7. These dips correspond to a depletion of about 20% of the population in the upper state. According to Equation 6-4 above, this transition should be saturated under these conditions, which would give 50% depletion. The discrepancy is most probably because the dump beam is focussed more tightly than is optimal. If the dump beam does not fully cover the volume defined by the pump beam, it will not spatially access all the initially pumped molecules.

The fraction of population in the initial $v''=0, J=9\ 1/2$ is 7.5% at 300K. Thus, we find the number density of molecules in our target vibrational level to be:

$$\begin{aligned}\rho_{\text{NO}, v''=4} &= \rho_{\text{NO}} \times P_{J''} \times P_{\text{pump}} \times P_{\text{dump}} \\ &= 2.2 \times 10^{12} \text{ molecules cm}^{-3}\end{aligned}$$

6.4 Discussion

These experiments indicate that 2-1 SEP is an effective way to populate single vibrational levels in the ground electronic state of NO. It is desirable to distribute the XeCl excimer pump beam between the pump and dump lasers, such that the efficiency for each process is optimized. This was not possible in the above experiments, due to laboratory constraints. Despite this, we already achieved an order of magnitude improvement in our stimulated emission pumping efficiency over the ArF-pumping approach. Let us assume that we have divided the XeCl excimer laser so that it gives us 6 mJ/pulse near 390 nm, to be used for the two-photon pump. Our calculations then indicate that the transition is nearly saturated and 40% of the molecules may be pumped. This will not only increase the number density of the molecules pumped, but will also improve the signal-to-noise ratio in the fluorescence dip spectrum. Near saturation, signal levels are not as sensitive to fluctuations in laser power.

By insuring enough power for the pump step, there is not much of the XeCl excimer pump beam left for the dump laser. Fortunately, the one-photon γ -band transitions may be saturated with only a few tens of μJ of pulse energy. As indicated above, the $A^2\Sigma(v)$ have lifetimes on the order of 200 ns, which gives rise to an Einstein B coefficient of $5 \times 10^6 \text{ s g}^{-1}$. For 50 μJ pulses, focussed to 0.5.5 mm² spot, and with a bandwidth of 0.2 cm⁻¹, we obtain k_{dump} of $7.5 \times 10^9 \text{ sec}^{-1}$. We refer again to the equation given by Kittrell, et al.,²² which gives us a dumping efficiency of 50%.

The initially pumped state in this double resonance process is $A^2\Sigma(v'=3, J'=8 \frac{1}{2})$. Unlike the high rotational states of $B^2\Pi(v'=7)$, dissociation is not a problem for these low rotational levels of $A(v'=3)$. Therefore, it is not necessary to maintain the sample over a liquid nitrogen trap to freeze out recombination products, so higher pressures may be used. At a modes pressure of 1 Torr ($3.5 \times 10^{16} \text{ molecules cm}^{-3}$), we obtain for the number density of molecules in the target vibrational level of the ground electronic state:

$$\rho_{\text{NO}, v''=4} = 5 \times 10^{14} \text{ molecules cm}^{-3}$$

Although this number is accurate only to the order of magnitude, it is obvious that the molecular densities in the target vibrational level may be obtained with this method which are significantly higher than those which may be expected for pumping with a 193 nm ArF excimer laser. Also, a wide variety of v'' levels may be populated by " $2 \text{ minus } 1$ " stimulated emission pumping. For example, $A^2\Sigma(v'=4)$ has good Franck-Condon overlap with $X^2\Pi(v''=3,5,6,11, \text{ and } 12)$. Nearly all other v'' levels of interest may be accessed via $v' = 2$ and/or 3. State-specific rates for collisional vibrational relaxation of this important atmospheric molecule may now be addressed. Recently, stimulated-emission pumping of NO via the B state has been demonstrated using a tunable, narrowband argon fluoride laser⁵⁴, in which the laser output could be tuned controllably across the excimer transition gain curve. This also affords the possibility of collisional relaxation measurements in high vibrational measurements of NO.

Section 6 References

1. Green, B.D.; Calendoncia, G.E.; Murphy, R.E.; Robert, F.X., *J. Chem. Phys.* **76**, 2441 (1982).
2. Deutsch, T.F., *Appl. Phys. Lett.* **9**, 295 (1966).
3. Burrows, M.D.; Baughcum, S.L.; Oldenberg, R.C., *Appl. Phys. Lett.* **46**, 22 (1985).
4. Stephenson, J.C., *J. Chem. Phys.* **60**, 4289 (1974).
5. Kosanetzky, J.; List, U.; Urban, W.; Vormann, H.; Fink, E.H., *Chem. Phys.* **50**, 361 (1980).
6. Nachshon, Y.; Coleman, P.D., *J. Chem. Phys.* **61**, 2520 (1974).
7. Murphy, R.E.; Lee, E.T.P.; Hart, A.M., *J. Chem. Phys.* **63**, 2919 (1975).
8. Horiguchi, H.; Tsuchiya, S., *J. Chem. Phys.* **70**, 763 (1979).
9. Horiguchi, H.; Tsuchiya, S., *J. Appl. Phys.* **18**, 1207 (1979).
10. Yardley, J.T., *Introduction to Molecular Energy Transfer* (Academic Press, Inc., New York, 1980).
11. Nikitin, E.E., *Opt. Spectrosc.* **9**, 8 (1960).
12. Wray, K.L., *J. Chem. Phys.* **36**, 2597 (1962).
13. Dillon, T.A.; Stephenson, J.C., *J. Chem. Phys.* **60**, 4286 (1974).
14. Schwartz, R.N.; Slawsky, Z.I.; Herzfeld, K.F., *J. Chem. Phys.* **20**, 1591 (1952).
15. Bergman, R.C.; Williams, M.J.; Rich, J.W., *Chem. Phys.* **66**, 357 (1982).
16. Rawlins, W.T.; Murphy, H.C.; Caledonia, G.E.; Kennealy, J.P.; Robert, F.X.; Corman, A.; Armstrong, R.A., *Appl. Opt.* **23**, 3316 (1984).
17. Armstrong, R.A.; Kennealy, J.P.; Robert, F.X.; Corman, A.; Rawlins, W.T.; Piper, L.G.; Caledonia, G.E.; Green, B.D.; Murphy, H.C.; Steinfeld, J.I.; Stachnik, R.; Adler-Golden, S.M., "Atmospheric Chemiluminescence: COCHISE and Related Experiments", AFGL-TR-82-0305 Technical Report, (1982). ADA130546.
18. Kennealy, J.P.; Del Greco, F.P.; Caledonia, G.E.; Green, B.D., *J. Chem. Phys.* **69**, 1574 (1978).
19. Miller, S.M.; Lurie, J.B.; Armstrong, R.A.; Winkler, I.; Steinfeld, J.I.; Rawlins, W.T.; Gelb, A.; Piper, L.; Caledonia, G.E.; Nebolsine, P.; Weyl, G.; Green, B.D., "Spectroscopic, Kinetic, and Dynamic Experiments on Atmospheric Species", AFGL-TR-85-0077 Technical Report, (1985). ADA162691.

20. Winkler, I.C.; Stachnik, R.A.; Steinfeld, J.I.; Miller, S.M., *J. Chem. Phys.* **85**, 890 (1986).
21. Sudbo, Aa.S., Loy, M.M.T., *Chem. Phys. Lett.* **82**, 135 (1981).
22. Kittrell, C.; Abramson, E.; Kinsey, J.L.; McDonald, S.A.; Reisner, D.E.; Field, R.W., *J. Chem. Phys.* **75**, 2056 (1981).
23. Hamilton, C.E.; Kinsey, J.L.; Field, R.W., *Ann. Rev. Phys. Chem.* **37**, 493 (1986).
24. Dai, H.L.; Korpa, C.L.; Kinsey, J.L.; Field, R.W., *J. Chem. Phys.* **82**, 1688 (1985).
25. Vaccaro, P.P.H.; Redington, R.L.; Schmidt, J.; Kinsey, J.L.; Field, R.W., *J. Chem. Phys.* **82**, 5755 (1985).
26. Lawrance, W.D.; Knight, A.E.W., *J. Chem. Phys.* **77**, (1982).
27. Lawrance, W.D.; Knight, A.E.W., *J. Chem. Phys.* **79**, 6030 (1983).
28. Kable, S.H.; Thoman, J.W., Jr.; Beames, S.; Knight, A.E.W., *J. Phys. Chem.* **91**, 1004 (1987).
29. Thoman, J.W., Jr.; Kable, S.H.; Rock, A.B.; Knight, A.E.W., *J. Chem. Phys.* **85**, 6234 (1986).
30. Shibuya, K.; Stuhl, F., *Chem. Phys.* **79**, 367 (1983).
31. Harradine, D., Ph.D. Thesis, Massachusetts Institute of Technology (1984).
32. Foy, B.R., Ph.D. Thesis, Massachusetts Institute of Technology (1988).
33. Steinfeld, J.I., *J. Chem. Phys.* **44**, 2740 (1966).
34. Tellinghuisen, J., *J. Quant. Spec. Rad. Transf.* **19**, 149 (1978).
35. Huber, K.P.; Herzberg, G., *Molecular Structure and Molecular Spectra. Vol. 4, Constants of Diatomic Molecules* (VanNostrand, Princeton, N.J., 1979).
36. McQuarrie, D.A., *Statistical Mechanics* (Harper and Row, New York, 1976).
37. Brzozowski, J.; Erman, P.; Lyyra, M, *Phys. Scripta* **14**, 290 (1976).
38. Lowry, T.M.; John, W.T., *J. Chem. Soc. London* **97**, 2634 (1910).
39. Nicholls, R.W., *J. Res. Nat. Bur. Sd., A* **68A**, 535 (1964).
40. Hughes, E., *J. Am. Chem. Soc.* **35**, 1531 (1961).
41. Scheingraber, H.; Vidal, C.R., *J. Opt. Soc. Am. B* **2**, 343 (1985).
42. Tsukiyama, K.; Munakata, T.; Tsukakoshi, M.; Kasuya, T, *Chem. Phys. Lett.* **137**, 315 (1987).
43. Rottke, H.; Zacharias, H., *J. Chem. Phys.* **83**, 4831 (1985).

44. Hamilton, C.E., private communication.
45. Mückenheim, W.; Lokai, P.; Burghardt, B.; Basting, D. Appl. Phys. B, submitted.
46. McKenzie, R.L.; Gross, K.P., Appl. Opt. **20**, 2153 (1982).
47. Gross, K.P., McKenzie, R.L., J. Chem. Phys. **76**, 5260 (1982).
48. Hochstrasser, R.J., Meredith, G.R.; Trommsdorf, H.P., Chem. Phys. Lett. **53**, 423 (1978).
49. Burris, J.; McGee, T.J.; McIlrath, T.J., Chem. Phys. Lett. **101**, 588 (1983).
50. Callear, A.B.; Pilling, M.J., Trans. Faraday Soc. **66**, 1618 (1970).
51. Brzozowski, J.; Elander, N.; Erman, P., Phys.Scripta **9**, 99 (1974).
52. Zacharias, J.; Halpern, J.B.; Welge, K.H., Chem. Phys. Lett. **43**, 41 (1976).
53. Smith, A.M.; Read, F.H., J. Phys. **B11**, 3263 (1978).
54. X. Yang and A.M. Wodtke (to be published).

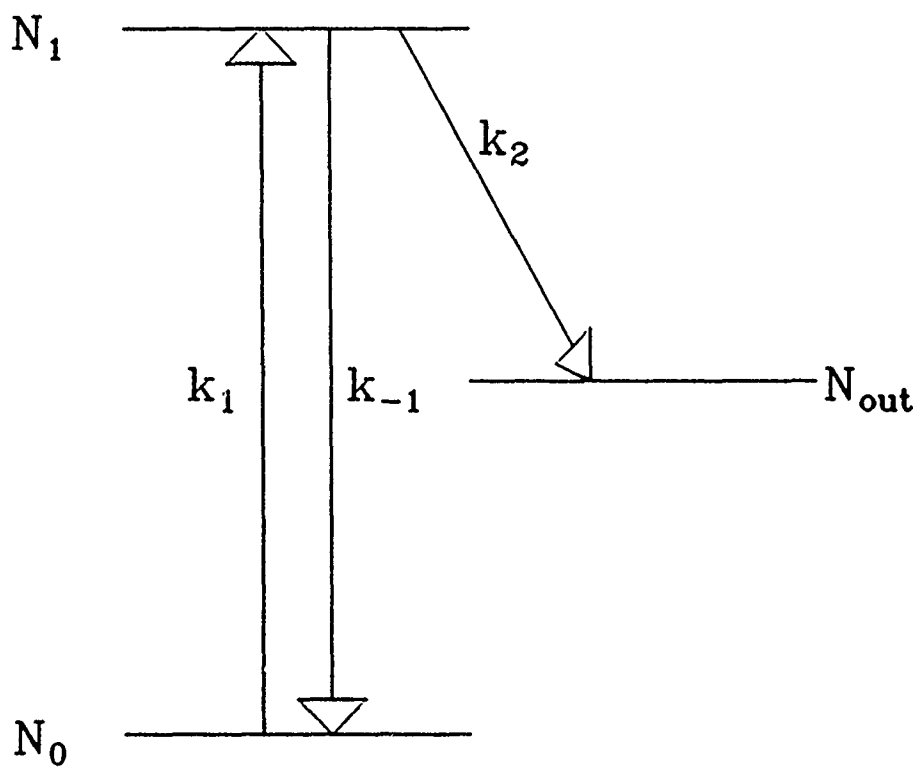


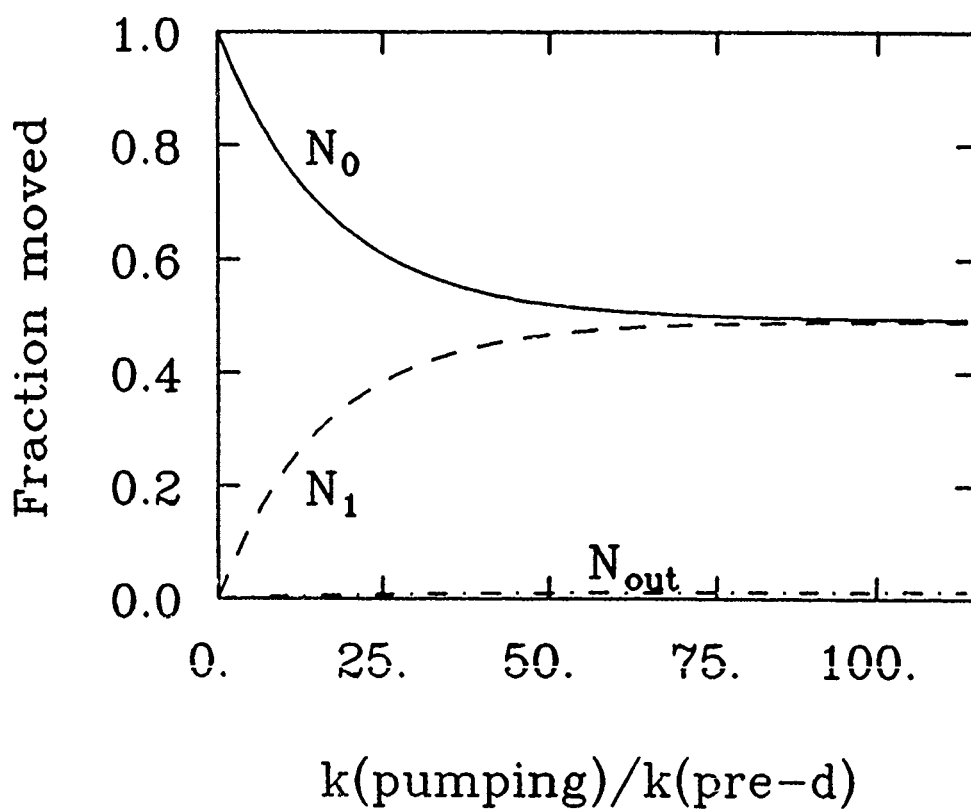
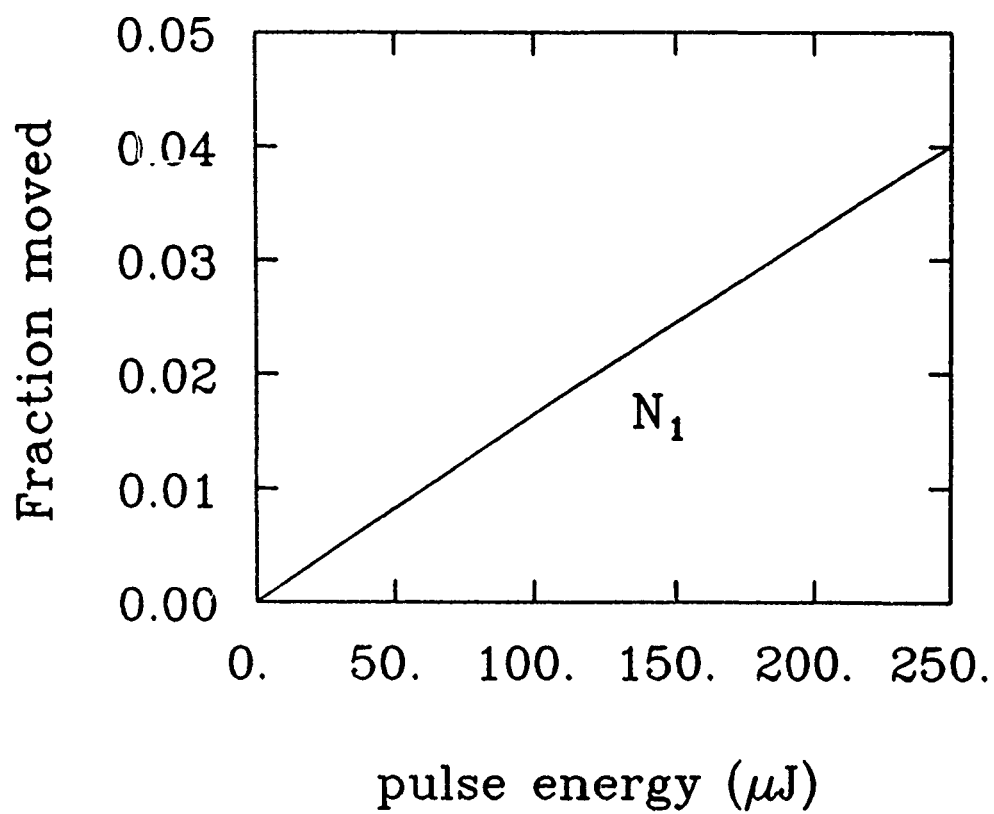
Figure 6-1 . Three-Level Model

Used to calculate the fraction of molecules pumped under sub-saturation conditions.

Figure 6-2 . 193 nm pumping efficiency under sub-saturation conditions

Upper Trace: Specific case, showing fraction in the upper level after a 10 ns pulse vs. pulse energy, using parameters particular to the Lumonics Excimer Laser (see text).

Lower Trace: General case, showing fraction in each level after a 10 ns pulse vs. ratio of rate into over rate out of the upper state, k_1/k_{out} .



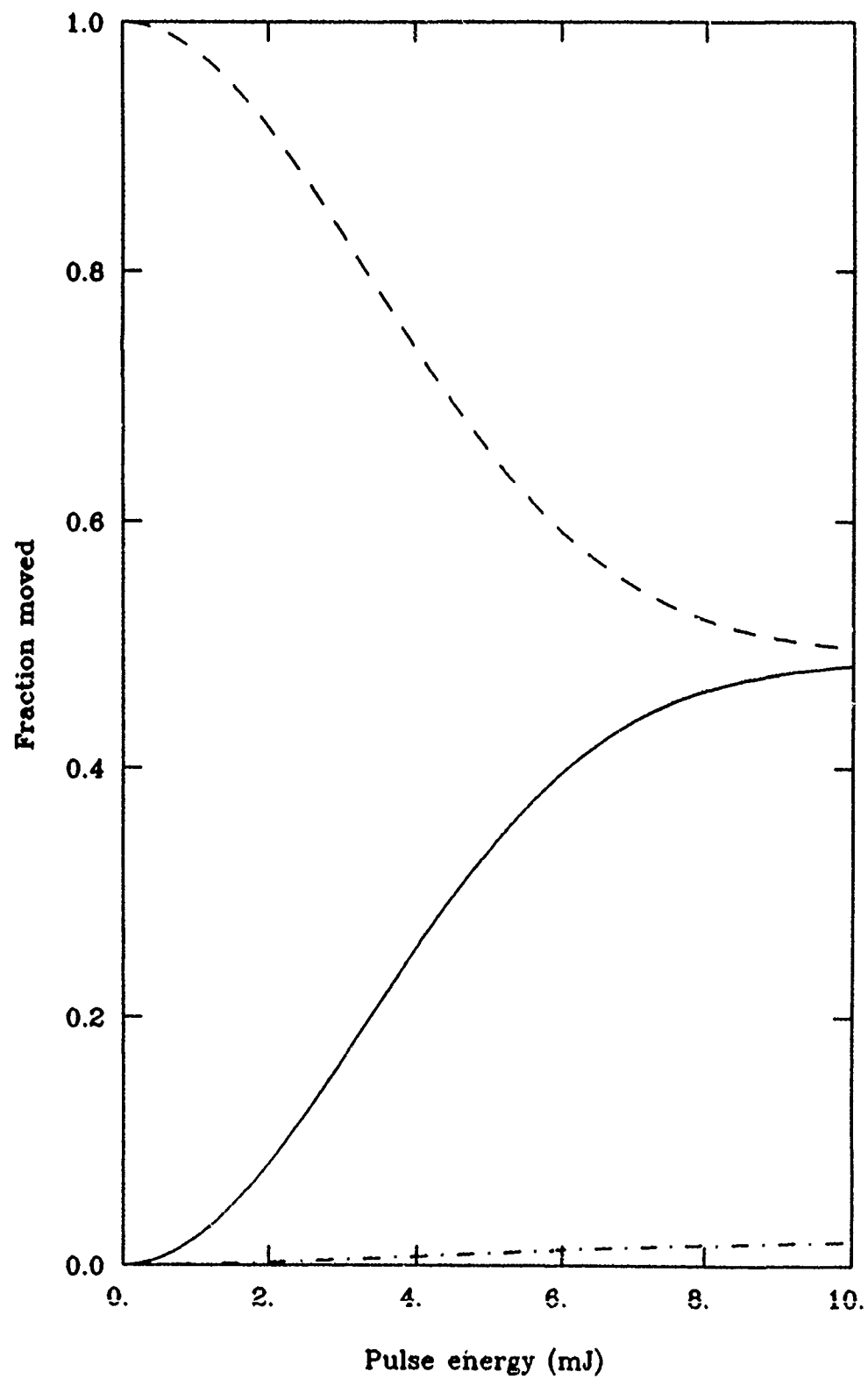


Figure 6-3. Two-photon pumping efficiency under sub-saturation conditions
Fraction of molecules in each of the levels shown in Figure 1-1
Dashed line: N_0
Solid line: N_1
Dot-Dash line: N_{out}

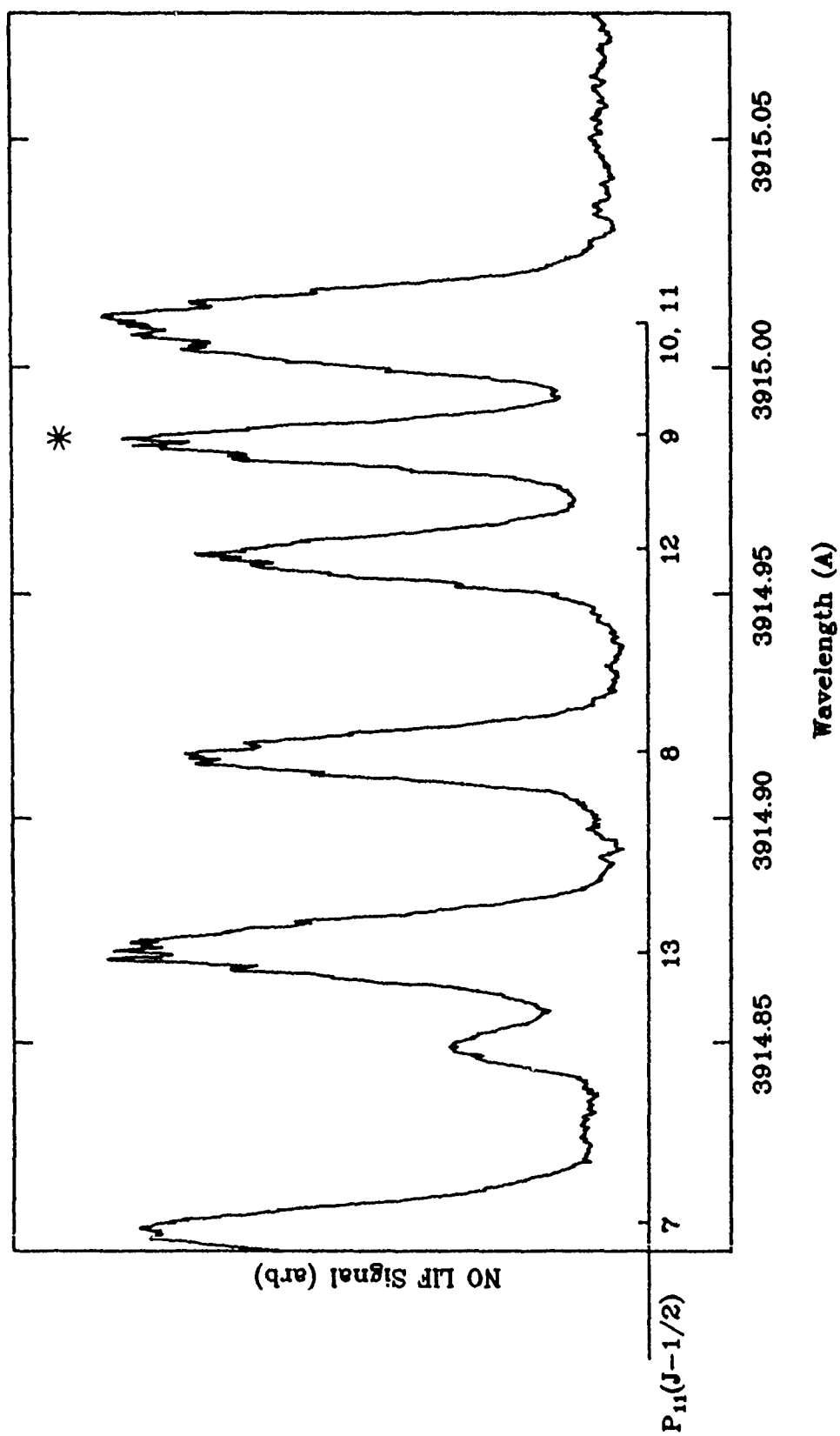


Figure 6-4. NO $\gamma(3,0)$ Two-Photon Excitation Spectrum
Assignments are after Zacharias, et. al.⁵²

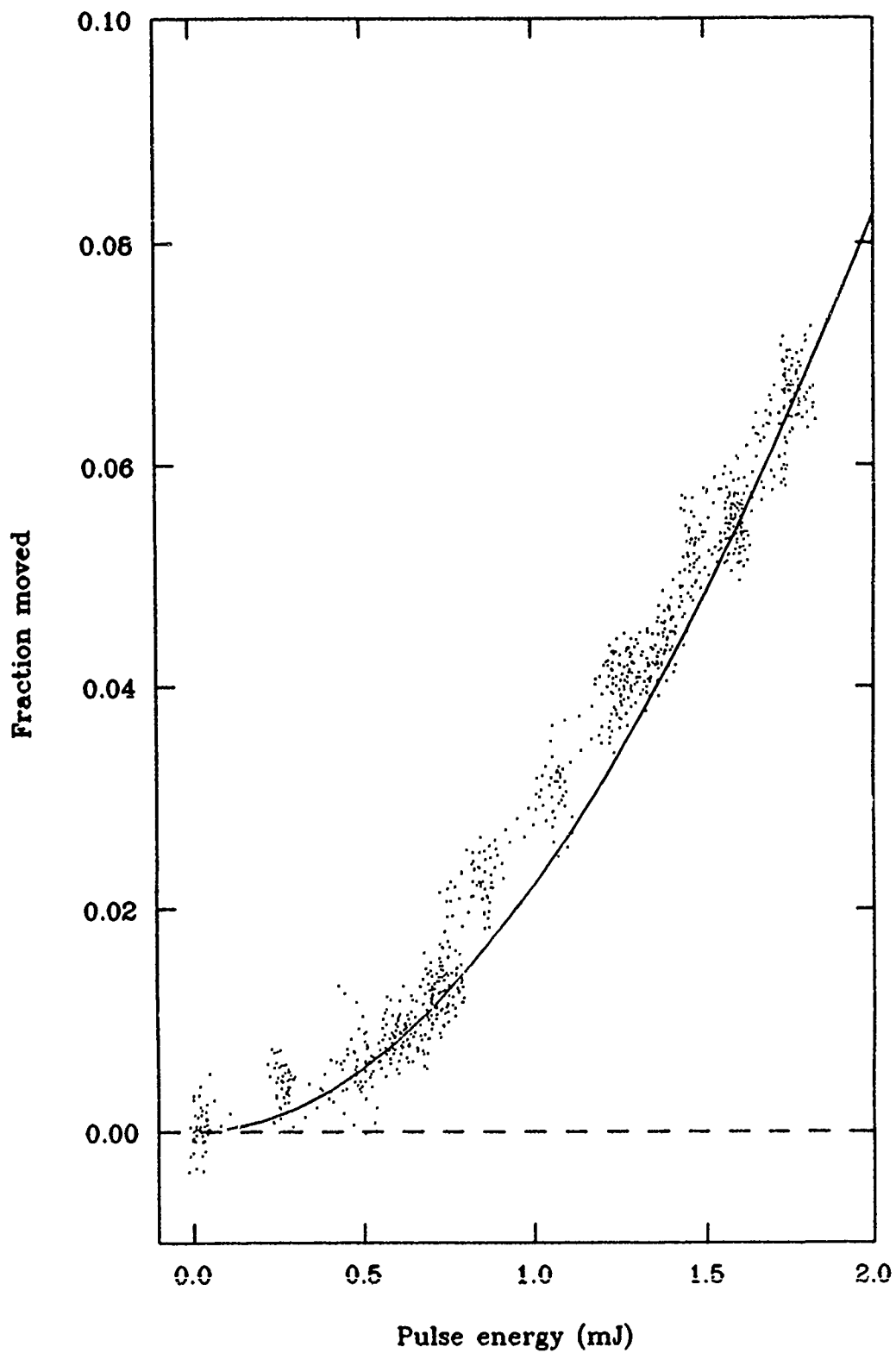


Figure 6-5. Experimental and calculated two-photon pumping efficiency

Dots: Experimental points

Solid line: Calculated efficiency

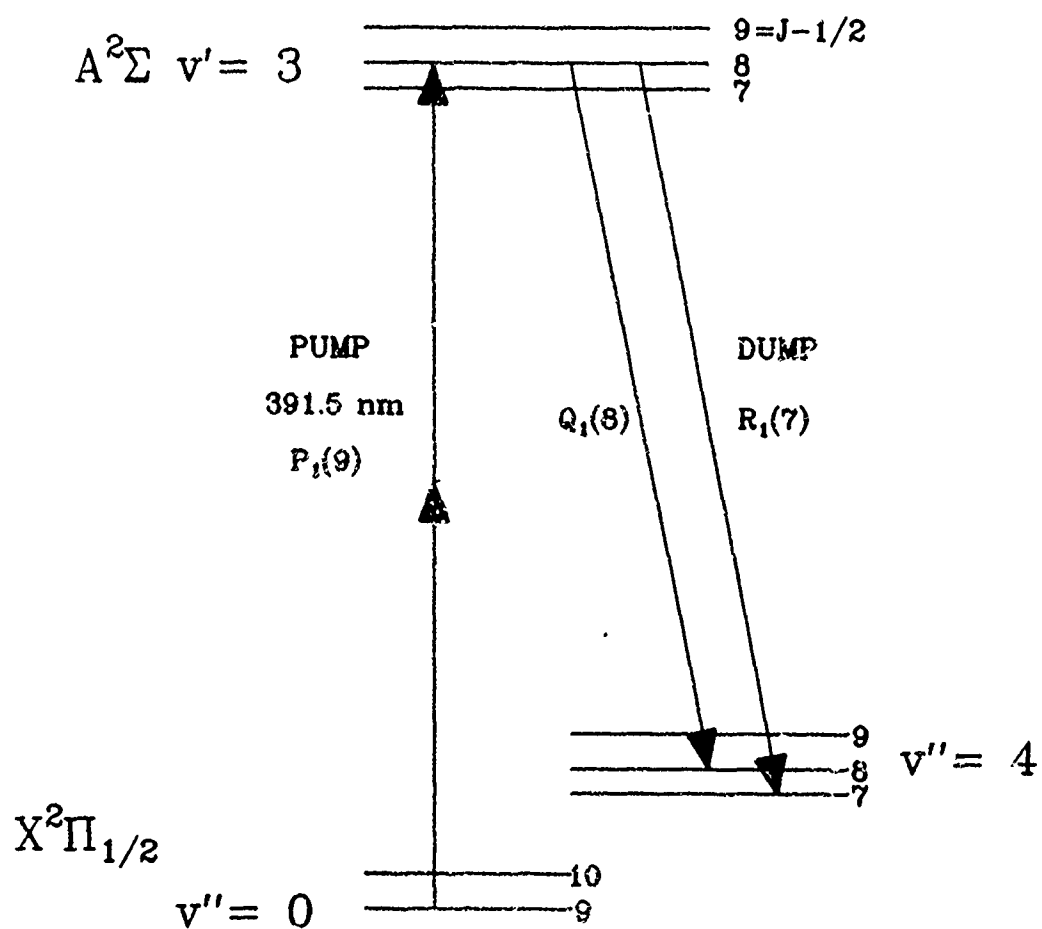


Figure 6-6. Levels and Transitions in "2-1" SEP of NO

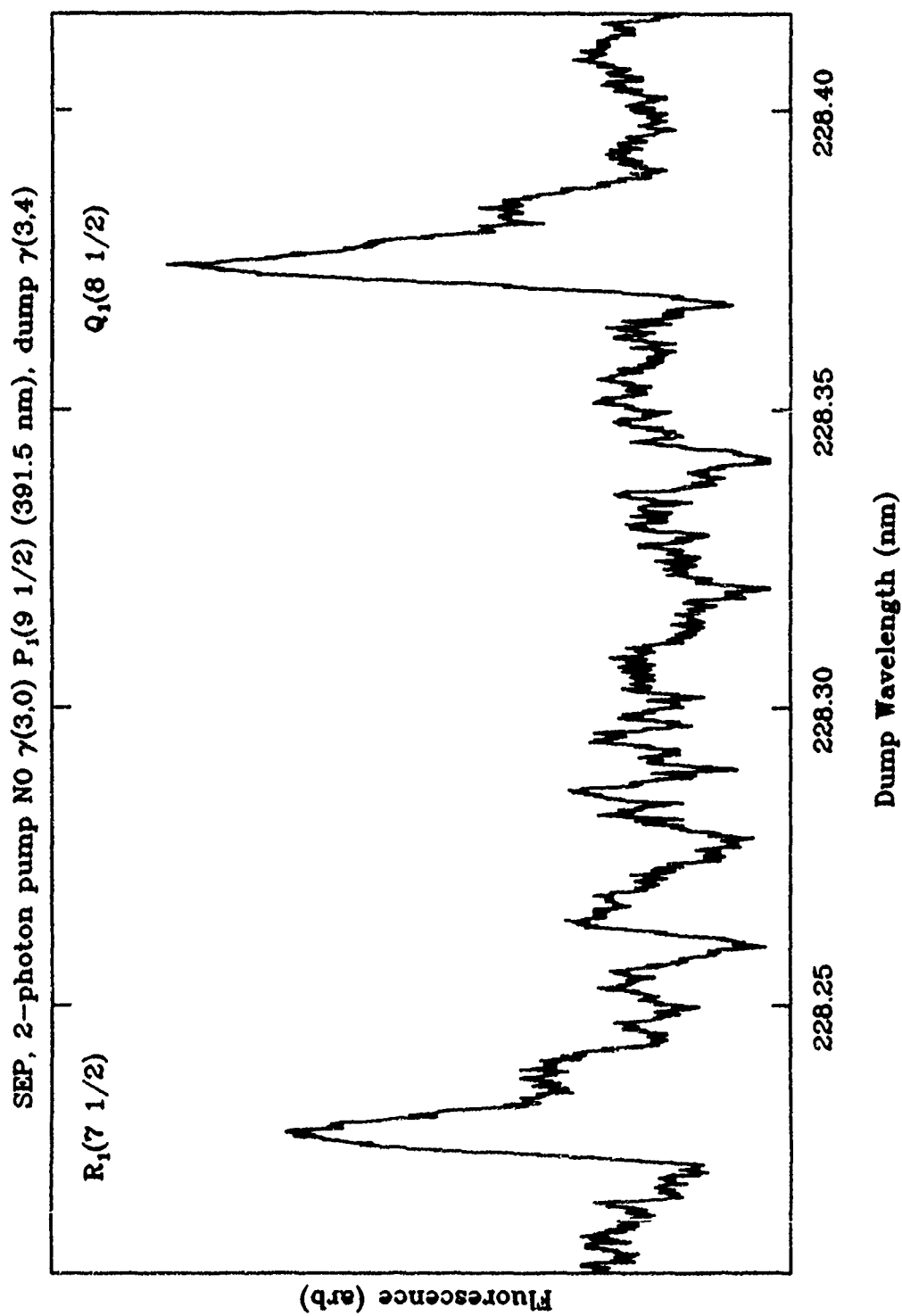


Figure 6-7. "2-1" Fluorescence Dip Spectrum of NO

$R_1(7\ 1/2)$ Transition: Observed, 228.23 ± 0.01 nm

Calculated, 228.232 nm

$Q_1(8\ 1/2)$ Transition: Observed, 228.37 ± 0.01 nm

Calculated, 228.374 nm

7.1 Recent Developments and Future Applications

7.1 REMPI Detection of $N_2(X^1\Sigma_g^+)$

While making measurements of $N(^4S)$ MPI signals, a number of molecular bands were apparent in the same spectral range. These bands were quenched only very slowly on addition of either O_2 or NO . They also became more prominent as the mole fraction of molecular nitrogen was increased. The band-head positions coincide with the reported band-head wavelengths¹ for the Lyman-Birge-Hopfield bands of N_2 ($a^1\Pi_g \rightarrow X^1\Sigma_g^+$). The single photon wavelengths of the observed transition band-heads, together with their assignments, are listed in Table 7.1.

The observed spectra for the (9,17) and (13,20) bands are shown in Fig. 7.1. The $N(^4S)$ quartet is visible to the red side of these bands. This N_2 transition is permitted only by magnetic dipole and electric quadrupole selection rules. This gives S and O electric quadrupole branches ($\Delta J = \pm 2$) and P, Q, and R electric quadrupole plus magnetic dipole branches ($\Delta J = \pm 1$). Work is currently under way to fit these spectra using the kinetic model described in Section 5. This will enable quantitative comparison of relative ground state populations to be made for high vibrational levels in the ground state of N_2 . MPI spectra of $N_2(X)$ have been reported previously using (3+1)^{2,3} and (2+2)^{4,5} excitation schemes. The spectra here are obtained using a (1+1) excitation scheme and might therefore be expected to provide a more sensitive detection method. A measurement of the power dependence of the (9,17) band-head was made and the results are shown in Fig. 7.2. The power dependence of the MPI signal varied between 1.6 and 1.2 over the laser power range investigated. This suggests that the ($a^1\Pi_g \rightarrow X^1\Sigma_g^+$) transition is becoming partially saturated.

We have been successful in detecting N_2 in highly vibrationally excited states ($v'' = 15$ to 21) in active nitrogen flows. It is to be expected that other vibrational levels will be accessible at longer wavelengths provided that sufficient energy is available to reach the ionization limit using only two photons, and that the Franck-Condon overlap¹ is favorable. Lower vibrational levels generally require progressively shorter laser wavelengths and are therefore not accessible using this scheme.

7.2. Identification of Atomic and Molecular Species Generated in Nitrogen Afterglows with SF₆

Attempts were made to enhance N-atom dissociation in N(²D)+O quenching experiments (Section 2) by flowing small amounts of SF₆ through the microwave discharge. While this successfully increased both the N(⁴S) and N(²D) concentrations, it also resulted in the appearance of atomic and molecular features in the spectral region of interest. The observed spectrum is shown in Fig. 7.3. The strong atomic line corresponds to the (1+1) MPI transition⁶



of atomic sulphur. The splitting of the upper J-level components is not resolved. The molecular spectrum corresponds to the (1+1) MPI $B^2\Sigma^+ \rightarrow X^2\Pi_{1/2}$ transition of NS⁷. The $X^2\Pi_{3/2}$ branch will be apparent some 220 cm⁻¹ to the red although this has not been confirmed experimentally. No other band positions are reported for this transition⁷.

7.3. FACELIF Modifications

A number of modifications to the FACELIF apparatus have been implemented in the light of some of the limitations encountered in the experiments described in the previous sections of this report. These improvements, together with their motivation, are discussed briefly here. The two main aspects of these modifications are, firstly, a substantially longer quartz flowtube and, secondly, a movable MPI detector.

The 30 cm pyrex flowtube has been replaced by 1.2 m length high grade quartz tubing of the same diameter. This has two distinct advantages over the previous arrangement. The first of these concerns [N] measurements for faster flows, made using NO titrations. As described in Sec. 2, in order to obtain accurate titration end-points, sufficient flow time must be allowed for the N + NO reaction to go to completion. The use of this longer flowtube will enable these titration measurements to be taken downstream of the MPI detector, thus extending the temporal range of the titration technique.

The longer flowtube arrangement also provides ample room for the installation of a spectrometer. A linear motion system has been purchased which, when installed, will allow the spectrometer to be accurately translated along the flowtube axis. The spectrometer will provide a useful additional diagnostic tool for analysing the temporal evolution of the afterglow.

The second major modification is the installation of a movable MPI detector. With the previous set-up, the grids remained fixed with the amplifier circuit attached directly to the feed-throughs. The new detector has the amplifier attached to the grids inside the flowtube. The whole assembly may be translated by means of a 1/4" stainless steel tube which also serves as a guide for the electrical connections.

The detector incorporates a three grid system which subtracts the background current in the absence of the laser pulse, thus effectively eliminating detection problems emanating from ions present in the flow. The laser beam is directed straight through the wall of the flowtube. Despite the lack of Brewster angle windows, the laser power is not significantly attenuated by its passage through the flowtube. MPI spectra have been successfully obtained using the new FACELIF configuration.

References

1. A. Lofthus and P.H. Krupenie, "The Spectrum of Molecular Nitrogen", J. Phys. Chem. Ref. Data **6**, 113 (1977).
2. S.T. Pratt, P.M. Dehmer and J.L. Dehmer, J. Chem. Phys. **80**, 1706 (1984).
3. S.T. Pratt, P.M. Dehmer and J.L. Dehmer, J. Chem. Phys. **81**, 3444 (1984).
4. K.L. Carleton, K.H. Welge and S.R. Leone, Chem. Phys. Letts. **115**, 492 (1985).
5. W.J. Marinelli and W.J. Kessler, PSI-TR-699 (1987).
6. S. Bashkin and J.O. Stoner, "Atomic Energy-levels and Grotrian Diagrams 2", North Holland Publishing Co., Amsterdam (1978).
7. N.A. Narasimham, K. Raghuveer and T.K. Balasubramanian, J. Mol. Spec. **54**, 160 (1975).

Table 7.1 Observed and calculated bandhead position for the $a^1\Pi_g \rightarrow X^1\Sigma_g^+$ transition in N_2 .

| <u>v'</u> | <u>v''</u> | <u>Wavelength/nm</u> | |
|------------------------|-------------------------|----------------------|-------------------|
| | | <u>Observed</u> | <u>Calculated</u> |
| 7 | 15 | 207.71 | 207.66 |
| 8 | 16 | 209.63 | 209.60 |
| 9 | 17 | 211.49 | 211.45 |
| 10 | 18 | 213.37 | 213.35 |
| 12 | 19 | 209.13 | 209.03 |
| 13 | 20 | 211.06 | 211.00 |
| 14 | 21 | 213.01 | 212.98 |

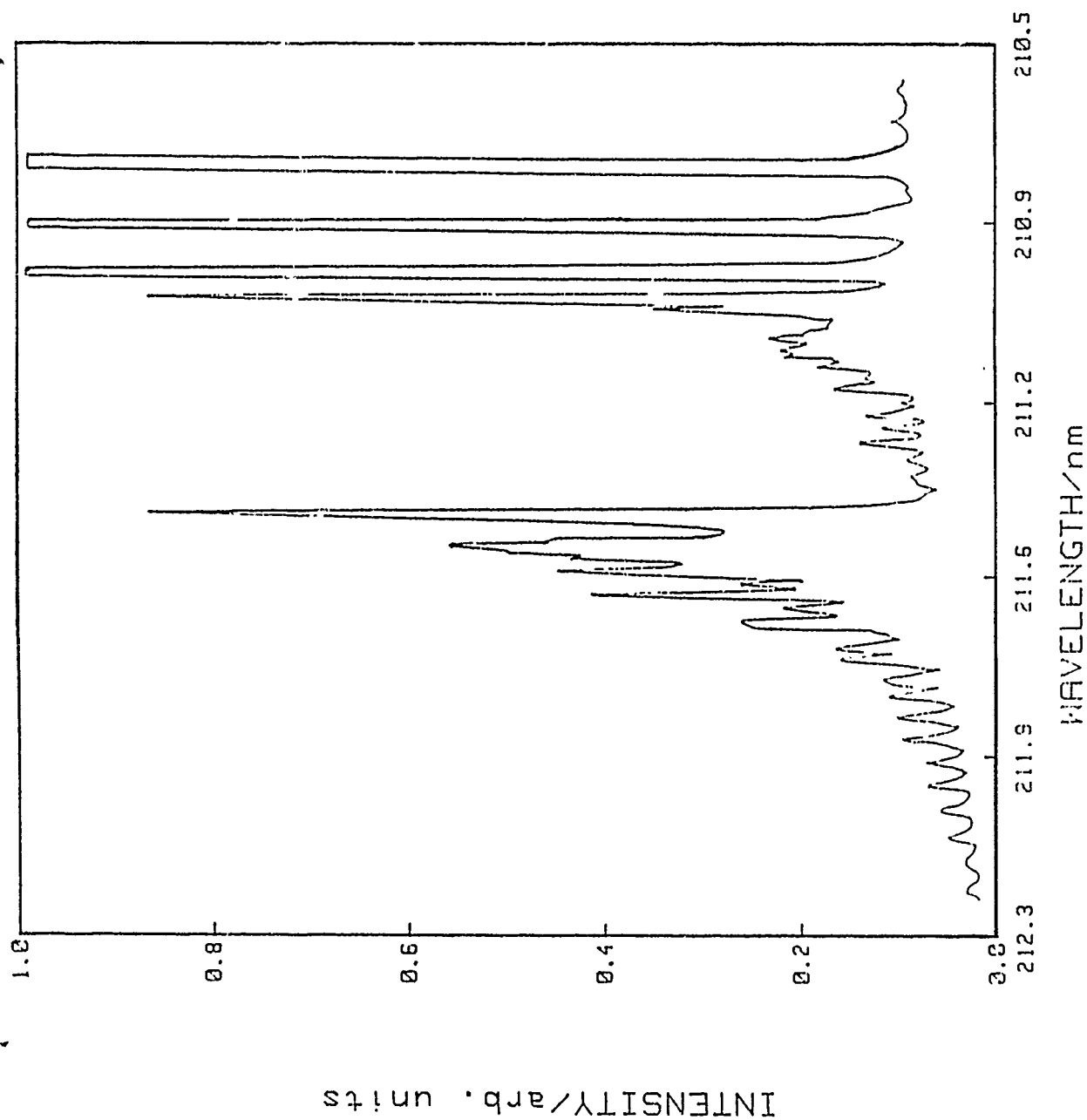


Figure 7.1. $N_2(a^1\Pi_g \rightarrow X^1\Sigma_g^+)$ spectra showing (9,17) and (13,20) bands. Flow conditions were 10% N_2 in He at a total pressure of 3.2 Torr.

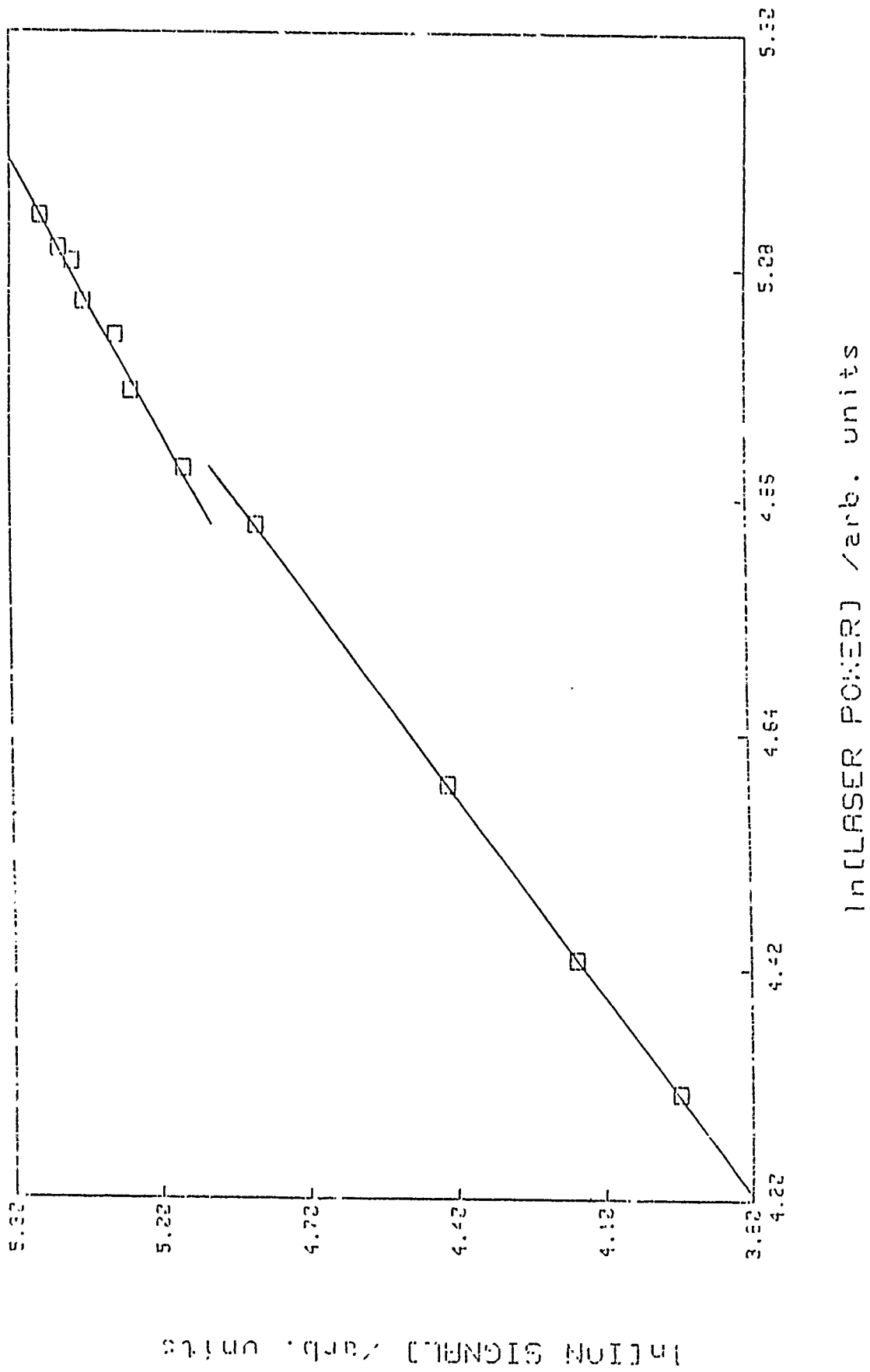


Figure 7.2. Laser power dependence of $N_2(9,17)$ band. The dependence ranges from 1.6 to 1.2 at higher power.

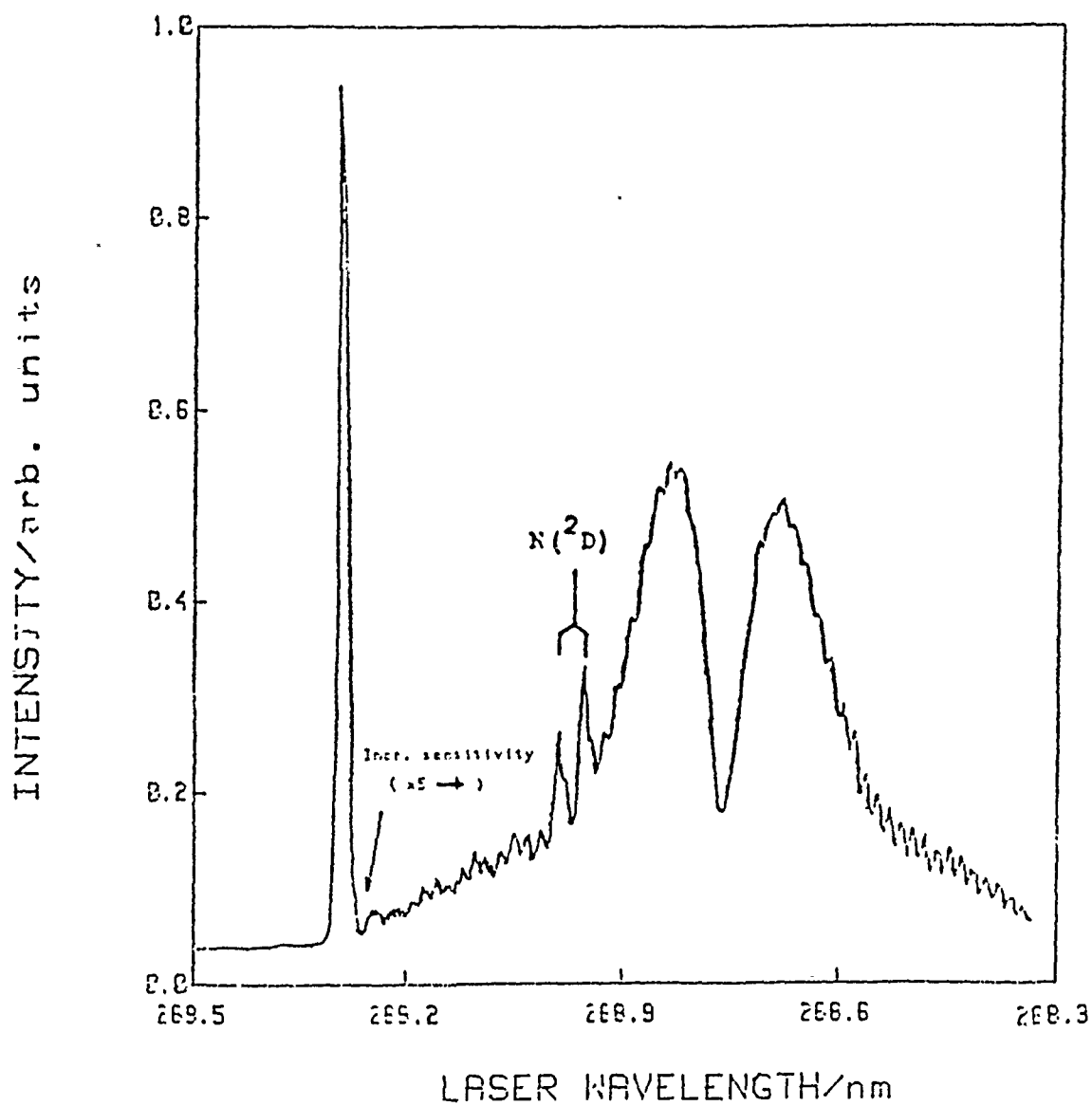


Figure 7.3. MPI spectrum of the region around the $N(^2D)$ transition in the presence of SF_6 showing the $S(^3P)$ line and the $NS(B^2\Sigma^+ \rightarrow X^2\Pi_{1/2})$ band.